SPINODAL INSTABILITIES IN NJL AND PNJL MODEL

A Dissertation

by

FENG LI

Submitted to the Office of Graduate and Professional Studies of
Texas A&M University
in partial fulfillment of the requirements for the degree of

DOCTOR OF PHILOSOPHY

Chair of Committee,	Che-Ming Ko
Committee Members,	Bhaskar Dutta
	Saskia Mioduszewski
	Joseph Natowitz
	Ralf Rapp
Head of Department,	George R. Welch

May 2016

Major Subject: Physics

ABSTRACT

We use both analytical and numerical approaches based on the Nambu-Jona-Lasino (NJL) or the Polyakov-Nambu-Jona-Lasino (PNJL) model to investigate the spinodal instability of a baryon-rich quark matter. In the analytical approach, we obtain via the linear response theory the boundaries of the spinodal region and calculate the growth rate of unstable modes during the early stage. We find that at the mean-field level, the boundaries of spinodal instabilities shrink with the wave number of unstable modes. Both the vector interaction and quantum effect suppress the spinodal instability. And the critical temperature T_c in the PNJL model is almost twice as large as in the NJL model. The collisional effects are then studied by solving the linearized Boltzmann equation, and are found to reduce the growth rate of unstable modes by an amount given by the inverse of the relaxation time. Numerically, we solve the transport equations by the test-particle method and study the phase separation for a quark matter in both a static box and an expanding fireball. We have calculated the higher-order density moments of the quark matter in a box and found them to increase and saturate at large values after phase separation, making them possible signals for a first-order phase transition in baryon-rich quark matter. The skewness of the quark number event-by-event distribution in a small sub-volume of the system is also found to increase, but this feature disappears if the subsystem is large. In the expanding quark matter, we find the expansions to be slowed by the presence of a first-order phase transition. Also, density clumps are found to appear and lead to an anisotropy in the momentum space, which can be characterized by the scaled density moments and the anisotropic elliptic (v_2) and quadrupolar (v_4) flows. An enhancement in the dilepton yield is also observed.

To my parents

ACKNOWLEDGEMENTS

First, I would like to thank my advisor, Prof. Che-Ming Ko, for his patience, enthusiasm and dedication. His guidance helped me during the research and writing of this dissertation. I look forward to our continued collaboration.

Prof. Ralf Rapp, Prof. Joseph B. Natowitz, Prof. Saskia Mioduszewski, and Prof. Bhaskar Dutta deserve my special thanks as my dissertation committee members for their valuable suggestions on both research and writing.

My sincere thanks also go to my group mates: Dr. Jun Xu, Dr. Taesoo Song, Dr. Yunpeng Liu, Kyongchol Han and Yifeng Sun for their helps on programming and experience sharing. I learned a lot from the discussions with them.

I acknowledge fruitful discussions with Dr. Min He, Dr. Guangyao Chen, Zilong Chang, Shuai Liu and Wei Zhao.

TABLE OF CONTENTS

Page

LIST OF FIGURES

FIGURE Page

1. INTRODUCTION

The confinement of color charges is one of the most mysterious features in the standard model. Due to their strong attractions through colored gluons, quarks in vacuum are bound in hadrons, so their color charges are not visible. However, it has been suggested that for a hadronic matter at sufficient high temperature and/or density, quarks and gluons inside the hadrons can become deconfined and form a soup of quarks and gluons called the quark-gluon plasma (QGP). This confinement-deconfinement transition was first found by Polyakov from the lattice calculations based on the SU(2) gauge theory by considering the so-called Polyakov loops [2]:

$$\begin{aligned}\Phi(\mathbf{x}) &\equiv \frac{1}{N_c}\mathrm{Tr}\left[P\exp\left(i\int_0^\beta d\tau A_4(\mathbf{x},\tau)\right)\right],\\ \bar{\Phi}(\mathbf{x}) &\equiv \frac{1}{N_c}\mathrm{Tr}\left[P\exp\left(-i\int_0^\beta d\tau A_4(\mathbf{x},\tau)\right)\right],\end{aligned} \tag{1.1}$$

where A_4 is the time component of the gauge field in the Euclidean space, P refers to path-ordering of the Euclidean time τ, and β is the inverse of the temperature. Both Φ and $\bar{\Phi}$ can be regarded as the order parameters for the color and anti-color confinement-deconfinement phase transition, respectively. Physically, the Polyakov loops Φ and $\bar{\Phi}$ are measures of $e^{-\beta F_\pm(\mathbf{x})}$, where $F_\pm(\mathbf{x})$ is the free energy of a pure gluon system with a static color ('+' sign) or anti-color ('-' sign) source located at $\mathbf{x}$ [3]. In the confined phase, which requires an infinite amount of free energy to add a static color or anti-color source in the system, $F_\pm \to \infty$, and the Polyakov loops are zero, while they are finite in the deconfined phase as it costs only finite free energy to add a static color or anti-color source.

Some interesting features of the confined quarks can be derived from the Polyakov

loop. One of them is the the reduction of color degrees of freedom, that is, the thermodynamics of confined quarks at temperature T behave as the thermodynamics of free quarks at temperature T/N_c (see Appendix A for details). This effect leads to a larger critical temperature T_c in the PNJL model than that in the NJL model, which does not include the effect of confinement, as discussed in Section 3.

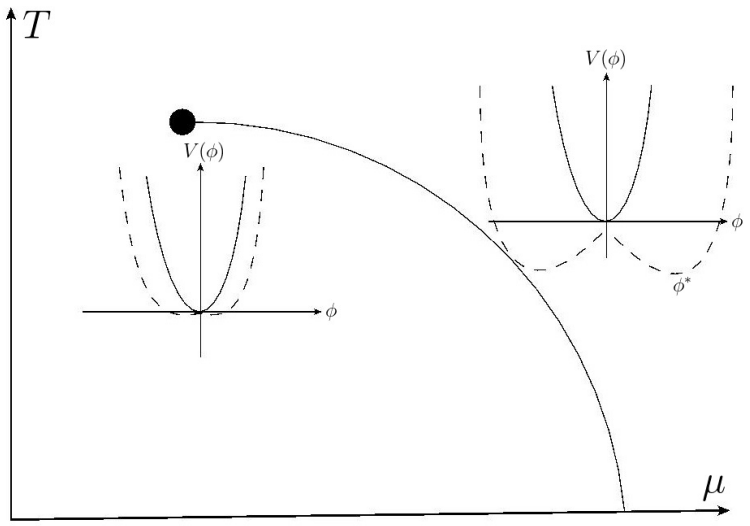

Figure 1.1: An illustration on the order of a phase transition in the temperature and chemical potential plane.

The behavior of the order parameter near the transition temperature determines the order of the phase transition. If the order parameter jumps from 0 to some finite value, it is a first-order phase transition. If it varies continuously but not smoothly, the phase transition is a second-order one. If it varies smoothly from 0 to some finite value, the transition is called a crossover, and no phase transition occurs. In general, the first and second-order phase transitions as well as the crossover transition can coexist in a phase diagram, and this is illustrated in Fig. 1.1. The solid curve

represents the phase boundary where the first-order phase transition occurs. The effective potential of the order parameter ϕ changes from a "V" shape (minimized at $\phi = 0$) at $T = T_0 - 0^+$ to a "W" shape (minimized at $\phi = \phi^* > 0$) at $T = T_0 + 0^+$. The order parameter thus jumps from 0 to ϕ^* when the first-order phase transition occurs. As the transition temperature T_0 rises, the two minima of "W" get closer, and finally merge at $T_0 = T_c$, where T_c, represented by the solid dot with baryon chemical potential $\mu = \mu_c$, is the so-called the critical end point. For a second-order phase transition, the effective potential jumps to a "U" shape instead of the "W" shape at $T = T_c$, and the order-parameter goes through a kink at $T = T_c$. For baryon chemical potential $\mu < \mu_c$, there is a crossover transition, and the order parameter changes smoothly from 0 to a finite value.

According to lattice QCD calculations, the phase transition in a QGP is a smooth crossover if it has zero baryon chemical potential [4]. However, due to difficulties in treating the fermion sign problem [5], lattice QCD has not provided definitive information on the order of the phase transition in QGP at finite chemical baryon potential and on the location of the critical end point.

Although information on the equation of state of baryon-rich quark matter has not been obtained from lattice QCD, studies based on various theoretical models have indicated that the quark-gluon plasma to hadronic matter transition changes to a first-order one when its baryon chemical potential is larger than a critical value [6, 7, 8, 9, 10, 11, 12, 13, 14, 15, 16, 17, 18, 19, 20, 21]. A possible signal for such a critical end point, at which the crossover transition changes to a first-order one, is the large higher moments in the net baryon or proton number event-by-event distributions in heavy ion collisions as suggested in Refs. [22, 23, 24, 25]. To determine if the critical end point exists and where it is located in the QCD phase diagram, the STAR Collaboration has carried out the beam energy scan (BES) program at RHIC to look

for this signal in collisions at nucleon-nucleon center of mass energies $\sqrt{s_{NN}}$ ranging from 7.7 to 39 GeV [26, 27, 28], which is expected to produce a baryon-rich QGP with baryon chemical potential in the range where a first-order QGP to hadronic matter transition is likely to appear. Although no definitive conclusion has been obtained from these experiments on the existence or the location of the critical point, the STAR Collaboration has observed many interesting phenomena that are different from those at higher collision energies. Among them is the increasing splitting of the elliptic flows of particles and their antiparticles with decreasing collision energy [29]. Based on an extension of a multiphase transport (AMPT) model [30] by including mean-field potentials from the Nambu-Jona-Lasinia (NJL) model [31, 32] for the partonic phase [33] and from empirical extracted values for the hadonic phase [34], a plausible explanation for this experimental observation has been achieved in Ref. [35], i.e., quarks and anti-quarks or hadrons and anti-hadrons are affected differently by the vector mean-field potentials in baryon-rich matter. Since a unique feature of a first-order phase transition is the large density fluctuations due to the spinodal instability that leads to the phase separation, we here extend the above study by using both the NJL model and its extension, the Polyakov-Nambu-Jona Lasinio (PNJL) model to investigate the spinodal instability of a baryon-rich QGP in the linear response theory as well as its semiclassical approximation, i.e., the linearized Boltzmann equation. We note that there already exist several studies in the literature on this interesting phenomenon and its possible signals based on the hydrodynamic approach [36, 37, 38, 39].

The remaining sections are organized as follows. A brief review on the Lagrangian and thermodynamic features of the NJL and PNJL models is given in Section 2. This is followed in Section 3 by an analytical calculation on the small amplitude spinodal instabilities by both using the linear response theory and solving the linearized

Boltzmann equations. The transport equation is solved by the test-particle method in Section 4 to study both the short and long time behavior of the spinodal instability of a quark matter in a periodic box. The same method is applied in Section 5 to an expanding quark matter to study how the density fluctuations are affected by the expansion of the system as in heavy ion collisions. Finally, a summary is given in Section 6.

Parts of the results from this dissertation have been published in Ref. [1]

2. THE NJL AND PNJL MODELS

In this section, we give a brief review on both the NJL and PNJL models, derive the gap equations, introduce the major features of chiral symmetry restoration and confinement-deconfinement transition, and most importantly, the thermodynamic properties of a quark matter. In all formulas shown in the following, we use i, j, k, l, m, n to label flavors, and a, b, c, d, e, f to label colors. Repeated indices are not summed unless indicated by a summation symbol.

2.1 The NJL and PNJL Lagrangians

The NJL model is an effective model of QCD for low-energy phenomena. It contains only the quark degrees of freedom as the gluon degrees of freedom are integrated out. Therefore, instead of being mediated by gluons, quarks interact by contact interactions characterized by a coupling constant G_S. The NJL Lagrangian containing only the scalar interaction for three quark flavors has the form [21]:

$$\begin{aligned}\mathcal{L}^S_{NJL} &= \bar{q}(i\not{\partial} - M)q + \frac{G_S}{2}\sum_{a=0}^{8}\Big[(\bar{q}\lambda^a q)^2 + (\bar{q}i\gamma_5\lambda^a q)^2\Big] \\ &\quad -K\Big[\det{}_f\Big(\bar{q}(1+\gamma_5)q\Big) + \det{}_f\Big(\bar{q}(1-\gamma_5)q\Big)\Big], \end{aligned} \tag{2.1}$$

where $q = (u, d, s)^T$, $M = \mathrm{diag}(m_u, m_d, m_s)$ is the quark mass matrix and λ^a are the Gell-Mann matrices with λ^0 being the identity matrix multiplied by $\sqrt{2/3}$. The Lagrangian preserves $U(1) \times SU(N_f)_L \times SU(N_f)_R$ symmetry. The axial symmetry is broken due to axial anomaly in QCD. In the NJL model, this symmetry is explicitly broken by the Kobayashi-Masakawa-t'Hooft (KMT) interaction given by the last term in Eq. (2.1) [40]. The $\det_f$ denotes the determinant in the flavor space [41],

that is

$$\det{}_f(\bar{q}\Gamma q) = \sum_{i,j} \varepsilon_{ij}(\bar{u}\Gamma q_i)(\bar{d}\Gamma q_j) \tag{2.2}$$

in the case of SU(2) and

$$\det{}_f(\bar{q}\Gamma q) = \sum_{i,j,k} \varepsilon_{ijk}(\bar{u}\Gamma q_i)(\bar{d}\Gamma q_j)(\bar{s}\Gamma q_k) \tag{2.3}$$

in the case of SU(3), where Γ denotes either a Dirac gamma or the identity matrix. The KMT interaction gives rise to four-point interactions in two flavors and six-point interactions in three flavors. In the two flavor case, the sum of scalar and pseudo-scalar interactions and the KMT interaction with K=-G reduces to the original NJL model [6, 31]. In the three flavor case, the determinantal term is responsible for obtaining the correct splitting in the masses of η and η' mesons.

A flavor-singlet vector interaction can also be added to the NJL Lagrangian as follows:

$$\mathcal{L}^V_{NJL} = -G_V(\bar{q}\gamma^\mu q)^2, \tag{2.4}$$

where the coupling constant G_V is assumed to be independent of T and μ. By adjusting the value of G_V, we can obtain an equation of state with or without a first-order phase transition.

Because the NJL model is not renormalizable, a regularization scheme is required to remove infinities in the momentum integrations. In this work, we assume that all interactions are among quarks of 3-momentum with magnitude below the cutoff momentum Λ.

By fixing the parameters G_S, K and Λ from the pion mass m_π and decay constant f_π, and the kaon mass m_K, the NJL model gives reasonable constituent quark

masses, i.e. 367 MeV for u, d quarks and 549 MeV for s quarks, and also reproduces the Gellmann-Oakes-Renner relation $m_\pi^2 f_\pi^2 = (m_u + m_d)\langle q\bar{q}\rangle$ [42], where m_u and m_d are the bare up and down quark masses, respectively, and $\langle q\bar{q}\rangle$ is the quark condensate in vacuum. The model further predicts that chiral symmetry is restored at high temperature [43] and high net baryon density [6] as expected from the QCD. More importantly, the NJL model gives a pressure in a quark matter that decreases isothermally with the net quark density within a certain region of temperature and density (or chemical potential) in the QCD phase digram, indicating the existence of a spinodal region and thus the possibility to use it to study the spinodal instabilities in QGP.

Due to the three and four-gluon self-interactions, quarks can also couple to gluon loops in the QGP. By integrating out the gluon degrees of freedom, quarks are then also affected by a background field due to their interactions with gluons [44, 45]. This effect is not included in the NJL model, which only includes the effective contact interactions among quarks. As a result, the NJL model fails to describe the equation of state obtained from the lattice QCD for QGP at high temperature and zero baryon chemical potential. To include the effect of quark interactions with gluons, the NJL model was extended to the PNJL model [46, 47] by taking into consideration the contribution from the Polyakov loop mentioned in Section 1, where quarks of different color are affected by different imaginary potentials. The NJL action is then modified as follows:

$$\begin{aligned}\mathcal{S}_{\rm PNJL}[q,\bar{q},\phi] &= \beta V\mathcal{U}(\Phi,\bar{\Phi},T) - \int_0^\beta \mathrm{d}^4x\Big\{\bar{q}(-\gamma^0(\partial_\tau + i\bar{\phi}) + i\boldsymbol{\gamma}\cdot\nabla - m_0)q \\ &\quad + \frac{G_S}{2}\sum_{a=0}^{8}\Big[(\bar{q}\lambda^a q)^2 + (\bar{q}i\gamma_5\lambda^a q)^2\Big] - G_V(\bar{q}\gamma_\mu q)^2 \\ &\quad - K\Big[\det{}_f\Big(\bar{q}(1+\gamma_5)q\Big) + \det{}_f\Big(\bar{q}(1-\gamma_5)q\Big)\Big]\Big\}, \end{aligned} \tag{2.5}$$

where $\bar{\phi} = \mathrm{diag}(\bar{\phi}^1, \bar{\phi}^2, -\bar{\phi}^1 - \bar{\phi}^2)$ is the background gauge field with $\bar{\phi}^a$ defined in Eq. (A.2), and $\mathcal{U}(\Phi, \bar{\Phi}, T)$ is the effective potential for the Polyakov loops defined in Eq. (1.1), i.e.,

$$\frac{\mathcal{U}(\Phi, \bar{\Phi}, T)}{T^4} = -\frac{1}{2}a(T)\bar{\Phi}\Phi + b(T)\ln[1 - 6\bar{\Phi}\Phi + 4(\bar{\Phi}^3 + \Phi^3) - 3(\bar{\Phi}\Phi)^2], \tag{2.6}$$

with

$$a(T) = a_0 + a_1\left(\frac{T_0}{T}\right) + a_2\left(\frac{T_0}{T}\right)^2, \quad b(T) = b_3\left(\frac{T_0}{T}\right)^3. \tag{2.7}$$

In order to ensure that the lattice QCD results for the thermodynamics of the pure gauge theory are reproduced for T up to twice the critical temperature T_0 for the deconfinement transition, we follow Ref. [48] to take $a_0 = 3.51$, $a_1 = -2.47$, $a_2 = 15.2$, and $b_3 = -1.75$. For T_0, there are two possible values being considered in literatures. In one case with $T_0 = 270$ MeV, the deconfinement transition temperature at $\mu = 0$ is 210 MeV and is almost the same as the chiral transition temperature of 222 MeV in this model [49], and both are higher than the result from recent lattice calculations, which ranges from 145 to 163 MeV [50, 51, 52]. In the other case with $T_0 = 210$ MeV, the transition temperatures become 171 MeV for the deconfinement and 203 MeV for the chiral restoration transitions, and their average value $T_X = 187$ MeV [49] is closer to the result from lattice calculations.

2.2 The gap equations

The gap equations are the self-consistent equations that determine the effective (or constituent) quark masses. They are obtained from the NJL Lagrangian (or action) in the mean-field approximation by replacing the interactions among quarks with interactions between a single quark and a background field. In this approximation, the modified Lagrangian becomes bilinear in quark fields. As an example, we

consider terms such as $\sum_a \frac{G_S}{2}(\bar{q}\lambda^a q)^2$ and $\sum_a \frac{G_S}{2}(\bar{q}i\gamma_5\lambda^a q)^2$. Since,

$$\sum_a (\bar{q}\Gamma\lambda^a q)^2 = 2\sum_{ij} \bar{q}_i\Gamma q_j \bar{q}_j\Gamma q_i, \tag{2.8}$$

where Γ is some operator defined in the Clifford space, i.e., the identity and gamma matrices and their productions. In the mean-field approximation, they become

$$\sum_{ij} \bar{q}_i\Gamma q_j \bar{q}_j\Gamma q_i \approx 2\sum_{ij} \langle\bar{q}_i\Gamma q_j\rangle \bar{q}_j\Gamma q_i - \sum_{ij} \langle\bar{q}_i\Gamma q_j\rangle\langle\bar{q}_j\Gamma q_i\rangle, \tag{2.9}$$

where $\langle\cdots\rangle$ indicates taking the expectation value. Keeping only the Hartree terms, namely, neglecting terms including $\langle\bar{q}_i\Gamma q_j\rangle$ with $i \neq j$ that contribute only to the residual interactions [53], we then have:

$$\sum_a (\bar{q}\Gamma\lambda^a q)^2 \approx 4\sum_i \langle\bar{q}_i\Gamma q_i\rangle \bar{q}_i\Gamma q_i - 2\sum_i \langle\bar{q}_i\Gamma q_i\rangle^2. \tag{2.10}$$

Similarly, we have by keeping only Hartree terms,

$$(\bar{q}\Gamma q)^2 \approx 2\langle\sum_j \bar{q}_j\Gamma q_j\rangle \sum_i \bar{q}_i\Gamma q_i - \langle\sum_i \bar{q}_i\Gamma q_i\rangle^2, \tag{2.11}$$

$$\begin{aligned}\det_f(\bar{q}\Gamma q) \approx\ & \bar{u}\Gamma u\langle\bar{d}\Gamma d\rangle\langle\bar{s}\Gamma s\rangle + \langle\bar{u}\Gamma u\rangle\bar{d}\Gamma d\langle\bar{s}\Gamma s\rangle + \langle\bar{u}\Gamma u\rangle\langle\bar{d}\Gamma d\rangle\bar{s}\Gamma s \\ & -2\langle\bar{u}\Gamma u\rangle\langle\bar{d}\Gamma d\rangle\langle\bar{s}\Gamma s\rangle.\end{aligned} \tag{2.12}$$

By denoting $\sigma_i = \langle\bar{q}_i q_i\rangle$, $\theta_i = \langle\bar{q}_i\gamma_5 q_i\rangle$, and $j^\mu = \langle\sum_i \bar{q}_i\gamma^\mu q_i\rangle$, the orginal action becomes:

$$\begin{aligned}\mathcal{S}_{\rm PNJL}[q,\bar{q},\phi] \approx \beta V\mathcal{U}(\Phi,\bar{\Phi},T) - \int_0^\beta \mathrm{d}^4x\Big\{\sum_{i,j,k;\text{cyclic}} \bar{q}_i\Big(-\gamma^0(\partial_\tau + i\bar{\phi} - \mu - i\mathbf{u}\cdot\nabla) \\ + i\boldsymbol{\gamma}\cdot\nabla - m_{0i} + 2G_S\sigma_i - 2G_S\gamma_5\theta_i - 2K(\sigma_j\sigma_k + \theta_j\theta_k) - 2K\gamma_5(\sigma_j\theta_k + \theta_j\sigma_k)\end{aligned}$$

$$- 2G_V\gamma^\mu j_\mu\Big)q_i + \sum_i G_S(\sigma_i^2 - \theta_i^2) - 2K\prod_i(\sigma_i + \theta_i) - 2K\prod_i(\sigma_i - \theta_i) - G_V j^2\Big\}. \tag{2.13}$$

Eq.(2.13) is bilinear in the quark (q) field, with σ_i, θ_i,$\bar{\phi}$ and j being background fields that act on q. To evaluate them, we minimize the thermodynamic potential defined as follows:

$$\begin{aligned}\Omega(T,\mu) &\equiv -(\beta V)^{-1}\ln\mathcal{Z} \\ &= \mathcal{U}(\Phi,\bar{\Phi},T) + \sum_i G_S(\sigma_i^2 - \theta_i^2) - 2K\prod_i(\sigma_i + \theta_i) - 2K\prod_i(\sigma_i - \theta_i) \\ &\quad -G_V j^2 - \frac{T}{V}\ln\mathrm{Det}[\beta\widetilde{S}^{-1}_{p<\Lambda}] - \frac{T}{V}\ln\mathrm{Det}[\beta\widetilde{S}^{-1}_{p>\Lambda}],\end{aligned} \tag{2.14}$$

where the Matsubara propagator of a constituent quark can be read explicitly from Eq. (2.13) as:

$$\begin{aligned}(\widetilde{S}^{-1}_{p<\Lambda})^{ab}_{il}(i\omega_n,\mathbf{p}) &= \delta^{ab}\delta_{il}[\gamma^0(-i\omega_n + i\bar{\phi}^a - \mu + \mathbf{u}\cdot\mathbf{p}) + \boldsymbol{\gamma}\cdot\mathbf{p} + m_{0i} - 2G_S\sigma_i \\ &\quad +2G_S\gamma_5\theta_i + 2K(\sigma_j\sigma_k + \theta_j\theta_k) + 2K\gamma_5(\sigma_j\theta_k + \theta_j\sigma_k) + 2G_V\gamma^\mu j_\mu],\end{aligned} \tag{2.15}$$

and

$$(\widetilde{S}^{-1}_{p>\Lambda})^{ab}_{il}(i\omega_n,\mathbf{p}) = \delta^{ab}\delta_{il}[\gamma^0(-i\omega_n + i\bar{\phi}^a - \mu + \mathbf{u}\cdot\mathbf{p}) + \boldsymbol{\gamma}\cdot\mathbf{p} + m_{0i}]. \tag{2.16}$$

We first evaluate the last two terms in Eq. (2.14). Evaluating the determinants in the color, flavor and spinor spaces results in:

$$\begin{aligned}\ln\det[\beta\widetilde{S}^{-1}_{p<\Lambda}] &= 2\sum_{a,i}\ln\det\beta^2[-(i\omega_n - i\bar{\phi}^a + \mu - \mathbf{u}\cdot\mathbf{p} - 2G_V j^0)^2 + (\mathbf{p} - 2G_V\mathbf{j})^2 \\ &\quad + (m_{0i} - 2G_S\sigma_i + 2K(\sigma_j\sigma_k + \theta_j\theta_k))^2 - 4(G_S\theta_i + K(\sigma_j\theta_k + \theta_j\sigma_k))^2],\end{aligned} \tag{2.17}$$

and

$$\ln\det[\beta\widetilde{S}^{-1}_{p>\Lambda}] = 2\sum_{a,i}\ln\det\beta^2[-(i\omega_n - i\bar{\phi}^a + \mu - \mathbf{u}\cdot\mathbf{p})^2 + \mathbf{p}^2 + m_{0i}^2]. \qquad (2.18)$$

Introducing

$$\begin{aligned} M_i &= m_{0i} - 2G_S\sigma_i + 2K(\sigma_j\sigma_k + \theta_j\theta_k), && (2.19)\\ \widetilde{\mu}_a &= \mu - i\bar{\phi}^a - 2G_V j^0, && (2.20)\\ E_{\mathbf{p}i} &= \sqrt{M_i^2 + (\mathbf{p} - 2G_V\mathbf{j})^2 - 4(G_S\theta_i + K(\sigma_j\theta_k + \theta_j\sigma_k))^2}, && (2.21) \end{aligned}$$

where the subscripts $i \neq j \neq k$, and applying the equality $\mathrm{tr}\ln[A] = \ln\det[A]$, the determinant is then

$$\begin{aligned} \ln\det[\beta\widetilde{S}^{-1}_{p<\Lambda}] &= 2\sum_{a,i}\mathrm{tr}\ln\beta^2[-(i\omega_n + \widetilde{\mu}_a - \mathbf{u}\cdot\mathbf{p})^2 + E^2_{\mathbf{p}i}]\\ &= 2V\sum_{a,i,\omega_n}\int_0^\Lambda \frac{d^3\mathbf{p}}{(2\pi)^3}\ln\beta^2[-(i\omega_n + \widetilde{\mu}_a - \mathbf{u}\cdot\mathbf{p})^2 + E^2_{\mathbf{p}i}]\\ &= 2V\sum_{a,i}\int_0^\Lambda \frac{d^3\mathbf{p}}{(2\pi)^3}\Big\{\beta E_{\mathbf{p}i} + \ln(1 + \mathrm{e}^{-\beta(E_{\mathbf{p}i} + \widetilde{\mu}_a - \mathbf{u}\cdot\mathbf{p})})\\ &\qquad + \ln(1 + \mathrm{e}^{-\beta(E_{\mathbf{p}i} - \widetilde{\mu}_a + \mathbf{u}\cdot\mathbf{p})})\Big\}\\ &= 2V\sum_{i}\int_0^\Lambda \frac{d^3\mathbf{p}}{(2\pi)^3}\Big\{3\beta E_{\mathbf{p}i} + \ln(1 + 3\bar{\Phi}\xi_i^{-1} + 3\Phi\xi_i^{-2} + \xi_i^{-3})\\ &\qquad + \ln(1 + 3\Phi\xi_i'^{-1} + 3\bar{\Phi}\xi_i'^{-2} + \xi_i'^{-3})\Big\}, \qquad (2.22) \end{aligned}$$

where $\xi_i = \exp(\beta(E_{\mathrm{p}_i} - \mu + \mathbf{u}\cdot\mathbf{p} + 2G_V j^0))$ and $\xi_i' = \exp(\beta(E_{\mathrm{p}_i} + \mu - \mathbf{u}\cdot\mathbf{p} - 2G_V j^0))$. Similarly, we have

$$\ln\det[\beta\widetilde{S}^{-1}_{p>\Lambda}] = 2V\sum_{i}\int_\Lambda^\infty \frac{d^3\mathbf{p}}{(2\pi)^3}\Big\{3\beta E^0_{\mathbf{p}i} + \ln(1 + 3\bar{\Phi}\xi_{0i}^{-1} + 3\Phi\xi_{0i}^{-2} + \xi_{0i}^{-3})$$

$$+\ln(1+3\Phi\xi_{0i}'^{-1}+3\bar{\Phi}\xi_{0i}'^{-2}+\xi_{0i}'^{-3})\Big\}, \tag{2.23}$$

where $E^0_{\mathbf{p}i}=\sqrt{m_{0i}^2+\mathbf{p}^2}$, $\xi_{0i}=\exp(\beta(E^0_{\mathrm{p}_i}-\mu+\mathbf{u}\cdot\mathbf{p}))$, and $\xi'_{0i}=\exp(\beta(E^0_{\mathrm{p}_i}+\mu-\mathbf{u}\cdot\mathbf{p}))$

The thermodynamic potential is minimized if $0=\partial\Omega/\partial\theta_i=\partial\Omega/\partial\sigma_i=\partial\Omega/\partial j^\mu=\partial\Omega/\partial\Phi=\partial\Omega/\partial\bar{\Phi}$, which leads to:

$$\begin{aligned}
\theta_i &= 0, && (2.24)\\
\sigma_i &= 6\int_0^\Lambda \frac{\mathrm{d}^3\mathbf{p}}{(2\pi)^3}\frac{M_i}{E_{\mathrm{p}_i}}(f_0(\xi_i;\Phi,\bar{\Phi})+f_0(\xi'_i;\bar{\Phi},\Phi)-1), && (2.25)\\
j^0 &= 6\sum_i\int_0^\Lambda \frac{\mathrm{d}^3\mathbf{p}}{(2\pi)^3}(f_0(\xi_i;\Phi,\bar{\Phi})-f_0(\xi'_i;\bar{\Phi},\Phi)), && (2.26)\\
\mathbf{j} &= 6\sum_i\int_0^\Lambda \frac{\mathrm{d}^3\mathbf{p}}{(2\pi)^3}(f_0(\xi_i;\Phi,\bar{\Phi})+f_0(\xi'_i;\bar{\Phi},\Phi)-1)\frac{\mathbf{p}-2G_V\mathbf{j}}{E_{\mathrm{p}_i}}, && (2.27)
\end{aligned}$$

and

$$\begin{aligned}
&\partial_\Phi\mathcal{U}(\Phi,\bar{\Phi},T)\\
=\;& 6T\sum_i\int_0^\Lambda\frac{d^3\mathbf{p}}{(2\pi)^3}\Big\{\frac{\xi_i}{\xi_i^3+3\bar{\Phi}\xi_i^2+3\Phi\xi_i+1}+\frac{\xi_i'^2}{\xi_i'^3+3\Phi\xi_i'^2+3\bar{\Phi}\xi_i'+1}\Big\}\\
&+6T\sum_i\int_\Lambda^\infty\frac{d^3\mathbf{p}}{(2\pi)^3}\Big\{\frac{\xi_{0i}}{\xi_{0i}^3+3\bar{\Phi}\xi_{0i}^2+3\Phi\xi_{0i}+1}+\frac{\xi_{0i}'^2}{\xi_{0i}'^3+3\Phi\xi_{0i}'^2+3\bar{\Phi}\xi_{0i}'+1}\Big\}, && (2.28)\\
&\partial_{\bar{\Phi}}\mathcal{U}(\Phi,\bar{\Phi},T)\\
=\;& 6T\sum_i\int_0^\Lambda\frac{d^3\mathbf{p}}{(2\pi)^3}\Big\{\frac{\xi_i^2}{\xi_i^3+3\bar{\Phi}\xi_i^2+3\Phi\xi_i+1}+\frac{\xi_i'}{\xi_i'^3+3\Phi\xi_i'^2+3\bar{\Phi}\xi_i'+1}\Big\}\\
&+6T\sum_i\int_\Lambda^\infty\frac{d^3\mathbf{p}}{(2\pi)^3}\Big\{\frac{\xi_{0i}^2}{\xi_{0i}^3+3\bar{\Phi}\xi_{0i}^2+3\Phi\xi_{0i}+1}+\frac{\xi_{0i}'}{\xi_{0i}'^3+3\Phi\xi_{0i}'^2+3\bar{\Phi}\xi_{0i}'+1}\Big\}, && (2.29)
\end{aligned}$$

where

$$f_0(\xi_i;\Phi,\bar{\Phi})=\frac{\bar{\Phi}\xi_i^2+2\Phi\xi_i+1}{\xi_i^3+3\bar{\Phi}\xi_i^2+3\Phi\xi_i+1} \tag{2.30}$$

is the color-averaged equilibrium quark distribution. Details of the derivation of

Eq. (2.30) are given in Appendix A. Eq.(2.30) reduces to the normal Fermi-Dirac distribution for $\Phi = \bar{\Phi} = 1$. The above equations together with Eq.(2.19) are called the gap equations, from which we can calculate M_i, j^0, $\mathbf{j}$, Φ and $\bar{\Phi}$ self consistently. From Eqs. (2.28) and (2.29), we have $\Phi = \bar{\Phi}$ in the case of $\mu = \mathbf{u} = 0$, and they differ slightly for finite μ.

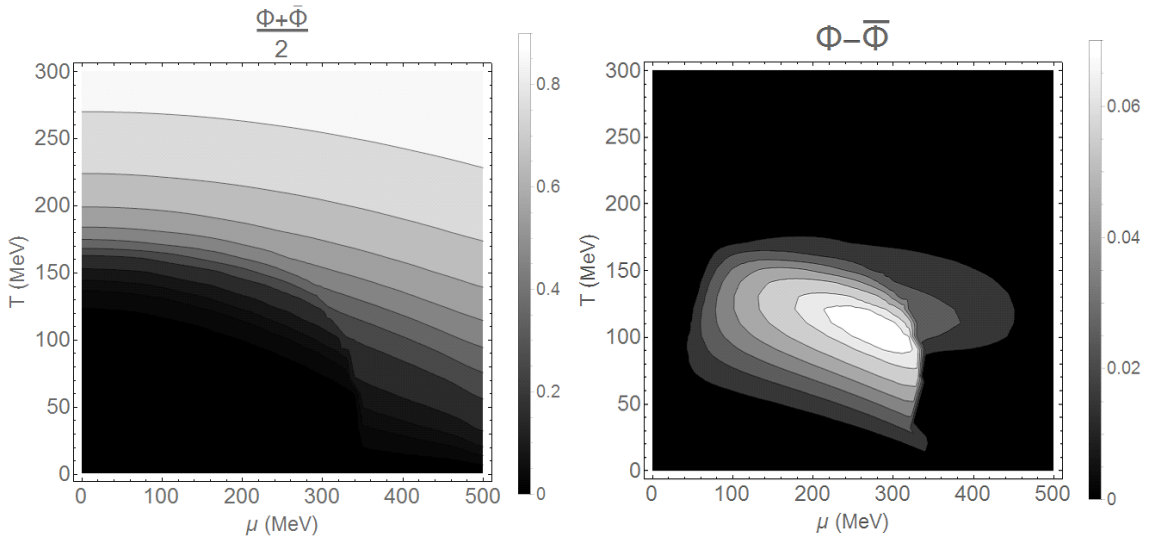

Figure 2.1: Average (left window) and difference (right window) of Polyakov loops Φ and $\bar{\Phi}$ as functions of T and μ.

The average and the difference of Φ and $\bar{\Phi}$ are shown as functions of T and μ in the left and right windows of Fig. 2.1, respectively. They are calculated from the PNJL Lagrangian with model parameters taken from Ref.[48], i.e., $\Lambda = 0.6023$ GeV, $G_S = 3.67\Lambda^2$, and $K = 12.36\Lambda^5$. The average of Polyakov loops shows a smooth transition from the confined phase (dark area) to the deconfined phase (bright area). The transition temperature, defined by $\Phi + \bar{\Phi} = 1$, is about 170 MeV at $\mu = 0$ and decreases as μ increases. There is also a less conspicuous at $\mu \approx 350$ MeV,

beyond which the transition temperature drops suddenly. This corresponds to the transition to the so-called quarkyonic phase that is confined, but chirally restored [54] as shown in Fig. 2.2 by the small light quark masses above this value of baryon chemical potential. The difference of Polyakov loops (the $\Phi - \bar{\Phi}$) shows that it almost vanishes at both low and high temperatures, and is much smaller than the average of Polyakov loops, implying that the confinement-deconfinement transition is indistinguishable between color and anti-color charges even in baryon rich quark matter.

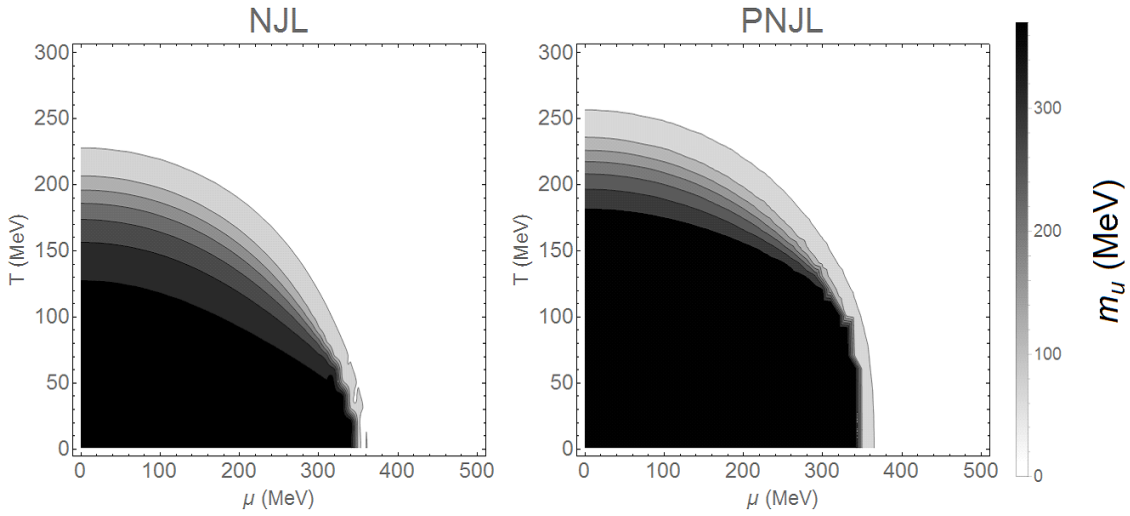

Figure 2.2: Effective u and d quark masses as functions of T and μ calculated from the NJL model (left window) and the PNJL model (right window) with model parameters $\Lambda = 0.6023$ GeV, $G_S = 3.67\Lambda^2$, and $K = 12.36\Lambda^5$.

The effective quark masses $M_{u,d}$ calculated from the NJL and PNJL models are shown in the left and right windows of Fig. 2.2, respectively. The chiral restoration, described by the drop of $M_{u,d}$ from the constituent mass to the bare mass, is seen for large μ or T. The transition along the T axis is smooth. At $\mu = 0$, the chiral

transition temperatures from the NJL and PNJL models are about 170 and 240 MeV, respectively, and $M_{u,d}$ drops more rapidly in the PNJL than in the NJL model. While along the μ axis, $M_{u,d}$ jumps from 367 MeV to the bare mass at $\mu \approx 350$ MeV in the low temperature region, and this is the first-order phase transition we are interested in.

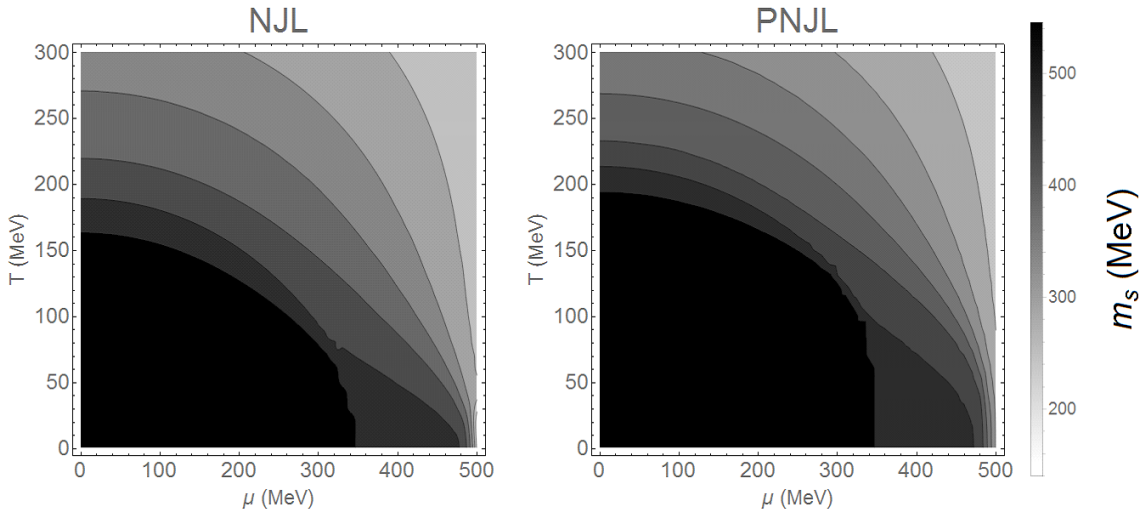

Figure 2.3: Effective s quark mass as a function of T and μ calculated from the NJL model (left window) and the PNJL model (right window) with model parameters $\Lambda = 0.6023$ GeV, $G_S = 3.67\Lambda^2$, and $K = 12.36\Lambda^5$.

The change in M_s, which is shown in Fig. 2.3, is more complicated at low temperature. As μ increases, M_s first jumps from 550 MeV to 462 MeV at $\mu \approx 350$ MeV, and remains constant until $\mu \approx 500$ MeV, when it changes smoothly to the bare mass.

2.3 Equation of state

The equation of state of quark matter gives the relation among its energy density, pressure, net quark density and temperature. For describing a first-order phase tran-

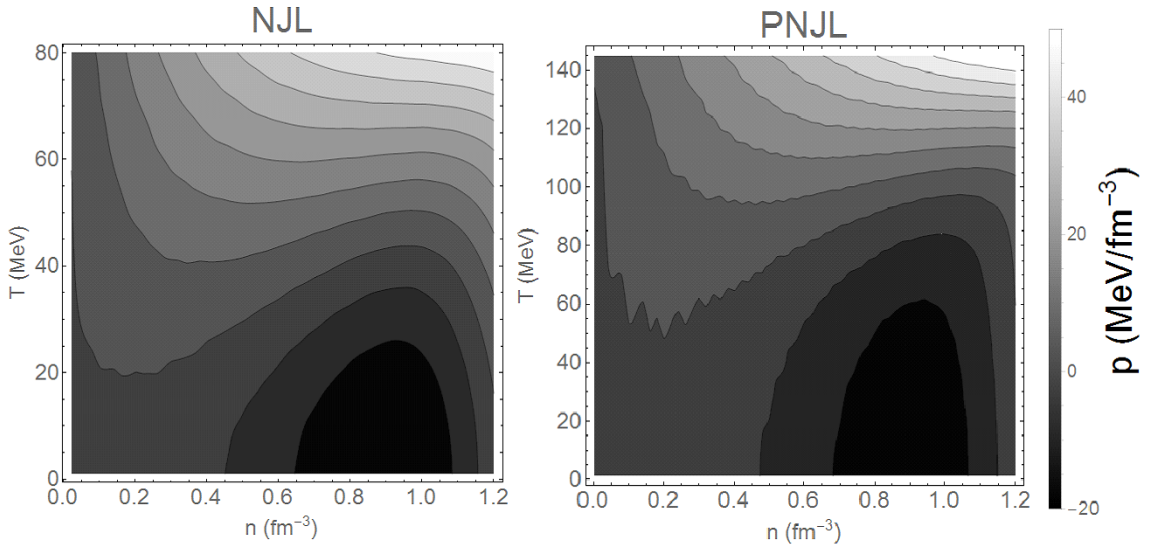

Figure 2.4: Pressure as a function of temperature T and net quark density n from the NJL model (left window) and the PNJL model (right window) with model parameters $\Lambda = 0.6023$ GeV, $G_S = 3.67\Lambda^2$, and $K = 12.36\Lambda^5$.

sition, pressure plays an important role. In Fig. 2.4, we show the pressure calculated from both the NJL and PNJL models in the left and right windows, respectively. They are obtained by simply taking the negative of the thermal potential given by Eq.(2.14). We note that for temperatures below 70 MeV in the NJL model and 120 MeV in the PNJL model, the pressure first increases, then decreases, and finally increases again with the net quark density. The decreasing part, i.e., $(\partial P/\partial n)_T < 0$, corresponds to the isothermal spinodal instability, which can be understood as follows. Consider a gas of particles in a box that is separated into two parts by a partition in the middle. In the normal case of $(\partial P/\partial n) > 0$, pushing the partition slightly leftward compresses the left part of the gas and increases its pressure, which then pushes the partition back to the middle. However, if the pressure decreases with density, the pressure difference between the two parts of the gas will drive the partition further to the left until gases in both sides are outside the spinodal insta-

bility region and reach a new equilibrium state with a dense phase on the left side and a dilute phase on the right side. If such a process happens isothermally, namely the system keeps in contact with a heat bath of constant temperature T, the criterion for spinodal instability is $(\frac{\partial p}{\partial n})_T < 0$. If the process is adiabatic, the criterion is $(\frac{\partial p}{\partial n})_S < 0$, where the subscript S denotes the entropy per net quark number.

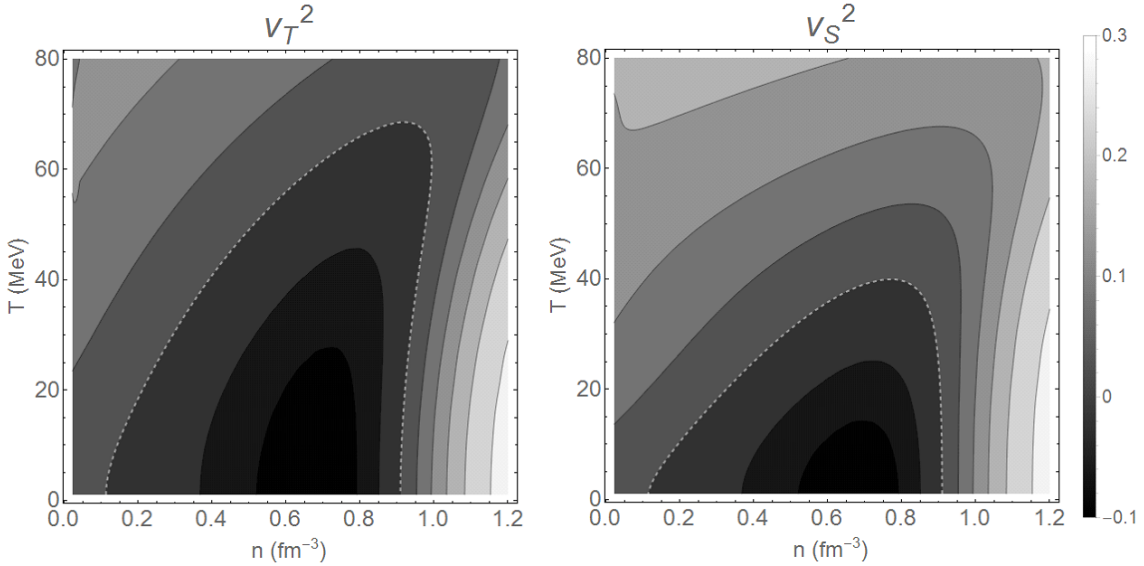

Figure 2.5: Square of the speed of sound (v^2) as a function of temperature T and net quark density n from the NJL model, in the isothermal (left window) and the isentropic (right window) cases. Contours where $v^2 = 0$ are shown by dashed curves, inside which is the spinodal instability region.

The above behavior of a system is called "instability" because a small deviation from equilibrium, such as pushing the partition slightly leftward, will be amplified and lead to a phase separation. Consider the Fourier expansion of the density fluctuation, $\delta n(t, \mathbf{x}) = \sum_{\mathbf{k}} \delta n_{\mathbf{k}} \exp(i\omega_k t - i\mathbf{k} \cdot \mathbf{x})$. When the frequency ω_k is imaginary, the fluctuation then grows exponentially with time. According to Ref.[55] based on an ideal hydrodynamic model, $\omega_{\mathbf{k}} = v_S k$ if the growth of the instability is adiabatic,

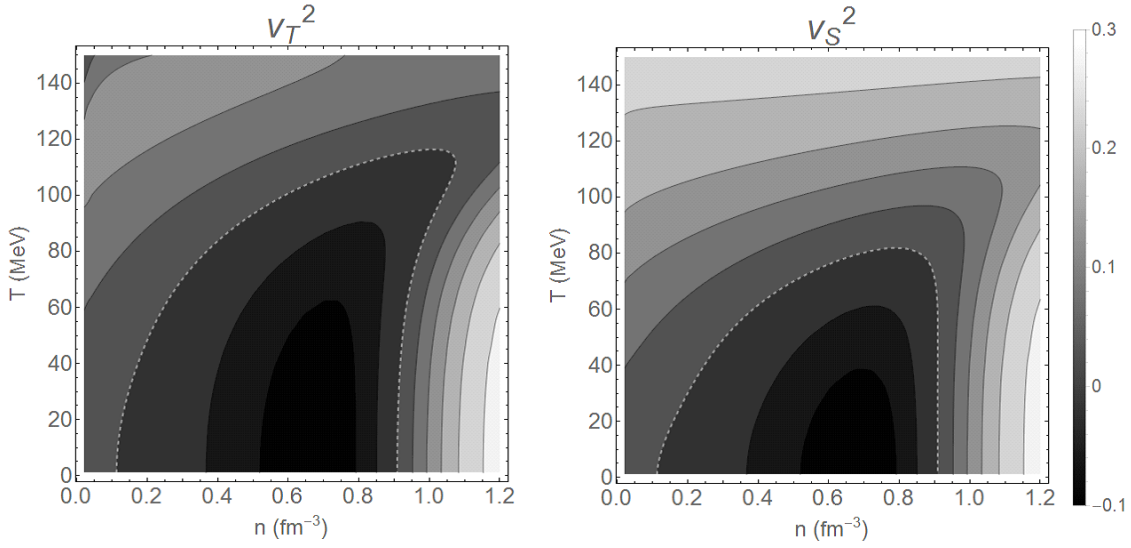

Figure 2.6: Square of the speed of sound (v^2) as a function of temperature T and net quark density μ from the PNJL model for the isothermal (left window) and the isentropic (right window) cases. Contours where $v^2 = 0$ are shown by dashed curves, inside which is the spinodal instability region.

and $\omega_{\mathbf{k}} = v_T k$ if it is isothermal, where $v_S^2 = \frac{n}{\epsilon+p}\left(\frac{\partial p}{\partial n}\right)_S$ and $v_T^2 = \frac{n}{\epsilon+p}\left(\frac{\partial p}{\partial n}\right)_T$ are the square of the isentropic and the isothermal speed of sound, respectively. The above two criteria are thus equivalent to $v_T^2 < 0$ and $v_S^2 < 0$. The more negative the v^2 is, the faster the fluctuations grow. The v_T^2 and v_S^2 calculated from the NJL model are shown in the left and right windows of Fig. 2.5, respectively. The contours that $v_T^2 = 0$ and $v_S^2 = 0$ are drawn by white dashed curves, inside which are the isothermal and isentropic spinodal instability regions of the NJL model. It is seen that the isothermal instability region is larger than the isentropic one. The critical temperature, corresponding to the highest temperature in the spinodal instability region, is aout 70 MeV in the isothermal case, consistent with the results in Fig. 2.4, while it is about 40 MeV in the isentropic case. A similar feature is seen in the PNJL model (see Fig. 2.6), where the isothermal critical temperature in the

PNJL model is about 120 MeV and the isentropic critical temperature is about 80 MeV. These results indicate that an isolated system is less likely to go through a first-order phase transition than an opened one. Nevertheless, the minimum v^2 in both cases is about -0.1, which is larger than that in Refs.[39, 55, 56], and this is the reason for the slower growth rate of unstable modes in our study than in theirs. Our results could become similar to theirs if we increase the attractive interactions among quarks by using large values for G_S and K. A more detailed discussion on the dispersion relation of unstable modes in baryon-rich quark matter will be given in Section 3 by using the linear response theory, which also allows the quantum effects to be included.

3. SPINODAL INSTABILITIES IN BARYON-RICH QUARK MATTER*

In systems that have a first-order phase transition, large density fluctuations can appear as a result of spinodal instabilities. Various methods have been used in studying the growth rate of such instabilities in a variety of systems. For example, this has been investigated for the liquid-gas phase transition in asymmetric nuclear matter by solving the linearized Dirac equation [57] or Vlasov equation [58] in the mean-field approximation. In this section, we study the development of spinodal instabilities in baryon-rich quark matter by using the linear response theory and its semi-classical limit, the linear Boltzmann equation. We will see that both approaches agree if the wavelength of the density fluctuation is large.

3.1 The linear response theory

Linear response theory has been widely used in calculating the transport coefficients, such as the electric conductivity and viscosity, of many-body systems. It describes how an equilibrium system responds to certain perturbations. Although the perturbations are in general external, such as an external electric field or the gradient of an external flow field, the perturbation for studying spinodal instabilities is generated internally from the fluctuations that drive the system away from equilibrium. In Section 3.1.1, we describe the theoretical framework on which the linear response theory is based. The matrix elements of the retarded correlator, which are needed for describing the response of a system, are then calculated in Section 3.1.2.

*Reprinted from Feng Li and Che-Ming Ko, 2016, Spinodal instabilities of baryon-rich quark-gluon plasma in the Polyakov–Nambu–Jona–Lasinio model, Phys. Rev. C 93:035205

Several results, such as the spinodal instability region and the growth rate of unstable modes, are shown in Section 3.1.3. Although the long-time behavior of spinodal instabilities will be studied in Sections 4 and 5 by numerically solving the semiclassical transport equation, it is still useful to first examine their early time behavior. Also, analytic results presented in this section can be used to check the accuracy of numerical calculations. Furthermore, the linear response theory allows the inclusion of quantum effects on spinodal instability, which is absent in the semi-classical transport approach.

3.1.1 Theoretical framework

When a many-body system is slightly perturbed, the deviation of a physical observable from its equilibrium value is linearly proportional to the perturbation. Since spinodal instabilities are self-induced, an observable will deviate further from its equilibrium value once the deviation starts. Therefore, the perturbation is proportional to the fluctuation itself with the proportionality coefficient given by the retarded correlator between this observable and the perturbation that is evaluated in the equilibrium state [59]. These coefficients can be calculated by applying the Kubo-Martin-Schwinger (KMS) condition [60], i.e., the retarded correlator is the analytical continuation of the Matsubara correlator in energy and can be calculated in the imaginary time approach.

Such a system can be described by the Hamiltonian: $H = H_0 + H'$, where H_0 is its Hamiltonian at equilibrium, and H' is the perturbation driving the system away from equilibrium. In the Schroedinger picture, the density matrix of the system, defined as $\rho \equiv p_i|\psi_i\rangle\langle\psi_i|$ with p_i denoting the probability of the system in state $|\psi_i\rangle$,

evolves in time according to

$$\rho(t) = \mathcal{U}(t,t_0)\rho(t_0)\mathcal{U}^\dagger(t,t_0), \tag{3.1}$$

where

$$\begin{aligned}\mathcal{U}(t,t_0) &\equiv Te^{-i\int_{t_0}^{t} d\bar{t}H(\bar{t})} \\ &= \sum_{n=0}^{\infty}(-i)^n\int_{t_0}^{t}dt_1\int_{t_0}^{t_1}dt_2\cdots\int_{t_0}^{t_{n-1}}dt_n H(t_1)H(t_2)\cdots H(t_n)\end{aligned} \tag{3.2}$$

is the time evolution operator from the initial time t_0 to time t. Since

$$\mathcal{U}^\dagger(t,t_0)\mathcal{U}(t,t_0) = 1, \tag{3.3}$$

and

$$\mathcal{U}(t_2,t_0) = \mathcal{U}(t_2,t_1)\mathcal{U}(t_1,t_0) \tag{3.4}$$

for $t_2 > t_1 > t_0$, we can expand $\mathcal{U}(t,t_0)$ in terms of the perturbation H':

$$\begin{aligned}&\mathcal{U}(t,t_0) \\ =\ &\sum_{n=0}^{\infty}(-i)^n\int_{t_0}^{t}dt_1\int_{t_0}^{t_1}dt_2\cdots\int_{t_0}^{t_{n-1}}dt_n(H_0(t_1)+H'(t_1))(H_0(t_2)+H'(t_2)) \\ &\times\cdots(H_0(t_n)+H'(t_n)) \\ =\ &\sum_{n=0}^{\infty}(-i)^n\int_{t_0}^{t}dt_1\int_{t_0}^{t_1}dt_2\cdots\int_{t_0}^{t_{n-1}}dt_n H_0(t_1)H_0(t_2)\cdots H_0(t_n) \\ &+\sum_{n=0}^{\infty}\sum_{k=1}^{n}(-i)^n\int_{t_0}^{t}dt_1\int_{t_0}^{t_1}dt_2\cdots\int_{t_0}^{t_{k-1}}dt_k\cdots\int_{t_0}^{t_{n-1}}dt_n H_0(t_1)H_0(t_2)\cdots H'(t_k) \\ &\times\cdots H_0(t_n)+\mathcal{O}(H'^2) \\ =\ &\mathcal{U}_0(t,t_0) - i\int_{t_0}^{t}dt'\sum_{m=0}^{\infty}(-i)^m\int_{t'}^{t}dt_1\int_{t'}^{t_1}dt_2\cdots\int_{t'}^{t_{m-1}}dt_m H_0(t_1)H_0(t_2)\cdots H_0(t_m)\end{aligned}$$

$$
\begin{aligned}
&\times H'(t')\sum_{n=0}^{\infty}(-i)^n\int_{t_0}^{t'}d\bar{t}_1\int_{t_0}^{\bar{t}_1}d\bar{t}_2\cdots\int_{t_0}^{\bar{t}_{n-1}}d\bar{t}_n H_0(\bar{t}_1)H_0(\bar{t}_2)\cdots H_0(\bar{t}_n)+\mathcal{O}(H'^2)\\
=\;& \mathcal{U}_0(t,t_0)-i\int_{t_0}^{t}dt'\mathcal{U}_0(t,t')H'(t')\mathcal{U}_0(t',t_0)+\mathcal{O}(H'^2),
\end{aligned}
\tag{3.5}
$$

where

$$
\mathcal{U}_0(t,t_0)\equiv Te^{-i\int_{t_0}^{t}d\bar{t}H_0(\bar{t})} \tag{3.6}
$$

is the time evolution operator in the absence of perturbations. Therefore, the density matrix of the system at time t is

$$
\begin{aligned}
\rho(t) &= \mathcal{U}(t,t_0)\rho(t_0)\mathcal{U}^{\dagger}(t,t_0)\\
&= \left(\mathcal{U}_0(t,t_0)-i\int_{t_0}^{t}dt'\mathcal{U}_0(t,t')H'(t')\mathcal{U}_0(t',t_0)\right)\rho(t_0)\\
&\quad\times\left(\mathcal{U}_0^{\dagger}(t,t_0)+i\int_{t_0}^{t}dt'\mathcal{U}_0^{\dagger}(t',t_0)H'(t')\mathcal{U}_0^{\dagger}(t,t')\right)\mathcal{O}(H'^2)\\
&= \mathcal{U}_0(t,t_0)\left(\rho(t_0)-i\int_{t_0}^{t}dt'\left(\mathcal{U}_0^{\dagger}(t',t_0)H'(t')\mathcal{U}_0(t',t_0)\rho(t_0)\right.\right.\\
&\quad\left.\left.-\rho(t_0)\mathcal{U}_0^{\dagger}(t',t_0)H'(t')\mathcal{U}_0(t',t_0)\right)\right)\mathcal{U}_0^{\dagger}(t,t_0)\mathcal{O}(H'^2)\\
&= \rho_0(t)-i\int_{t_0}^{t}dt'\mathcal{U}_0(t,t_0)[H_I'(t'),\rho(t_0)]\mathcal{U}_0^{\dagger}(t,t_0)+\mathcal{O}(H'^2),
\end{aligned}
\tag{3.7}
$$

where

$$
\rho_0(t)=\mathcal{U}_0(t,t_0)\rho(t_0)\mathcal{U}_0^{\dagger}(t,t_0) \tag{3.8}
$$

is the density matrix of the system at time t in the absence of perturbations, and

$$
H_I'(t')=\mathcal{U}_0^{\dagger}(t',t_0)H'(t')\mathcal{U}_0(t',t_0) \tag{3.9}
$$

is the perturbation expressed in the interaction picture. The third equality in Eq. (3.7) is obtained by using the unitarity (Eq.(3.3)) and the composition property (Eq. (3.4)) of the time evolution operator $\mathcal{U}$.

The time dependence of the expectation value of a physical observable A is then given by

$$\begin{aligned}\langle A(t)\rangle &= \mathrm{tr}[\rho(t)A_S] \\ &= \mathrm{tr}\left[\rho_0(t)A_S - i\int_{t_0}^{t} dt'[H_I'(t'),\rho(t_0)]A_I(t)\right] + \mathcal{O}(H'^2) \\ &= \langle A_0(t)\rangle + i\int_{t_0}^{t} dt'\mathrm{tr}\left[\rho(t_0)[H_I'(t'),A_I(t)]\right] + \mathcal{O}(H'^2), \end{aligned} \tag{3.10}$$

where the subscript S refers to the Schroedinger picture. The second and third equalities in Eq. (3.10) are obtained by employing the cyclic property of trace. Without loss of generality, we assume that the system is initially at equilibrium, namely, $\rho(t_0) = \rho_0$, then

$$\delta\langle A(t)\rangle = i\int dt'\theta(t-t')\langle[H_I'(t'),A_I(t)]\rangle_0, \tag{3.11}$$

where the right hand side is the retarded correlator evaluated with the system in an equilibrium state. Although the correlator generally depends on both t and t', it can be reduced to a function of $t-t'$ for an equilibrium system.

Since spinodal instabilities are self induced, the perturbation H_I' is just composed of the fluctuations of the mean fields, that is

$$H_I' = \int d^3\mathbf{x}\left[\bar{u}u\delta M_u + \bar{d}d\delta M_d + \bar{s}s\delta M_s + 2G_V\delta j_\mu(\bar{u}\gamma^\mu u + \bar{d}\gamma^\mu d + \bar{s}\gamma^\mu s)\right], \tag{3.12}$$

where the mass fluctuations given by

$$\begin{aligned}
\delta M_u &= -2G_S\delta\langle\bar{u}u\rangle - 2K\langle\bar{s}s\rangle\delta\langle\bar{d}d\rangle - 2K\langle\bar{d}d\rangle\delta\langle\bar{s}s\rangle, \\
\delta M_d &= -2G_S\delta\langle\bar{d}d\rangle - 2K\langle\bar{s}s\rangle\delta\langle\bar{u}u\rangle - 2K\langle\bar{u}u\rangle\delta\langle\bar{s}s\rangle, \\
\delta M_s &= -2G_S\delta\langle\bar{s}s\rangle - 2K\langle\bar{u}u\rangle\delta\langle\bar{d}d\rangle - 2K\langle\bar{d}d\rangle\delta\langle\bar{u}u\rangle. \qquad (3.13)
\end{aligned}$$

The fluctuations in the condensates $\langle\bar{u}u\rangle$, $\langle\bar{d}d\rangle$ and $\langle\bar{s}s\rangle$ as well as in the current density j^μ can then be obtained from Eq. (3.11), and they are

$$\begin{aligned}
\delta\langle\bar{q}q\rangle_x &= -i\int d^4x'\Big\{\chi_{\sigma\sigma}(x-x';M_u)[(-2G_S - 2K\langle\bar{s}s\rangle_{x'})\delta\langle\bar{q}q\rangle_{x'} \\
&\qquad - 2K\langle\bar{q}q\rangle_{x'}\delta\langle\bar{s}s\rangle_{x'}] + 2G_V\chi^\mu_{\sigma j}(x-x';M_u)\delta j_\mu(x')\Big\}, \\
\delta\langle\bar{s}s\rangle_x &= -i\int d^4x'\Big\{\chi_{\sigma\sigma}(x-x';M_s)\,[-4K\langle\bar{q}q\rangle_{x'}\delta\langle\bar{q}q\rangle_{x'} - 2G_S\delta\langle\bar{s}s\rangle_{x'}] \\
&\qquad + 2G_V\chi^\mu_{\sigma j}(x-x';M_s)\delta j_\mu(x')\Big\}, \\
\delta j^\mu(x) &= -i\int d^4x'\Big\{[2\chi^\mu_{\sigma j}(x-x';M_u)(-2G_S - 2K\langle\bar{s}s\rangle_{x'}) \\
&\qquad - 4K\chi^\mu_{\sigma j}(x-x';M_s)\langle\bar{q}q\rangle_{x'}]\delta\langle\bar{q}q\rangle_{x'} \\
&\qquad + \left[-4K\chi^\mu_{\sigma j}(x-x';M_u)\langle\bar{q}q\rangle_{x'} - 2G_S\chi^\mu_{\sigma j}(x-x';M_s)\right]\delta\langle\bar{s}s\rangle_{x'} \\
&\qquad + 2G_V(2\chi^{\mu\nu}_{jj}(x-x';M_u) + \chi^{\mu\nu}_{jj}(x-x';M_s))\delta j_\nu(x')\Big\}, \qquad (3.14)
\end{aligned}$$

where

$$\begin{aligned}
\chi_{\sigma\sigma}(x) &\equiv \theta(t)\langle[\bar{q}(x)q(x),\bar{q}(0)q(0)]\rangle_0, \\
\chi^\mu_{\sigma j}(x) &\equiv \theta(t)\langle[\bar{q}(x)\gamma^\mu q(x),\bar{q}(0)q(0)]\rangle_0, \\
\chi^{\mu\nu}_{jj}(x) &\equiv \theta(t)\langle[\bar{q}(x)\gamma^\mu q(x),\bar{q}(0)\gamma^\nu q(0)]\rangle_0, \qquad (3.15)
\end{aligned}$$

and $\langle\bar{q}q\rangle \equiv \langle\bar{u}u\rangle = \langle\bar{d}d\rangle$ represents the light quark condensates, since we have taken

u and d quarks to have the same bare mass and assumed that the quark matter is isospin symmetric.

Taking the Fourier transformation of the equations in Eq. (3.14) and moving all terms on the left side to the right side, we obtain

$$\begin{aligned}
0 &= (1 - i\widetilde{\chi}_{\sigma\sigma}(k; M_u)(2G_S + 2K\langle\bar{s}s\rangle))\,\delta\langle\bar{q}q\rangle_k \\
&\quad -2Ki\widetilde{\chi}_{\sigma\sigma}(k; M_u)\langle\bar{q}q\rangle\delta\langle\bar{s}s\rangle_k + 2G_V i\widetilde{\chi}^{\mu}_{\sigma j}(k; M_u)\delta j_\mu(k), \\
0 &= -4Ki\widetilde{\chi}_{\sigma\sigma}(k; M_s)\langle\bar{q}q\rangle\delta\langle\bar{q}q\rangle_k + (1 - 2G_S i\widetilde{\chi}_{\sigma\sigma}(k; M_s))\,\delta\langle\bar{s}s\rangle_k \\
&\quad +2G_V i\widetilde{\chi}^{\mu}_{\sigma j}(k; M_s)\delta j_\mu(k), \\
0 &= -i\left(2\widetilde{\chi}^{\mu}_{\sigma j}(k; M_u)(2G_S + 2K\langle\bar{s}s\rangle) + 4K\widetilde{\chi}^{\mu}_{\sigma j}(k; M_s)\langle\bar{q}q\rangle\right)\delta\langle\bar{q}q\rangle_k \\
&\quad -i\left(4K\widetilde{\chi}^{\mu}_{\sigma j}(k; M_u)\langle\bar{q}q\rangle + 2G_S\widetilde{\chi}^{\mu}_{\sigma j}(k; M_s)\right)\delta\langle\bar{s}s\rangle_k \\
&\quad + \left(g^{\mu\nu} + i2G_V(2\widetilde{\chi}^{\mu\nu}_{jj}(k; M_u) + \widetilde{\chi}^{\mu\nu}_{jj}(k; M_s))\right)\delta j_\nu(k),
\end{aligned} \tag{3.16}$$

with

$$\widetilde{\chi}(k) = \int d^4x\chi(x)e^{ikx}. \tag{3.17}$$

The equations in Eq.(3.16) have non-zero solutions if and only if

$$\det\begin{vmatrix} A_{11} & A_{12} & A_{13} \\ A_{21} & A_{22} & A_{23} \\ A_{31} & A_{32} & A_{33} \end{vmatrix} = 0, \tag{3.18}$$

where

$$\begin{aligned}
A_{11} &= 1 - i\widetilde{\chi}_{\sigma\sigma}(k^0, \mathbf{k}; M_u)(2G_S + 2K\langle\bar{s}s\rangle), \\
A_{12} &= -2iK\widetilde{\chi}_{\sigma\sigma}(k^0, \mathbf{k}; M_u)\langle\bar{q}q\rangle,
\end{aligned}$$

$$
\begin{aligned}
A_{13} &= 2iG_V\widetilde{\chi}^{\mu}_{\sigma j}(k^0,\mathbf{k};M_u),\\
A_{21} &= -4iK\widetilde{\chi}_{\sigma\sigma}(k^0,\mathbf{k};M_s)\langle\bar{q}q\rangle,\\
A_{22} &= 1-2iG_S\widetilde{\chi}_{\sigma\sigma}(k^0,\mathbf{k};M_s),\\
A_{23} &= 2iG_V\widetilde{\chi}^{\mu}_{\sigma j}(k^0,\mathbf{k};M_s),\\
A_{31} &= -2i\widetilde{\chi}^{\mu}_{\sigma j}(k^0,\mathbf{k};M_u)(2G_S+2K\langle\bar{s}s\rangle)+4iK\widetilde{\chi}^{\mu}_{\sigma j}(k^0,\mathbf{k};M_s)\langle\bar{q}q\rangle,\\
A_{32} &= -4iK\widetilde{\chi}^{\mu}_{\sigma j}(k^0,\mathbf{k};M_u)\langle\bar{q}q\rangle+2iG_S\widetilde{\chi}^{\mu}_{\sigma j}(k^0,\mathbf{k};M_s),\\
A_{33} &= g^{\mu\nu}+i2G_V(2\widetilde{\chi}^{\mu\nu}_{jj}(k^0,\mathbf{k};M_u)+i\widetilde{\chi}^{\mu\nu}_{jj}(k^0,\mathbf{k};M_s))
\end{aligned}
\tag{3.19}
$$

Details on the calculation of quark correlators $\widetilde{\chi}(\mathbf{k})$ in the above equation are given in Section 3.1.2 and Appendix B. Since the quark correlators are either even or odd functions of ω as discussed in Section 3.1.2, the determinant in Eq. (3.18) is even in ω, i.e., both $\omega=\omega_{\mathbf{k}}$ and $\omega=-\omega_{\mathbf{k}}$ are solutions. For unstable modes, corresponding to imaginary ω, i.e., $\omega_{\mathbf{k}}=i\Gamma_k$, the imaginary frequency $\omega=i\Gamma_k$ and $\omega=-i\Gamma_k$ then correspond to unstable modes that grow and decay exponentially in time with a growth or decay rate Γ_k.

3.1.2 The correlators

In this subsection, we calculate the correlators χs defined in Eq. (3.15) in the leading order. The retarded correlator $\widetilde{\chi}$ is related to the Matsubara correlator Π by the Kubo-Martin-Schwinger (KMS) condition [60] $\widetilde{\chi}(k)=-i\Pi(k^0+i0^+,\mathbf{k})$, where in the leading order,

$$
\begin{aligned}
\Pi_{\sigma\sigma}(i\nu_n,\mathbf{k}) &= -T\sum_{a=1}^{3}\sum_{\omega_n}\int_{|\mathbf{p}|<\Lambda}^{|\mathbf{k}+\mathbf{p}|<\Lambda}\frac{\mathrm{d}^3\mathbf{p}}{(2\pi)^3}\mathrm{Tr}[\widetilde{S}_a(i\omega_n,\mathbf{p})\widetilde{S}_a(i\omega_n+i\nu_n,\mathbf{k}+\mathbf{p})],\\
\Pi^{\mu\nu}_{jj}(i\nu_n,\mathbf{k}) &= -T\sum_{a=1}^{3}\sum_{\omega_n}\int_{|\mathbf{p}|<\Lambda}^{|\mathbf{k}+\mathbf{p}|<\Lambda}\frac{\mathrm{d}^3\mathbf{p}}{(2\pi)^3}\mathrm{Tr}[\gamma^{\mu}\widetilde{S}_a(i\omega_n,\mathbf{p})\gamma^{\nu}\widetilde{S}_a(i\omega_n+i\nu_n,\mathbf{k}+\mathbf{p})],
\end{aligned}
$$

$$\Pi^{\mu}_{\sigma j}(i\nu_n, \mathbf{k}) = -T\sum_{a=1}^{3}\sum_{\omega_n}\int_{|\mathbf{p}|<\Lambda}^{|\mathbf{k}+\mathbf{p}|<\Lambda}\frac{\mathrm{d}^3\mathbf{p}}{(2\pi)^3}\mathrm{Tr}[\widetilde{S}_a(i\omega_n, \mathbf{p})\gamma^{\mu}\widetilde{S}_a(i\omega_n + i\nu_n, \mathbf{k}+\mathbf{p})], \tag{3.20}$$

with the Matsubara frequency $\omega_n = (2n+1)\pi T$, $\nu_n = 2n\pi T$, and $\widetilde{S}_a$ is the quark propagator in the imaginary time formalism. The subscript a is the color index, and each color is treated separately as the background color field in the PNJL model contributes differently to the chemical potentials of quarks of different colors. Eq. (3.20) can be expressed in a more compact form as

$$\Pi(i\nu_n, \mathbf{k}) = T\sum_{a=1}^{3}\sum_{\omega_n}\int_{|\mathbf{p}|<\Lambda}^{|\mathbf{k}+\mathbf{p}|<\Lambda}\frac{\mathrm{d}^3\mathbf{p}}{(2\pi)^3}\mathrm{Tr}[\mathcal{O}_1\widetilde{S}_a(i\omega_n, \mathbf{p})\mathcal{O}_2\widetilde{S}_a(i\omega_n + i\nu_n, \mathbf{k}+\mathbf{p})], \tag{3.21}$$

where $\mathcal{O}_{1,2}$ are unit or gamma matrices.

According to the KMS condition, the quark propagator $\widetilde{S}_a(i\omega_n, \mathbf{p})$ is written in terms of the quark spectral function $\widetilde{\mathcal{A}}_a(p)$,

$$\widetilde{S}_a(i\omega_n, \mathbf{p}) = -\int\frac{dp^0}{2\pi}\frac{\widetilde{\mathcal{A}}_a(p)}{i\omega_n - p^0}, \tag{3.22}$$

where

$$\widetilde{\mathcal{A}}_a(p) \equiv \int d^4x\mathcal{A}_a(x)e^{ipx/\hbar} \equiv \int d^4x\{q_a(x), \bar{q}_a(0)\}e^{ipx/\hbar}. \tag{3.23}$$

Under the quasi-particle approximation, the quark spectral function can be written as

$$\widetilde{\mathcal{A}}_a(p) = \pi[\Delta_+(\mathbf{p})\delta(p^0 + \widetilde{\mu}_a - E_{\mathbf{p}}) - \Delta_-(\mathbf{p})\delta(p^0 + \widetilde{\mu}_a + E_{\mathbf{p}})], \tag{3.24}$$

where

$$\Delta_{\pm}(\mathbf{p}) = \pm\gamma^0 - \frac{\mathbf{p}}{E_{\mathbf{p}}}\cdot\boldsymbol{\gamma} + \frac{M}{E_{\mathbf{p}}}, \tag{3.25}$$

and $\tilde{\mu}_{1,2} = \mu - 2G_V j^0 \pm i\phi_3$ and $\tilde{\mu}_3 = \mu - 2G_V j^0$ are effective chemical potentials. We therefore have

$$\begin{aligned}\Pi(i\nu_n, \mathbf{k}) &= \sum_{a=1}^{3} \int_{|\mathbf{p}|<\Lambda}^{|\mathbf{k}+\mathbf{p}|<\Lambda} \frac{\mathrm{d}^3\mathbf{p}}{(2\pi)^3} \int \frac{dp^0}{2\pi}\frac{dp^{0\prime}}{2\pi} \mathrm{Tr}[\mathcal{O}_1 \widetilde{\mathcal{A}}_a(p^0, \mathbf{p}) \mathcal{O}_2 \widetilde{\mathcal{A}}_a(p^{0\prime}, \mathbf{k}+\mathbf{p})] \\ &\quad \times T\sum_{\omega_n} \frac{-1}{(i\omega_n - p^0)(i\omega_n + i\nu_n - p^{0\prime})}. \end{aligned} \tag{3.26}$$

The summation over the Matsubara frequency ω_n can be evaluated as follows:

$$\begin{aligned} & T\sum_{\omega_n} \frac{-1}{(i\omega_n - p^0)(i\omega_n + i\nu_n - p^{0\prime})} \\ = \;& \frac{-1}{p^{0\prime} - p^0 - i\nu_n} \left(T\sum_{\omega_n} \frac{1}{i\omega_n + i\nu_n - p^{0\prime}} - T\sum_{\omega_n} \frac{1}{i\omega_n - p^0} \right) \\ = \;& \frac{-1}{p^{0\prime} - p^0 - i\nu_n} \frac{1}{2\pi i} \int_{-i\infty+0^+}^{i\infty+0^+} dz \Big(\frac{1}{z + i\nu_n - p^{0\prime}} + \frac{1}{-z + i\nu_n - p^{0\prime}} \\ & - \frac{1}{z - p^0} - \frac{1}{-z - p^0} \Big) \times \left(\frac{1}{2} - f_0(z) \right) \\ = \;& \frac{f_0(p^0) - f_0(p^{0\prime})}{p^{0\prime} - p^0 - i\nu_n}, \end{aligned} \tag{3.27}$$

where $f_0(x) = (\exp(x/T)+1)^{-1}$ is the Fermi-Dirac distribution function. In obtaining the second equality in Eq. (3.27), we have used the fact that the function $1/2 - f_0(z)$ has simple poles at $z = (2n+1)\pi i T$ with the same residue T. The third equality follows after using the relation $f_0(x + i\nu_n) = f_0(x)$.

In all above equations, we have taken the Plank constant $\hbar = 1$. Including explicitly $\hbar$, Eq. (3.26) can be rewritten as

$$\begin{aligned} & i\widetilde{\chi}(\omega, \mathbf{k}) = \Pi(\hbar\omega + i0^+, \hbar\mathbf{k}) \\ = \;& \frac{1}{4} \sum_{a=1}^{3} \int_{|\mathbf{p}|<\Lambda}^{|\hbar\mathbf{k}+\mathbf{p}|<\Lambda} \frac{\mathrm{d}^3\mathbf{p}}{(2\pi)^3} \end{aligned}$$

$$
\begin{aligned}
&\Big\{\mathrm{Tr}[\mathcal{O}_1\Delta_+(\mathbf{p})\mathcal{O}_2\Delta_+(\hbar\mathbf{k}+\mathbf{p})]\frac{f_0(E_{\mathbf{p}}-\widetilde{\mu}_a)-f_0(E_{\mathbf{p}+\hbar\mathbf{k}}-\widetilde{\mu}_a)}{E_{\mathbf{p}+\hbar\mathbf{k}}-E_{\mathbf{p}}-\hbar\omega-i0^+}\\
&+\mathrm{Tr}[\mathcal{O}_1\Delta_-(\mathbf{p})\mathcal{O}_2\Delta_-(\hbar\mathbf{k}+\mathbf{p})]\frac{f_0(E_{\mathbf{p}+\hbar\mathbf{k}}+\widetilde{\mu}_a)-f_0(E_{\mathbf{p}}+\widetilde{\mu}_a)}{E_{\mathbf{p}}-E_{\mathbf{p}+\hbar\mathbf{k}}-\hbar\omega-i0^+}\\
&-\mathrm{Tr}[\mathcal{O}_1\Delta_+(\mathbf{p})\mathcal{O}_2\Delta_-(\hbar\mathbf{k}+\mathbf{p})]\frac{f_0(E_{\mathbf{p}+\hbar\mathbf{k}}+\widetilde{\mu}_a)+f_0(E_{\mathbf{p}}-\widetilde{\mu}_a)-1}{-E_{\mathbf{p}}-E_{\mathbf{p}+\hbar\mathbf{k}}-\hbar\omega-i0^+}\\
&-\mathrm{Tr}[\mathcal{O}_1\Delta_-(\mathbf{p})\mathcal{O}_2\Delta_+(\hbar\mathbf{k}+\mathbf{p})]\frac{1-f_0(E_{\mathbf{p}+\hbar\mathbf{k}}-\widetilde{\mu}_a)-f_0(E_{\mathbf{p}}+\widetilde{\mu}_a)}{E_{\mathbf{p}}+E_{\mathbf{p}+\hbar\mathbf{k}}-\hbar\omega-i0^+}\Big\}.
\end{aligned}
\tag{3.28}
$$

After making the variable change $\mathbf{p}'=-\mathbf{p}-\hbar\mathbf{k}$ in terms containing $f_0(E_{\mathbf{p}+\hbar\mathbf{k}}\pm\widetilde{\mu}^a)$, which also satisfies $|\mathbf{p}'|<\Lambda$ and $|\mathbf{p}'+\hbar\mathbf{k}|<\Lambda$, and writing $\mathbf{p}'$ again as $\mathbf{p}$, Eq. (3.15) becomes

$$
\begin{aligned}
&i\widetilde{\chi}(\omega,\mathbf{k})\\
=\;&\frac{1}{4}\sum_{a=1}^{3}\int_{|\mathbf{p}|<\Lambda}^{|\hbar\mathbf{k}+\mathbf{p}|<\Lambda}\frac{\mathrm{d}^3\mathbf{p}}{(2\pi)^3}\\
&\Big\{\Big(\frac{\mathrm{Tr}[\mathcal{O}_1\Delta_+(\mathbf{p})\mathcal{O}_2\Delta_+(\hbar\mathbf{k}+\mathbf{p})]}{E_{\mathbf{p}+\hbar\mathbf{k}}-E_{\mathbf{p}}-\hbar\omega-i0^+}+\frac{\mathrm{Tr}[\mathcal{O}_1\Delta_+(-\mathbf{p}-\hbar\mathbf{k})\mathcal{O}_2\Delta_+(-\mathbf{p})]}{E_{\mathbf{p}+\hbar\mathbf{k}}-E_{\mathbf{p}}+\hbar\omega+i0^+}\\
&+\frac{\mathrm{Tr}[\mathcal{O}_1\Delta_+(\mathbf{p})\mathcal{O}_2\Delta_-(\hbar\mathbf{k}+\mathbf{p})]}{E_{\mathbf{p}}+E_{\mathbf{p}+\hbar\mathbf{k}}+\hbar\omega+i0^+}+\frac{\mathrm{Tr}[\mathcal{O}_1\Delta_-(-\mathbf{p}-\hbar\mathbf{k})\mathcal{O}_2\Delta_+(-\mathbf{p})]}{E_{\mathbf{p}}+E_{\mathbf{p}+\hbar\mathbf{k}}-\hbar\omega-i0^+}\Big)f_0(E_{\mathbf{p}}-\widetilde{\mu}_a)\\
&+\Big(\frac{\mathrm{Tr}[\mathcal{O}_1\Delta_-(-\mathbf{p}-\hbar\mathbf{k})\mathcal{O}_2\Delta_-(-\mathbf{p})]}{E_{\mathbf{p}+\hbar\mathbf{k}}-E_{\mathbf{p}}-\hbar\omega-i0^+}+\frac{\mathrm{Tr}[\mathcal{O}_1\Delta_-(\mathbf{p})\mathcal{O}_2\Delta_-(\hbar\mathbf{k}+\mathbf{p})]}{E_{\mathbf{p}+\hbar\mathbf{k}}-E_{\mathbf{p}}+\hbar\omega+i0^+}\\
&+\frac{\mathrm{Tr}[\mathcal{O}_1\Delta_-(\mathbf{p})\mathcal{O}_2\Delta_+(\hbar\mathbf{k}+\mathbf{p})]}{E_{\mathbf{p}}+E_{\mathbf{p}+\hbar\mathbf{k}}-\hbar\omega+i0^+}+\frac{\mathrm{Tr}[\mathcal{O}_1\Delta_+(-\mathbf{p}-\hbar\mathbf{k})\mathcal{O}_2\Delta_-(-\mathbf{p})]}{E_{\mathbf{p}}+E_{\mathbf{p}+\hbar\mathbf{k}}+\hbar\omega+i0^+}\Big)f_0(E_{\mathbf{p}}+\widetilde{\mu}_a)\\
&-\frac{\mathrm{Tr}[\mathcal{O}_1\Delta_-(\mathbf{p})\mathcal{O}_2\Delta_+(\hbar\mathbf{k}+\mathbf{p})]}{E_{\mathbf{p}}+E_{\mathbf{p}+\hbar\mathbf{k}}-\hbar\omega+i0^+}-\frac{\mathrm{Tr}[\mathcal{O}_1\Delta_+(-\mathbf{p}-\hbar\mathbf{k})\mathcal{O}_2\Delta_-(-\mathbf{p})]}{E_{\mathbf{p}}+E_{\mathbf{p}+\hbar\mathbf{k}}+\hbar\omega+i0^+}\Big\}.
\end{aligned}
\tag{3.29}
$$

We note that if $\mathcal{O}_{1,2}$ are such that $\mathrm{Tr}[\mathcal{O}_1\Delta_\pm(\mathbf{p})\mathcal{O}_2\Delta_\pm(\hbar\mathbf{k}+\mathbf{p})]=\mathrm{Tr}[\mathcal{O}_1\Delta_\pm(-\mathbf{p}-\hbar\mathbf{k})\mathcal{O}_2\Delta_\pm(-\mathbf{p})]$ and $\mathrm{Tr}[\mathcal{O}_1\Delta_\pm(\mathbf{p})\mathcal{O}_2\Delta_\mp(\hbar\mathbf{k}+\mathbf{p})]=\mathrm{Tr}[\mathcal{O}_1\Delta_\mp(-\mathbf{p}-\hbar\mathbf{k})\mathcal{O}_2\Delta_\pm(-\mathbf{p})]$, then $\widetilde{\chi}(\omega,\mathbf{k})=\widetilde{\chi}(-\omega,\mathbf{k})$. On the other hand, if $\mathrm{Tr}[\mathcal{O}_1\Delta_\pm(\mathbf{p})\mathcal{O}_2\Delta_\pm(\hbar\mathbf{k}+\mathbf{p})]=-\mathrm{Tr}[\mathcal{O}_1\Delta_\pm(-\mathbf{p}-\hbar\mathbf{k})\mathcal{O}_2\Delta_\pm(-\mathbf{p})]$ and $\mathrm{Tr}[\mathcal{O}_1\Delta_\pm(\mathbf{p})\mathcal{O}_2\Delta_\mp(\hbar\mathbf{k}+\mathbf{p})]=-\mathrm{Tr}[\mathcal{O}_1\Delta_\mp(-\mathbf{p}-\hbar\mathbf{k})\mathcal{O}_2\Delta_\pm(-\mathbf{p})]$, then $\widetilde{\chi}(\omega,\mathbf{k})=-\widetilde{\chi}(-\omega,\mathbf{k})$. Furthermore, taking the fluctuation in

the current density as a longitudinal wave, i.e., $\delta\mathbf{j} = \delta j_z \hat{\mathbf{k}}$, then terms such as $\widetilde{\chi}^{0x}_{jj}$ vanish. The expressions for remaining $\widetilde{\chi}$s and their semi-classical approximations are given in Appendix B. Among them, $\widetilde{\chi}_{\sigma\sigma}(\omega, \mathbf{k})$, $\widetilde{\chi}^{0}_{\sigma j}(\omega, \mathbf{k})$, $\widetilde{\chi}^{00}_{jj}(\omega, \mathbf{k})$, and $\widetilde{\chi}^{zz}_{jj}(\omega, \mathbf{k})$ are even in ω, while $\widetilde{\chi}^{z}_{\sigma j}(\omega, \mathbf{k})$ and $\widetilde{\chi}^{0z}_{jj}(\omega, \mathbf{k})$ are odd in ω. The determinant in Eq. (3.18) is thus even in ω, i.e., both $\omega = \omega_{\mathbf{k}}$ and $\omega = -\omega_{\mathbf{k}}$ are solutions.

3.1.3 Results

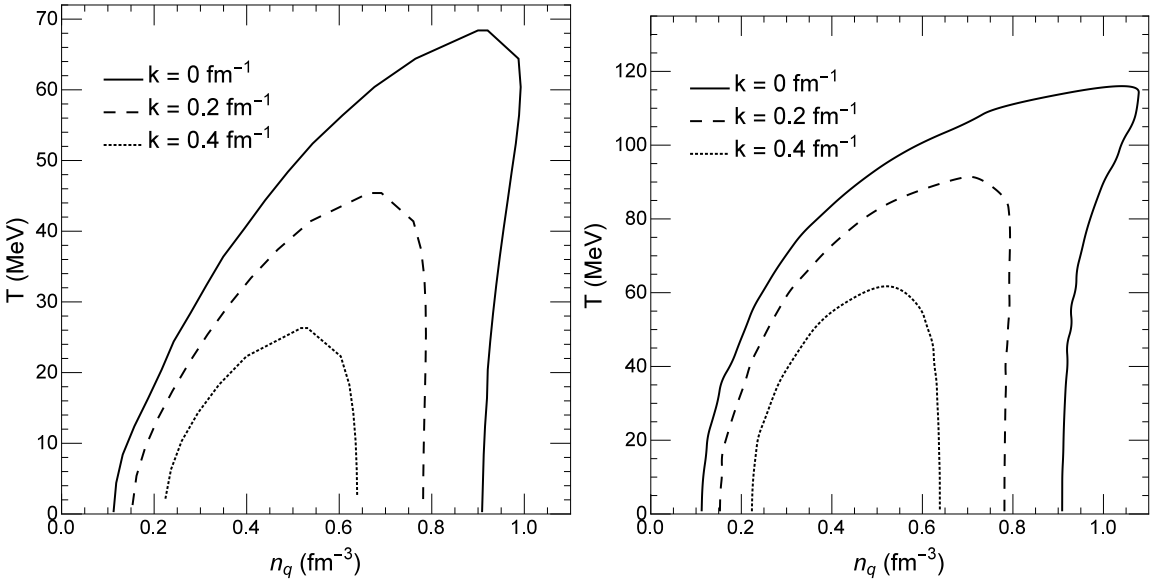

Figure 3.1: Spinodal boundaries of unstable modes of different wave numbers in the temperature and net quark density plane from the NJL model (left window) and the PNJL model (right window) with $G_V = 0$. Taken from Ref. [1]

In this subsection, we show the results obtained from Eq. (3.18) for the spinodal boundaries of longitudinal unstable modes of different wave numbers. Since the determinant in Eq. (3.18) is even in k^0, it has a minimum at $k^0 = 0$. Therefore, for a given wave number k, temperature T, and net baryon density n_q, Eq. (3.18) can

be solved if and only if the determinant is negative or zero when $k^0 = 0$. We can thus obtain the boundaries of the spinodal instability region for different values of k by solving Eq. (3.18) with $k^0 = 0$, and they are shown in the left and right windows of Fig. 3.1 with $G_V = 0$ but with (PNJL) and without (NJL) the Polyakov loop, respectively. It is seen that for unstable modes of a given wave number, the spinodal instability region is larger in the PNJL than in the NJL model due to the effect of the Polyakov loop. The highest temperature T_c of the spinodal instability region is about 68 MeV in the NJL model and 120 MeV in the PNJL model. Comparing these results with the dashed lines shown in Figs. 2.5 and 2.6 based on the thermodynamic approach, we find that the spinodal boundary of unstable modes of $k = 0$ coincides with the boundary determined from $v_T = 0$ but is different from that determined from $v_S = 0$. Therefore, unstable modes in the long wavelength limit correspond to the isothermal spinodal instability, and this is because the time evolution operator $\mathcal{U}(t, t_0)$ in the linear response theory, as shown in Eq. (3.5), becomes non-unitary after linearization, and the entropy of the system no longer remains constant. Our result is different from that in Refs. [55, 61], where the spinodal boundary obtained from solving the linearized hydrodynamic equations in the long wavelength limit is the same as the isentropic one from the thermodynamic approach. On the other hand, the spinodal region in the long wavelength limit in our study coincides with that from the linearized ideal hydrodynamic approach that includes an infinite thermal conductivity [55]. The latter is not surprising since in the linear response approach, the system is not isolated but rather in contact with a thermal bath at constant temperature. However, for a more realistic expanding scenario, this may well be different.

Figure 3.1 also shows that the spinodal instability region shrinks as the wave number of an unstable mode increases or its wavelength becomes shorter. This

indicates that clumps of quark matter or the high density regions are more likely to merge into larger clumps, which correspond to modes of smaller wave number or longer wavelength, and this effect is larger at higher temperatures. According to Refs. [55, 61] based on the linearized ideal hydrodynamic approach, the suppression of high k unstable modes is due to the finite-range interaction between quarks, which leads to a finite surface tension in the interface of two separated phases [62]. As a result, the surface energy of the system is lowered by the merge of density clumps. Although the inter-quark interaction in the PNJL model is zero range, such a surface energy effect is present in the linear response approach as a result of the quantum effect, which leads to a smearing of the particle distribution in space that allows distant particles to interact even if their interaction is of zero range. As shown in Section 3.2 using the linearized Boltzmann equation by taking the classical limit of the quantum linear response theory, the suppression on the growth rate of high k unstable modes indeed goes away.

We have also studied the effect of the vector interaction on the spinodal boundaries of unstable modes of different wave numbers by using $G_V = 0.2\, G_S$ in the PNJL and NJL models, and the results are shown in the left and right windows of Fig. 3.2, respectively. It is seen that the vector interaction shrinks the unstable region, particularly for unstable modes of large wave number or shorter wavelength. For example, the left window of Fig. 3.2 shows that unstable modes with $k \geq 0.2$ fm^{-1} disappear for the NJL model with $G_V = 0.2\, G_S$. The shrinking of the spinodal region or the phase coexistence region, thus the decrease of the growth rates of unstable modes, with increasing vector coupling, is well-known in NJL type models [21]. It also agrees with the expectation that a repulsive interaction drives particles away from density clumps and thus destroys the unstable modes.

We further show in Fig. 3.3 the dispersion relation of unstable modes in the PNJL

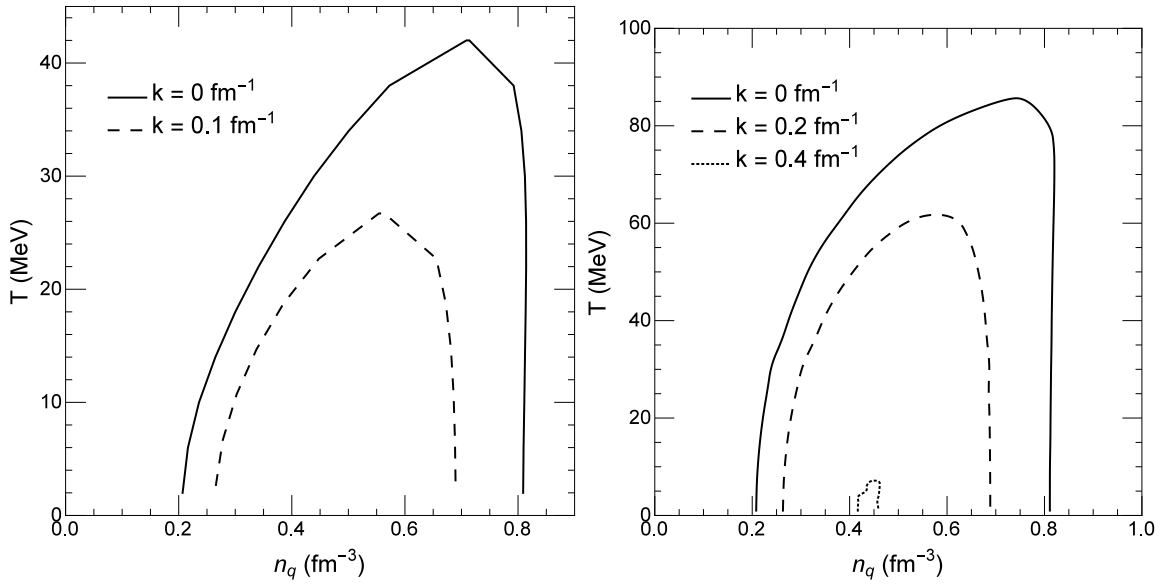

Figure 3.2: Spinodal boundaries of unstable modes of different wave numbers in the temperature and net quark density plane from the NJL model (left window) and the PNJL model (right window) with $G_V = 0.2\ G_S$. Taken from Ref. [1]

model, i.e., its growth rate Γ_k as a function of the wave number k, in quark matter of net quark density $n_q = 0.7$ fm^{-3} and at temperature $T = 70$ MeV, for the cases of $G_V = 0$ (dashed line) and $G_V = 0.2\ G_S$ (solid line). The vector interaction is seen to dramatically reduce the growth rate of unstable modes. For $G_V = 0$, the growth rate peaks at $k = 0.15$ fm^{-1}, implying that the size of the most likely quark clumps due to density fluctuations is about $2\pi/k_{\rm max} \sim 40$ fm. The typical growth rate is 0.01fm^{-1}, indicating that it takes about 100 fm for the fluctuations to grow. This time duration is an order of magnitude longer than typical lifetime of a heavy-ion collision, which is about 10 fm, making the effect of instabilities hardly visible. The instabilities can be enhanced by increasing the attraction interaction between quarks, namely increasing the values of G_S and K. The latter then requires a larger cutoff parameter Λ in order to reproduce the correct meson masses in vacuum. Also,

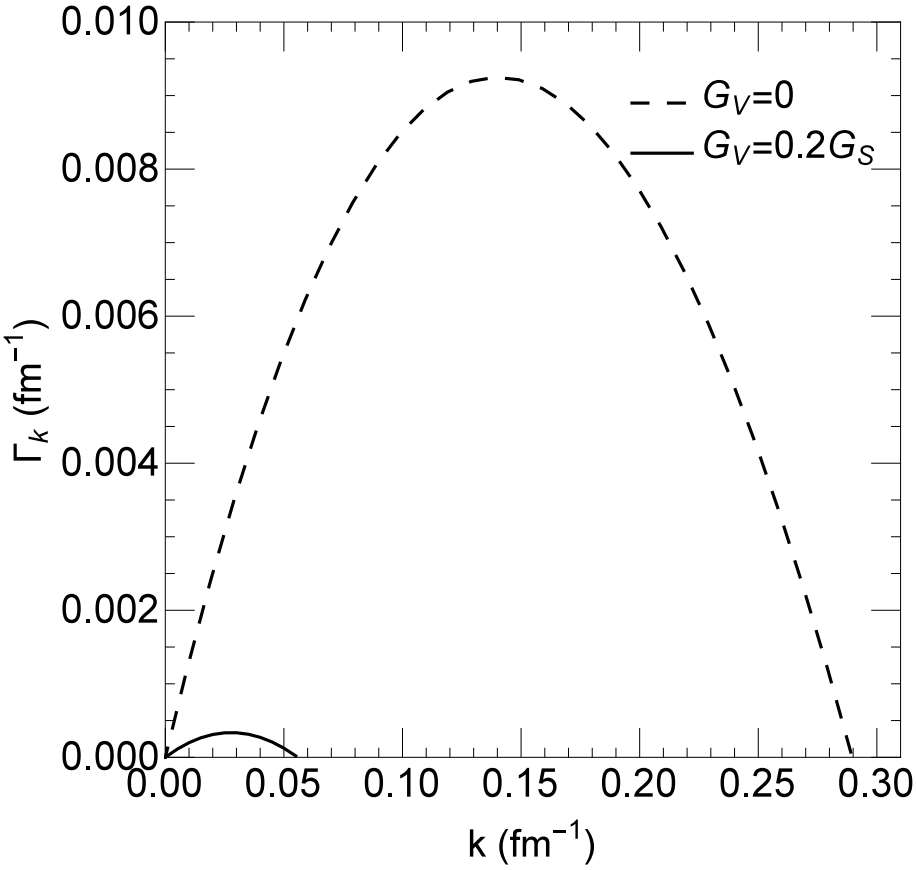

Figure 3.3: Growth rate of unstable modes in quark matter of net quark density $n_q = 0.7$ fm^{-3} and temperature $T = 70$ MeV for both $G_V = 0$ and $G_V = 0.2\ G_S$ based on the PNJL model. Taken from Ref. [1]

nonlinear effects, which are neglected in the linear response theory, may enhance the growth rate of unstable modes and result in appreciable density fluctuations in a much shorter time.

The above growth rate of unstable modes is significantly smaller than that obtained in Ref. [36] based on an ideal fluid dynamics using an equation of state constructed from both hadron and quark phases. As argued in Ref. [39], the growth rate is very different in the Polyakov Quark-Meson (PQM) model [56], which is similar to the PNJL model used in the present study, as a result of drastic differences in

the thermodynamics at the phase boundary between the quark and hadron phases. However, these studies are based on the semi-classical approach and their predictions can be affected by quantum effects as included in the present study.

3.2 Linearized Boltzmann equation

Higher-order corrections, i.e. the collisional effect, to the correlators in Eq.(3.15) obtained in the linear response theory can in principle be included but it is much more involved. For simplicity, we study their effects on the growth rate of unstable modes by using the linearized transport (or Boltzmann) equation, which agrees with the linear response approach in the semiclassical limit. Another advantage of this approach is that the transport equation can be solved by the test-particle method and thus easily used for studying unstable modes of large amplitude, which is the content of Sections 4 and 5. In the present study, we consider the case of the NJL model with vanishing vector interaction, as we already know from Section 3.1 that the vector interaction suppresses spinodal instabilities. The reason for not studying the collisional effect based on the PNJL model is because a consistent treatment of collisional terms in the transport equation is currently not available.

3.2.1 Theoretical framework

The Boltzmann equation for the quark phase space distribution function $f_a(\mathbf{x}, \mathbf{p})$ can be written in a concise form [33],

$$D[f_a] = C[f_z], \tag{3.30}$$

in terms of the drift term

$$D[f_a] \equiv \partial_t f_a + \mathbf{v} \cdot \nabla_{\mathbf{r}} f_a + \frac{M_a}{E_a} \nabla_{\mathbf{r}} V^S \nabla_{\mathbf{p}} f_a, \tag{3.31}$$

where $\mathbf{v} = \mathbf{p}/E_{\mathbf{p}}$ is the velocity, V^S defined in Eq. (C.30) is the scalar potential, and the collision term

$$C[f_a] \equiv \sum_{bcd} \frac{1}{1+\delta_{ab}} \int \frac{d^3\mathbf{p}_b}{(2\pi)^3 2E_b} \frac{d^3\mathbf{p}_c}{(2\pi)^3 2E_c} \frac{d^3\mathbf{p}_d}{(2\pi)^3 2E_d} \frac{(2\pi)^4}{2E_a} \delta^4(p_a + p_b - p_c - p_d) \times |\mathcal{M}_{ab}|^2 \left[f_c f_d (1-f_a)(1-f_b) - f_a f_b (1-f_c)(1-f_d) \right] \tag{3.32}$$

that describes scatterings among quarks. In the above, the subscripts a, b, c, and d denote the spin, flavor, color, and baryon charge of a quark or anti-quark.

Expanding the distribution function f around its equilibrium value f^0, which satisfies the condition $D[f_a^0] = C[f_a^0] = 0$, by writing $f = f^0 + \delta f$ and keeping only terms linear in δf, we obtain

$$D[f_a] \approx \partial_t \delta f_a + \mathbf{v} \cdot \nabla_{\mathbf{r}} \delta f_a + \frac{M_a}{E_a} \nabla_{\mathbf{r}} \delta V^S \nabla_{\mathbf{p}} f_a^0, \tag{3.33}$$

where we have introduced $V^S = V_0^S + \delta V^S$ and used the fact that $\nabla_{\mathrm{r}} V_0^S = 0$ at equilibrium. Similarly, the collision term becomes

$$C[f_a] \approx \sum_{bcd} \int d^3\mathbf{p}_b d^3\mathbf{p}_c d^3\mathbf{p}_d \frac{(2\pi)^{-5} \delta^4(p_a + p_b - p_c - p_d)}{(1+\delta_{ab}) 2E_a 2E_b 2E_c 2E_d} |\mathcal{M}_{ab}|^2 f_a^0 f_b^0 (1 - f_c^0) (1 - f_d^0) \left[-\frac{\delta f_a}{f_a^0(1-f_a^0)} - \frac{\delta f_b}{f_b^0(1-f_b^0)} + \frac{\delta f_c}{f_c^0(1-f_c^0)} + \frac{\delta f_d}{f_d^0(1-f_d^0)} \right]. \tag{3.34}$$

Using the relaxation-time approximation to the collision term, we neglect the contributions from δf_b, δf_c, and δf_d in Eq.(3.34) and rewrite the collision integral as

$$C[f_a] \approx -\frac{1}{\tau_a} \delta f_a \tag{3.35}$$

in terms of the relaxation time τ_a,

$$\frac{1}{\tau_a} = \sum_{bcd} \int d^3\mathbf{p}_b d^3\mathbf{p}_c d^3\mathbf{p}_d \frac{(2\pi)^{-5}\delta^4(p_a + p_b - p_c - p_d)}{(1+\delta_{ab})2E_a 2E_b 2E_c 2E_d} |\mathcal{M}_{ab}|^2 \frac{f_b^0(1-f_c^0)(1-f_d^0)}{1-f_a^0}, \tag{3.36}$$

which characterizes the time for the system to evolve from a non-equilibrium state to an equilibrium one.

After changing variables according to $\mathbf{P} = \mathbf{p}_a + \mathbf{p}_b$, $\mathbf{P}' = \mathbf{p}_c + \mathbf{p}_d$, and $\mathbf{p} = \mathbf{p}_c - \mathbf{p}_d$, and using the relation $d^3\mathbf{p}_b d^3\mathbf{p}_c d^3\mathbf{p}_d = 2^{-3} d^3\mathbf{P} d^3\mathbf{P}' d^3\mathbf{p}$ and $\mathbf{P} = \mathbf{P}'$, Eq.(3.36) becomes

$$\frac{1}{\tau_a} = \sum_{bcd} \int d^3\mathbf{P} d^3\mathbf{p} \frac{(2\pi)^{-5}\delta(E_a + E_b - E_c - E_d)}{(1+\delta_{ab})2^3 2E_a 2E_b 2E_c 2E_d} |\mathcal{M}_{ab}|^2 \frac{f_b^0(1-f_c^0)(1-f_d^0)}{1-f_a^0}. \tag{3.37}$$

Writing

$$\delta(E_a + E_b - E_c - E_d) = \int dE \delta(E_a + E_b - E)\delta(E_c + E_d - E), \tag{3.38}$$

it is then easy to show that for the first δ function, we have

$$\delta(E - E_a - E_b) = \frac{E_b}{P p_a} \delta\left(x - \frac{p_a^2 - p_b^2 + P^2}{2P p_a}\right), \tag{3.39}$$

where x denotes $\cos\angle(\mathbf{P}, \mathbf{p}_a)$. The second δ function is tedious to evaluate unless the colliding particles have same mass. Since we are interested in a quark matter that has temperatures below the critical temperature T_c and net baryon chemical potentials smaller than 1 GeV, very few strange (anti-)quarks are present and the scatterings are mostly among light u and d quarks of similar masses. Taking the

equal mass limit, the second δ function can be expressed as

$$\delta(E_c + E_d - E) = \delta\left(p - E\sqrt{\frac{s-2m^2}{E^2 - P^2x'^2}}\right)\frac{4EE_cE_d}{p(E^2 - P^2x'^2)}, \tag{3.40}$$

with $x' = \cos\angle(\mathbf{P}, \mathbf{p})$ and $s = (p_a + p_b)^2$. Assuming that the scattering cross sections are isotropic, then $|\mathcal{M}_{ab}|^2 = 16\pi s\sigma^{ab}_{\rm CM}$, this leads to

$$\begin{aligned}\frac{1}{\tau_a} = &\sum_{bcd}\frac{1}{(1+\delta_{ab})2(2\pi)^2 p_a E_a(1-f_a^0)}\int dEdPdx' s\sigma^{ab}_{\rm CM}\\ &\frac{PE^2}{E^2 - P^2x'^2}\sqrt{\frac{s-2m^2}{E^2-P^2x'^2}}f_b^0(1-f_c^0)(1-f_d^0).\end{aligned} \tag{3.41}$$

For collisions of u and d quarks only, the summation in the above equation becomes a constant factor: $\sum_{bcd}(1+\delta_{ab})^{-1} = 2$ (spins) $\times$ 3 (colors) $\times$ 2 (flavors) $-$ 1/2 (identical particle) = 11.5 [63].

The linearized transport equation can now be expressed as

$$\partial_t\delta f_a + \mathbf{v}\cdot\nabla_{\mathbf{r}}\delta f_a + \frac{M_a}{E_a}\nabla_{\mathbf{r}}\delta V_a^S\nabla_{\mathbf{p}}f_a^0 + \tau_a^{-1}\delta f_a = 0. \tag{3.42}$$

Introducing the Fourier transform of δf and δV^S,

$$\begin{aligned}\delta\tilde{f}(\mathbf{k},\mathbf{p},\omega) &= \int dtd^3\mathbf{x}\delta f(\mathbf{x},\mathbf{p},t)\exp(i\omega t - i\mathbf{k}\cdot\mathbf{x}),\\ \delta\tilde{V}^S(\mathbf{k},\omega) &= \int dtd^3\mathbf{x}\delta V^S(\mathbf{x},t)\exp(i\omega t - i\mathbf{k}\cdot\mathbf{x}),\end{aligned} \tag{3.43}$$

Eq. (3.42) can be rewritten as

$$(\omega + i\tau_a^{-1} - \mathbf{k}\cdot\mathbf{v}_a)\delta\tilde{f}_a + \frac{M_a}{E_a}\delta\tilde{V}_a^S\mathbf{k}\cdot\nabla_{\mathbf{p}}f_a^0 = 0. \tag{3.44}$$

Since $V_i^S = 2G_S\langle\bar{q}q\rangle_i + 2K\langle\bar{q}q\rangle_j\langle\bar{q}q\rangle_k$ with i,j,k indicating the quark flavors and $i \neq j \neq k$ as in Section 3.1, their variations are given by

$$\begin{aligned}
\delta V_q^S &= (2G_S + 2K\langle\bar{s}s\rangle)\delta\langle\bar{q}q\rangle + 2K\langle\bar{q}q\rangle\delta\langle\bar{s}s\rangle, \\
\delta V_s^S &= 4K\langle\bar{q}q\rangle\delta\langle\bar{q}q\rangle + 2G_S\delta\langle\bar{s}s\rangle,
\end{aligned} \tag{3.45}$$

with q denoting u or d quark. For an isospin symmetric quark matter considered in the present study, u and d quarks have same mass and condensate, we then obtain from Eq. (3.44) the following:

$$\begin{aligned}
\delta f_{q,\bar{q}} &= \frac{2\mathbf{k}\cdot\nabla_{\mathbf{p}} f^0_{q,\bar{q}}(M_q/E_q)[(G_S + K\langle\bar{s}s\rangle)\delta\langle\bar{q}q\rangle + K\langle\bar{q}q\rangle\delta\langle\bar{s}s\rangle]}{\omega + i\tau_q^{-1} - \mathbf{k}\cdot\mathbf{v}}, \\
\delta f_{s,\bar{s}} &\approx \frac{2\mathbf{k}\cdot\nabla_{\mathbf{p}} f^0_{q,\bar{q}}(M_q/E_q)[2K\langle\bar{q}q\rangle\delta\langle\bar{q}q\rangle + G_S\delta\langle\bar{s}s\rangle]}{\omega + i\tau_q^{-1} - \mathbf{k}\cdot\mathbf{v}}.
\end{aligned} \tag{3.46}$$

In the above, we have taken the relaxation time of strange quarks to be the same as that for light quarks for simplicity. Expressing both $\delta\langle\bar{q}q\rangle$ and $\delta\langle\bar{s}s\rangle$ in terms of $\delta f_{q,\bar{q}}$ and $\delta f_{s,\bar{s}}$ according to

$$\begin{aligned}
\delta\langle\bar{q}q\rangle &= 2N_c\int\frac{d^3\mathbf{p}}{(2\pi)^3}\left(\frac{M_q}{E_q}(\delta f_q + \delta f_{\bar{q}}) + \frac{p^2}{E_q^3}(f_q^0 + f_{\bar{q}}^0 - 1)\delta M_q\right), \\
\delta\langle\bar{s}s\rangle &= 2N_c\int\frac{d^3\mathbf{p}}{(2\pi)^3}\left(\frac{M_s}{E_s}(\delta f_s + \delta f_{\bar{s}}) + \frac{p^2}{E_s^3}(f_s^0 + f_{\bar{s}}^0 - 1)\delta M_s\right),
\end{aligned} \tag{3.47}$$

and substituting $\delta\tilde{f}_{q,\bar{q}}$, $\delta\tilde{f}_{s,\bar{s}}$, δM_q, and δM_s in Eq.(3.47), we obtain after some simplifications the following result:

$$\begin{pmatrix} 1 - 2(G_S + K\langle\bar{s}s\rangle)(\chi_q - \xi_q) & -2K\langle\bar{q}q\rangle(\chi_q - \xi_q) \\ -4K\langle\bar{q}q\rangle(\chi_s - \xi_s) & 1 - 2G_S(\chi_s - \xi_s) \end{pmatrix} \begin{pmatrix} \delta\langle\bar{q}q\rangle \\ \delta\langle\bar{s}s\rangle \end{pmatrix} = 0, \tag{3.48}$$

where

$$\begin{aligned}\chi_a &= 2N_c \int \frac{d^3\mathbf{p}}{(2\pi)^3} \left(\frac{M_a}{E_a}\right)^2 \frac{\mathbf{k}\cdot\nabla_{\mathbf{p}}(f_a^0+\bar{f}_a^0)}{\omega + i\tau_a^{-1} - \mathbf{k}\cdot\mathbf{v}} \\ &= \frac{N_c M_a^2}{\pi^2 T} \int dE_a v \left[f_a^0(f_a^0-1) + \bar{f}_a^0(\bar{f}_a^0-1)\right] \left(\frac{\tau_a^{-1}-i\omega}{kv} \arctan\frac{kv}{\tau_a^{-1}-i\omega} - 1\right),\end{aligned} \tag{3.49}$$

and

$$\xi_a = \frac{N_c}{\pi^2} \int dE_a \frac{p^3}{E_a^2}(f_a^0 + \bar{f}_a^0 - 1). \tag{3.50}$$

Comparing Eqs.(3.49) and (3.50) with the $\chi_{\sigma\sigma}$ in Eq. (B.14), we find they agree if $\tau^{-1} = 0$. We note that Eq.(3.28) for the the quark correlator in the quantum treatment reduces to Eq.(3.49) in the limit $\hbar = 0$. Since $\delta\langle\bar{q}q\rangle$ and $\delta\langle\bar{s}s\rangle$ can be of any value, Eq. (3.48) is satisfied if and only if:

$$\begin{vmatrix} 1-2(G_S+K\langle\bar{s}s\rangle)(\chi_q-\xi_q) & -2K\langle\bar{q}q\rangle(\chi_q-\xi_q) \\ -4K\langle\bar{q}q\rangle(\chi_s-\xi_s) & 1-2G_S(\chi_s-\xi_s) \end{vmatrix} = 0. \tag{3.51}$$

By solving Eq.(3.51), we can obtain the relation between the frequency and wave number of collective modes in quark matter, i.e., its dispersion relation $\omega(k)$. These collective modes become unstable and grow with time if their frequencies are imaginary, i.e., $\omega = i\Gamma_k$, which can occur in quark matter for some temperatures and densities as discussed in Section 2. Since $\chi(\omega,k) = \chi(\omega/k)$ when $\tau^{-1} = 0$, the growth rate Γ_k is thus proportional to k in the absence of collisions. This is in contrast to the results obtained in the quantum linear response theory, where the growth rates of unstable modes of larger wave numbers are suppressed.

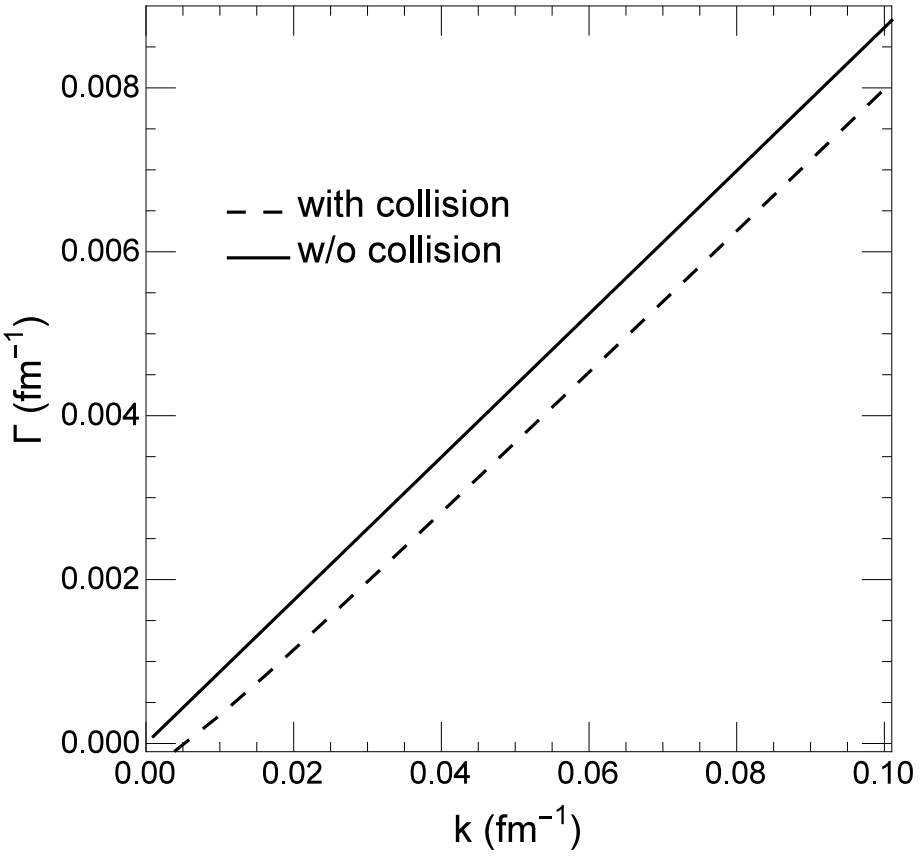

Figure 3.4: Growth rates of unstable modes in a quark matter of net quark density 0.7 fm^{-3} and temperature 45 MeV without and with the collisional term using a light quark scattering cross section that has a value of 3 mb and is isotropic. Taken from Ref. [1]

3.2.2 Results

In Fig. 3.4, we show by dashed and solid lines the dispersion relation or growth rate of unstable modes in a quark matter of net quark density 0.7 fm^{-3} and temperature 45 MeV with and without the collisional effect, respectively, using an isotropic light quark scattering cross section of 3 mb. The collisional effect is seen to reduce Γ_k by almost a constant value for all wave numbers k. Although the reduction is small, its effect is important for soft unstable modes. In this particular example, unstable

modes with $k < 0.005$ fm^{-1} disappear after the inclusion of collisional effects. As a result, the spinodal instability regions for unstable modes of longer wavelength become smaller than those of shorter wavelength as shown in Fig. 3.5 by dotted, dashed, and dash-dotted lines for the spinodal boundaries of unstable modes of different wave numbers of 0.001, 0.01, and 0.1 fm^{-1}, respectively. Compared to the entire spinodal instability region shown by the solid curve, the area of the spinodal region in the temperature and density plane shrinks as the wave number of the unstable mode k decreases. This behavior is opposite to that shown in Section 3.1, where the high k modes disappear due to quantum effects, and the spinodal region shrinks as k increases. Such a behavior is also observed in Ref. [55] based on the linearized hydrodynamical approach with a finite viscosity, where it is found that the spinodal region shrinks and the growth rates of unstable modes decrease in the presence of viscosity. However, while the growth rate vanishes at $k = 0$ in Ref. [55], it is negative in our study based on the linearized Boltzmann equation. The latter is due to the factor $\omega + i\tau^{-1}$ that always appears together in the relaxation-time approximation. In this case, the growth rate is given by $-\tau^{-1}$ in the long wavelength limit and vanishes only in the limit of infinite scattering cross section.

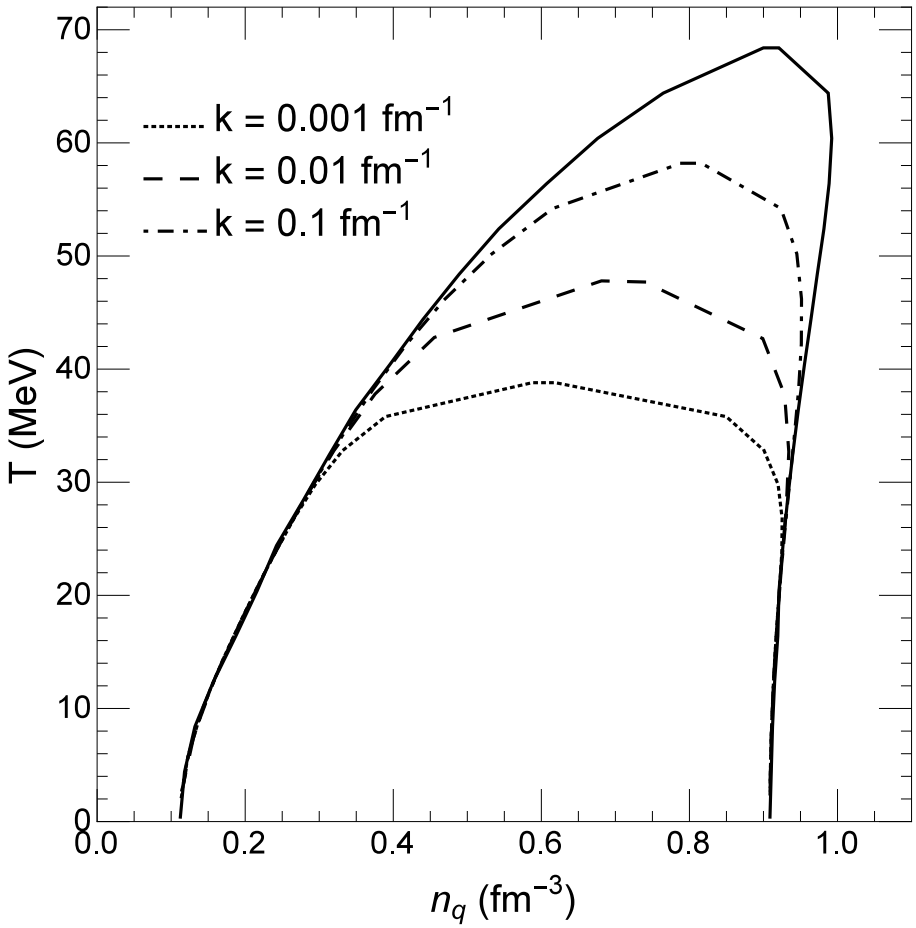

Figure 3.5: The spinodal region calculated with the inclusion of the collisional term using an isotropic quark scattering cross section of 3 mb for the different wave numbers of unstable modes. The solid line denotes the boundary of the entire spinodal instability region.

4. QUARK MATTER IN A BOX

This section serves as a bridge between the studies of the spinodal instabilities in the small and large amplitude limits. Although the small amplitude case has already been discussed in Section 3, we will develop an intuitive picture to show how an initial sinusoidal fluctuation grows during the early stage of its time evolution by solving the Boltzmann equation numerically. The latter is done by using the test particle method, in which the time evolution of the one-particle phase-space distribution function $f(\mathbf{x}, \mathbf{p}, t)$ is described by the motions of many classical particles as discussed in detail in Appendices C and D. For the large amplitude case, which also includes the growth of instabilities during the late stage, we will follow the whole phase separation process to see how dense clusters develop inside a box of initially uniform quark matter and finally lead to the formation of a large scale structure. Some observables will be studied to characterize this structure.

4.1 Small amplitude density fluctuations

We consider a quark matter that is confined in a cubic box with periodic boundary conditions. The system is prepared by uniformly distributing many test particles inside the box according to the density of the system with their momenta given by the Fermi-Dirac distribution at certain temperature. We then study the growth of density fluctuations from an initial distribution with density and temperature corresponding to that inside the spinodal region. Results obtained from solving the Boltzmann equation by following the classical motions of these test particles will then be compared with those obtained from the linear response theory. Specifically, we introduce an initial density fluctuation that has a sinusoidal oscillation in the z direction, $\rho_{\rm ini} = \rho_0(1+0.1\sin(2\pi z/L))$, where ρ_0 is the average initial density and L is

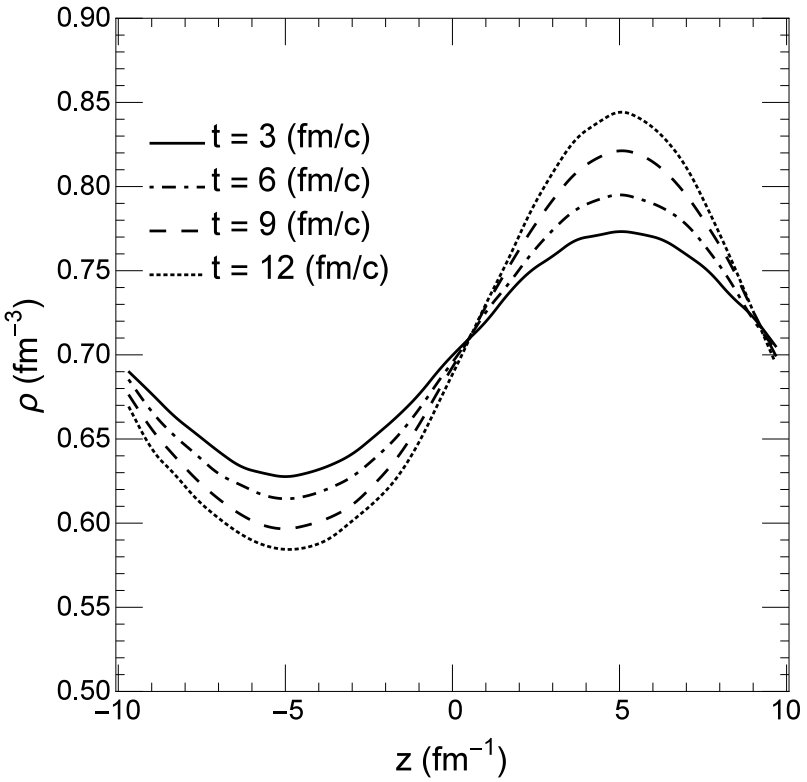

Figure 4.1: Time evolution of a unstable density mode of wave number $k = 0.31$ fm^{-1}.

the length of the box with $L = 10,\ 20,\ 30,\ 40,\ 50$ fm corresponding to wave numbers $k = 0.63,\ 0.31,\ 0.21,\ 0.16,\ 0.13$ fm^{-1}, respectively. As an example, Fig. 4.1 shows how the amplitude of the sinusoidal wave grows with time in the case of $L = 20$ fm, the average density $\rho_0 = 0.7$ fm^{-3}, and an initial temperature $T = 45$ MeV. Since the amplitude of density fluctuation at early times is expected to grow exponentially, it can be approximated by a hyperbolic cosine function of time, i.e.,

$$\delta\rho(t) = \delta\rho_0 \cosh(\Gamma_k t), \tag{4.1}$$

where Γ_k is the growth rate and can be extracted directly from the numerical results, and they are shown in Fig. 4.2 by solid circles. They are seen to agree very well with those obtained from the analytical results based on the linearized Boltzmann equation (see Appendix D.1), shown by solid and dashed curves for the cases with and without the collision term in the Boltzmann equation, respectively, in the small k region, although they differ slightly at $k = 0.63$ fm^{-1} but still within the numerical error bar.

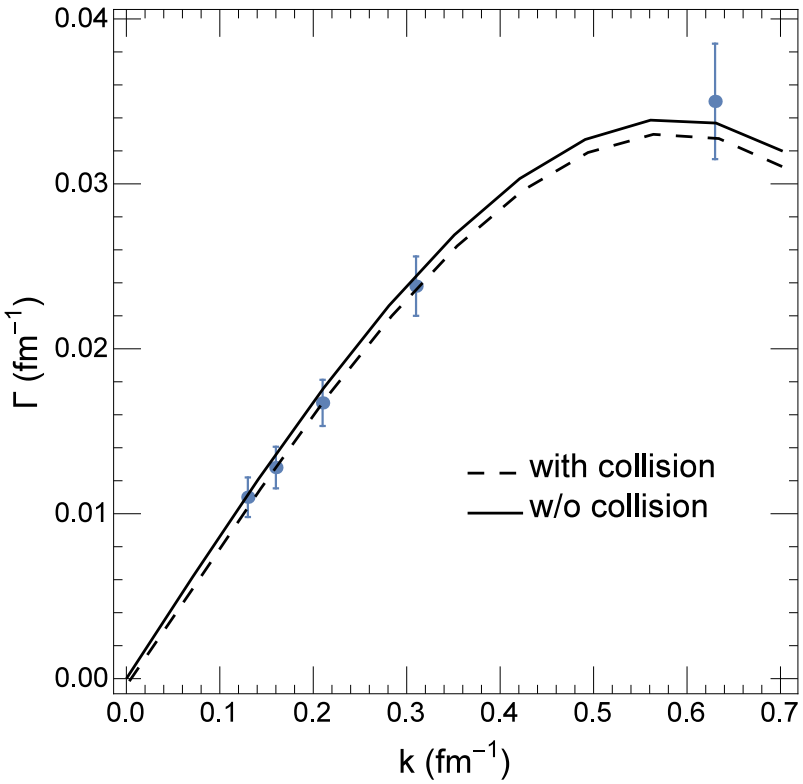

Figure 4.2: Growth rates extracted from numerically solving the Boltzmann equation for unstable modes of wave numbers $k = 0.63$, 0.31, 0.21, 0.16, 0.13 fm^{-1} for quark matter of density $\rho = 0.7$ fm^{-3} and temperature $T = 45$ MeV. Analytical results from the linearized Boltzmann equation are shown by solid and dashed curves for the cases with and without the collision term, respectively.

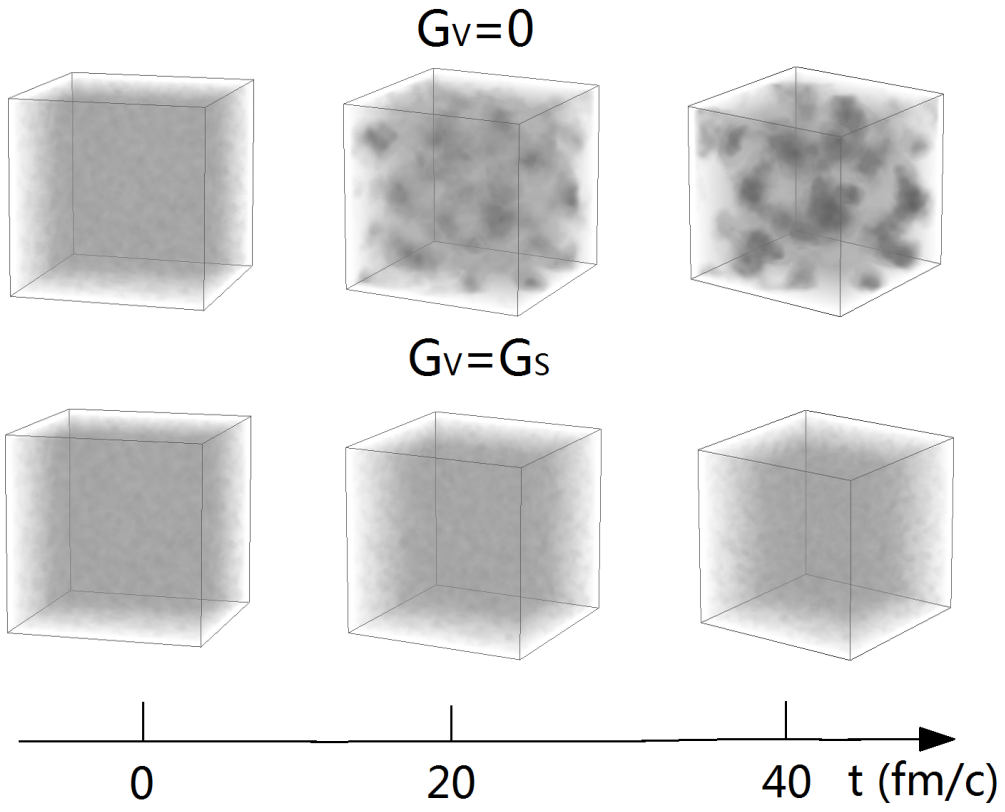

Figure 4.3: Time evolution of density distribution in a quark matter of initial net quark density $n = 0.5$ fm^{-3} and temperature $T = 20$ MeV for the cases of $G_V = 0$ (upper row) and $G_V = G_S$ (lower row).

To study how density fluctuations emerge and grow, we compare results from two calculations based on the same initial conditions but with and without the spinodal instability in the equation of state. This is achieved by introducing a vector interaction in the NJL model, which is known to move a quark matter from inside the spinodal region to the outside if its strength is sufficiently large. As shown in Section 3, the spinodal region disappears if the vector coupling G_V has the same value as G_S

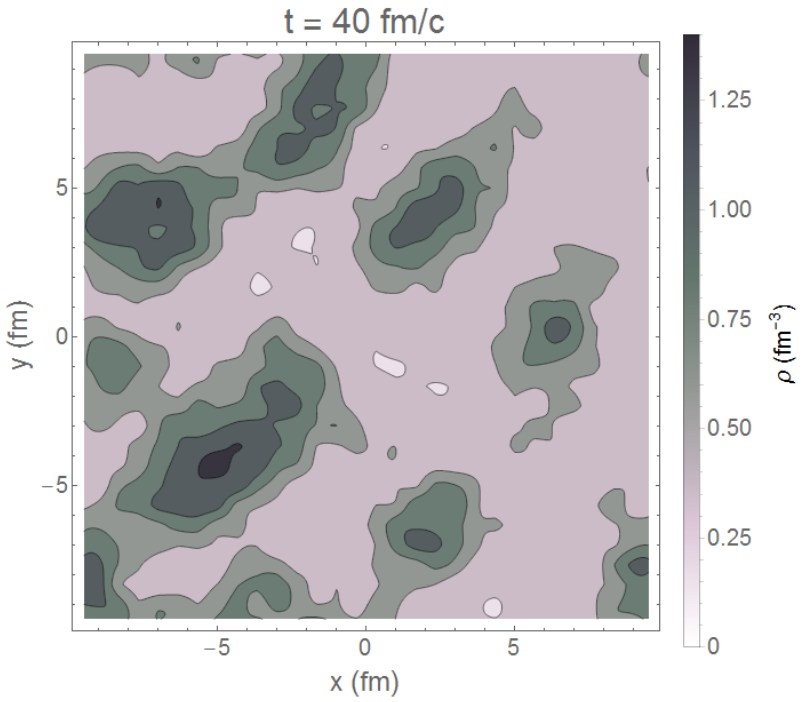

Figure 4.4: Cross sectional view of density distribution on the $z = 0$ plane at $t = 40$ fm/c for the case $G_V = 0$ with a first-order phase transition.

for initial temperature $T_0 = 20$ MeV and net quark density $\rho_0 = 0.5$ fm^{-3}, although the latter is well inside the spinodal instability region for $G_V = 0$. Figure 4.3 shows the time evolution of the density distribution in a box of size $20 \times 20 \times 20$ fm^3 for the two cases of $G_V = 0$ (upper row) and $G_V = G_S$ (lower row), with the darker color denoting higher density regions and the lighter color denoting lower density regions. Although the system is initially uniform in space, some dense spots are present due to statistical fluctuations because of finite number of test particles used in the calculation. In the case of $G_V = G_S$ without a first-order phase transition or spinodal instability, the density distribution in the box remains unchanged with time as shown in the lower row. This changes dramatically, however, for the case of $G_V = 0$. Due to the spinodal instability, the initial dense spots act like "seeds",

which create several small low pressure centers and attract nearby partons, leading to the formation of many clusters at $t = 20$ fm/c. These clusters further grow, connect with each other, and form stable large structures at $t = 40$ fm/c, when the system clearly separates into two phases of matter with one of high density and the other of low density. A clearer picture can be obtained by taking a cross sectional view

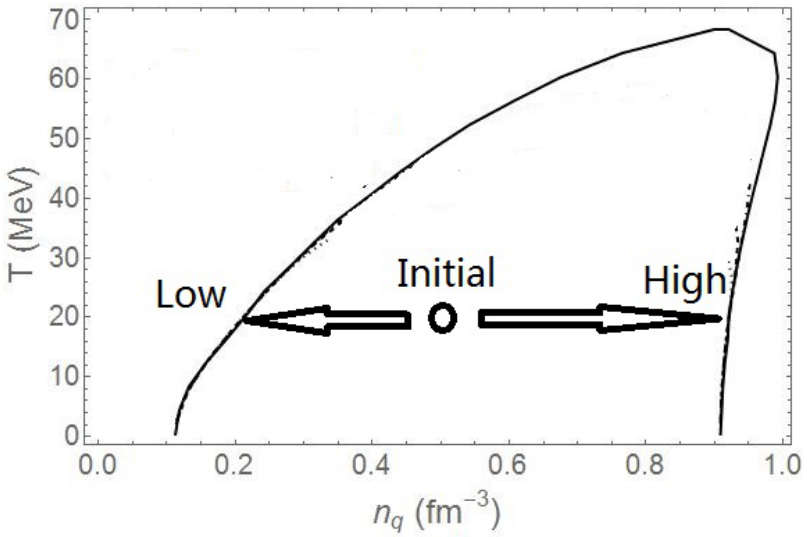

Figure 4.5: Demonstration of the phase separation on the phase diagram.

on the $z = 0$ plane as shown by the density distribution contours in Fig. 4.4. The two phases are now distinguishable with the dilute phase having a density of about 0.25 fm^{-3} and the dense phase having a density of about 1.0 fm^{-3}. According to the phase diagram in Fig. 4.5, the initial location of the system is indicated by the circle inside the spinodal region. During the phase separation, the location of most part of the system moves towards the left boundary of the spinodal instability region that has a density of about 0.2 fm^{-3}, while that of the small part of the system moves towards the right boundary of the spinodal instability region that has a density of

about 0.9 fm^{-3}, consistent with the picture shown by the density evolution. As

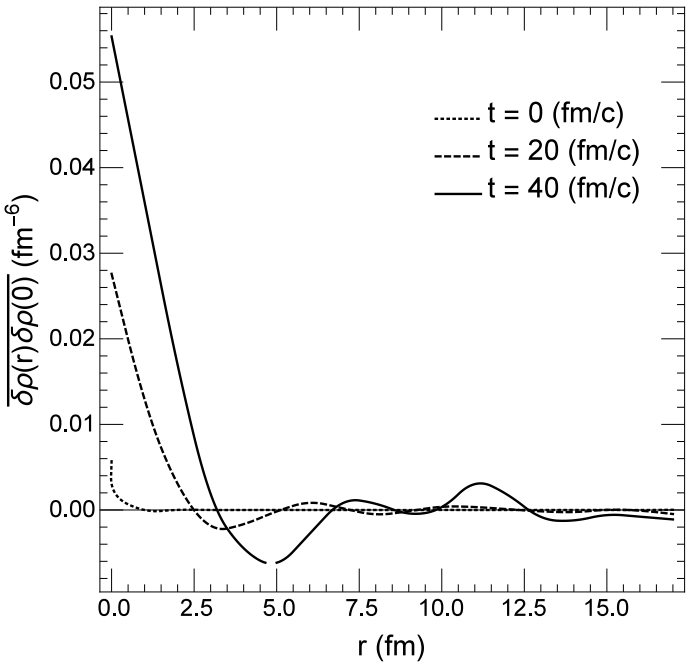

Figure 4.6: Time evolution of the density-density correlation function in a quark matter of temperature $T = 20$ MeV and average net quark density $n = 0.5$ fm^{-3} inside the spinodal region.

the large scale structure forms, we expect the density-density correlation $\overline{\rho(r)\rho(0)}$ to get stronger and the correlation length to become larger. This is indeed the case as shown in Fig. 4.6, where it is seen that both the amplitude of the correlation function and the correlation length increases with time.

The density fluctuations can be quantified by the scaled density moments $\langle\rho^N\rangle/\langle\rho\rangle^N$ [56], where

$$\rho^N \equiv \frac{\int d^3\mathbf{r}\rho(\mathbf{r})^{N+1}}{\int d^3\mathbf{r}\rho(\mathbf{r})}. \tag{4.2}$$

This quantity is scale invariant since its value remains unchanged under a scale

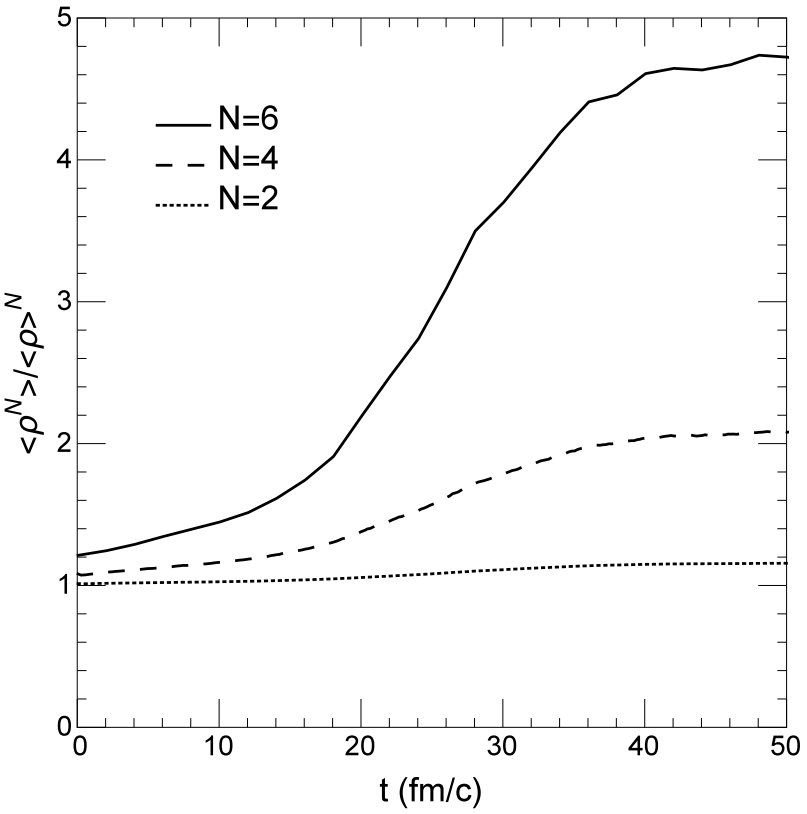

Figure 4.7: Time evolution of scaled density moments in a quark matter of temperature $T = 20$ MeV and average net quark density $n = 0.5$ fm^{-3} inside the spinodal region.

transfomation $\mathbf{r} \to \lambda\mathbf{r}$, where λ can be any positive number. The scaled density moments are all equal to one for a uniform density distribution but become greater than one as density fluctuations grow. In Fig. 4.7, we show by dotted, dashed, and solid lines the scaled density moments for $N = 2$, 4 and 6, respectively. Our results show that the scaled moments increase during the phase separation and saturate at about $t = 40$ fm/c, when the phase separation almost ends. Also, moments with larger N increase faster and saturate at larger values. The final saturation values can be estimated as follows. For a system of an initial density ρ_0 that separates into two phases of density ρ_1 and ρ_2 with volumes V_1 and V_2, respectively, the scaled

density moments are then

$$\frac{\langle \rho^N \rangle}{\langle \rho \rangle^N} = \frac{\rho_1^{N+1} V_1 + \rho_2^{N+1} V_2}{\left(\rho_1^2 V_1 + \rho_2^2 V_2\right)^N / \left(\rho_1 V_1 + \rho_2 V_2\right)^{N-1}}. \tag{4.3}$$

Using the condition of particle number conservation

$$\rho_1 V_1 + \rho_2 V_2 = \rho_0 (V_1 + V_2), \tag{4.4}$$

the scaled density moments after the phase separation is thus

$$\frac{\langle \rho^N \rangle}{\langle \rho \rangle^N} = \frac{[\rho_1^{N+1}(\rho_2 - \rho_0) + \rho_2^{N+1}(\rho_0 - \rho_1)][\rho_0(\rho_2 - \rho_1)]^{N-1}}{[\rho_1^2(\rho_2 - \rho_0) + \rho_2^2(\rho_0 - \rho_1)]^N}. \tag{4.5}$$

For our case of $\rho_0 = 0.5$ fm^{-3}, $\rho_1 \approx 0.25$ fm^{-3}, and $\rho_2 \approx 1.0$ fm^{-3}, we have $\langle \rho^2 \rangle / \langle \rho \rangle^2 \to 1.22$,$\langle \rho^4 \rangle / \langle \rho \rangle^4 \to 2.11$, and $\langle \rho^6 \rangle / \langle \rho \rangle^6 \to 3.75$, which are close to the final saturation values shown in Fig. 4.7.

Other quantities of interest are the skewness and kurtosis of the particle multiplicity distribution, which were proposed as possible signals for the critical phenomena [23] and have been studied in the beam energy scan experiments at RHIC[26, 27]. They are defined as follows:

$$\begin{aligned} \text{skewness} &\equiv \frac{\langle \delta N_q^3 \rangle}{\langle \delta N_q^2 \rangle^{3/2}}, \\ \text{kurtosis} &\equiv \frac{\langle \delta N_q^4 \rangle}{\langle \delta N_q^2 \rangle^2} - 3. \end{aligned} \tag{4.6}$$

Both quantities characterize how far an event-by-event multiplicity distribution deviates from a normal distribution. A positive skewness means a long tail on the right side of the distribution, i.e., most events have the net quark number below the

mean value, while some events have an extreme high net quark number. A positive kurtosis implies a sharper peak than the peak in a normal distribution, while a negative kurtosis corresponds to a flatter one. Theoretical calculations based on the grand canonical picture predict that both quantities diverge with the correlation length when a system approaches its critical point [23], with the kurtosis diverging faster than the skewness. Therefore, they can be viewed as signals for the critical end point.

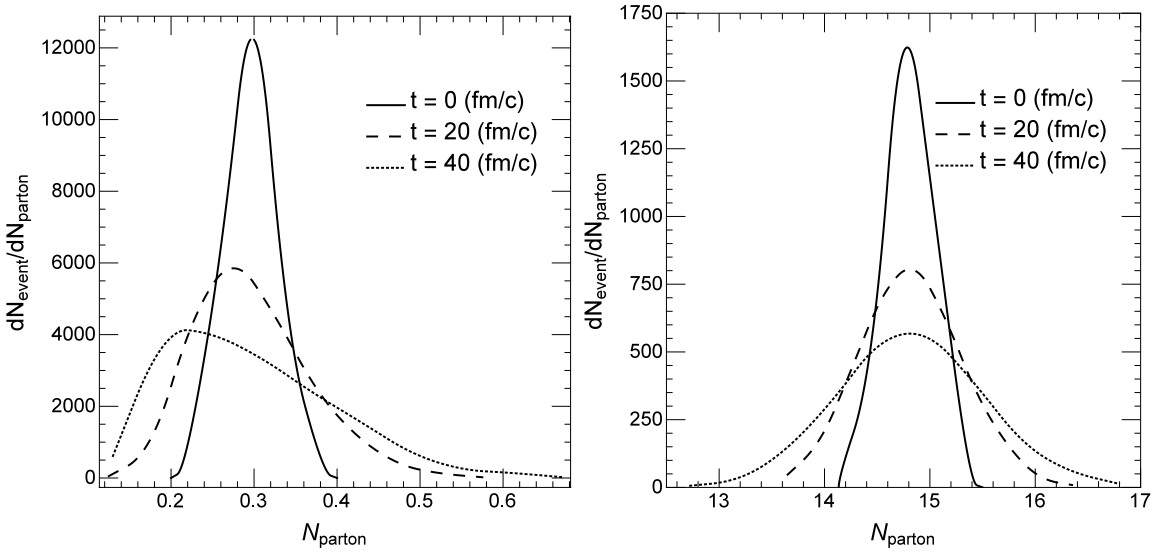

Figure 4.8: Time evolution of event-by-event distribution of the number of quarks in a sub-volume of size 0.6 fm^3 (left window) and 30 fm^3 (right window) in a quark matter of temperature $T = 20$ MeV and average net quark density $n = 0.5$ fm^{-3} inside the spinodal region. The total number of events is 1000.

To be consistent with the grand canonical picture, we consider quarks in a sub-volume of the box in our study, such as its central cell, and treat the remaining part as the reservoir. When the system is initially inside the spinodal instability region, the sub-volume can take quarks from the reservoir in some cases, and in most cases

quarks are taken away from it. So the quark number inside this sub-volume varies dramatically from event to event and thus generates the skewness and kurtosis. In Figs. 4.8, we show the event-by-event distribution of the number of quarks in the central cell from 1000 events at t = 0, 20, and 40 fm/c by the solid, dashed and dotted lines, respectively, for the two cases of sub-volume of size 0.6 fm^3 (the left window) and 30 fm^3 (the right window). The left window of Fig. 4.8 clearly shows that the distribution for the small sub-volume becomes asymmetric as time increases, starting with an initial skewness of 0.11 and increasing to 0.60 at 20 fm/c and 0.75 at 40 fm/c. This feature is absent in the right window of Fig. 4.8 for the larger sub-volume, where the distribution remains essentially symmetric with increasing time, with the skewness changing slowly from -0.001 (t=0) to 0.086 (t=20 fm/c) and 0.132 (t=40 fm/c), and there is no apparent increase or decrease in the kurtosis.

In summary, we have analyzed the phase separation of a quark matter in a box. The growth rates of unstable modes extracted from numerically solving the Boltzmann equations are compared and found to agree with the analytical results in Section 3. The high-order density moments in the system are seen to increase and saturate at large values after the phase separation and can be considered as signals for a first-order phase transition. The skewness of the quark number event-by-event distribution in a small sub-volume of the system also increases, but this feature becomes absent if the subsystem is large. In both cases, there is no appreciable kurtosis in the distribution.

5. EXPANDING QUARK MATTER

5.1 Blast wave initial conditions

To study how large density fluctuations due to the spinodal instability as a result of a first-order phase transition obtained from the box calculation in Section 4 are affected by the expansion of the system as in a heavy ion collision, we carry out a dynamical calculation using the transport model that includes parton scatterings besides the mean-field potentials (see Appendix C and D for details). For the initial parton distributions, their positions are taken to follow that of a spherical Wood-Saxon form:

$$\rho(r) = \frac{\rho_0}{1 + \exp((r - R)/a)} \tag{5.1}$$

with a radius $R = 5$ fm and a surface thickness parameter $a = 0.5$ fm, similar to that expected from a central Au+Au collisions. Momenta of the patons are again taken to be that of a Fermi-Dirac distribution at certain temperature. Calculations are then carried out with two different equations of state with and without a first-order phase transition, which can be realized by adjusting the coupling strength of the vector interaction. To see how the expanding system goes into the spinodal region in the QCD phase diagram, we first study the time evolution of the temperature and density in the central cell of the system, which has an initial density $\rho_0 = 1.5$ fm^3 and temperature $T = 70$ MeV, and trace its trajectory as shown in Fig. 5.1 for the two cases with (solid line) and without (dashed line) a phase transition. Although a system described by the transport model may not always be in perfect thermal equilibrium, we approximate its temperature by that of an equilibrated quark matter that has the same energy density and net quark density in the NJL model. As

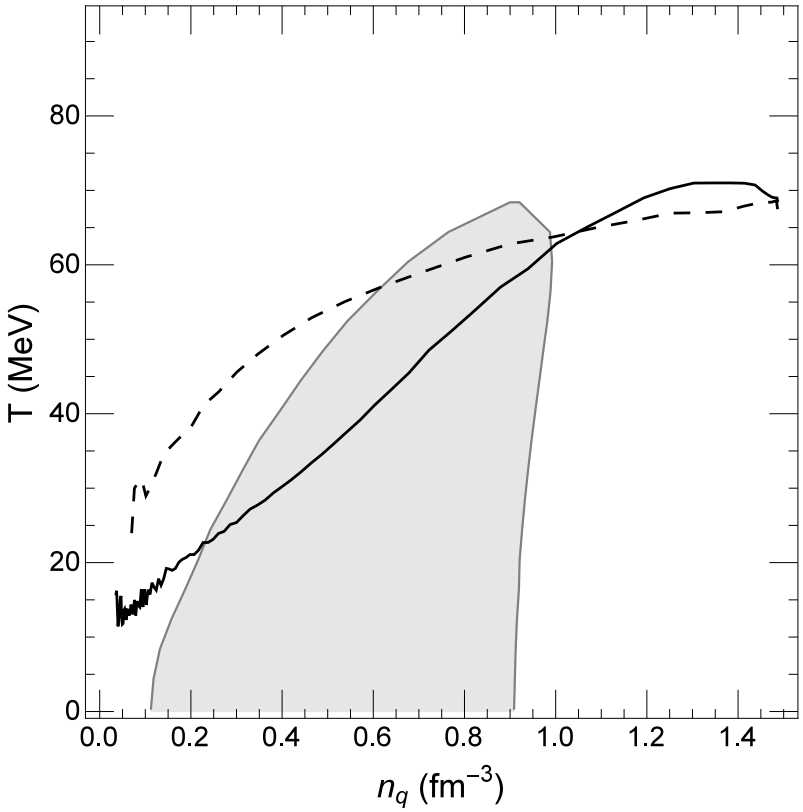

Figure 5.1: Phase trajectories of the central cell of an expanding quark matter with (solid line) and without (dashed line) a first-order phase transition using the blast wave initial conditions. The spinodal region is shown by gray color.

expected, the solid curve enters the spinodal instability region, which is shown by the gray color, at about 6.5 fm/c and leaves the region at about 17.4 fm/c after spending about 10 fm/c inside this region. How the central density decreases with time is shown by the solid line in Fig. 5.2, which is seen to decrease slower than in the case without a first-order phase transition shown by the dashed line obtained with $G_V = G_S$

The density fluctuations can be seen via the density distribution on a plane such as the one at $z = 0$ shown in Fig. 5.3. The left window shows the density distribution

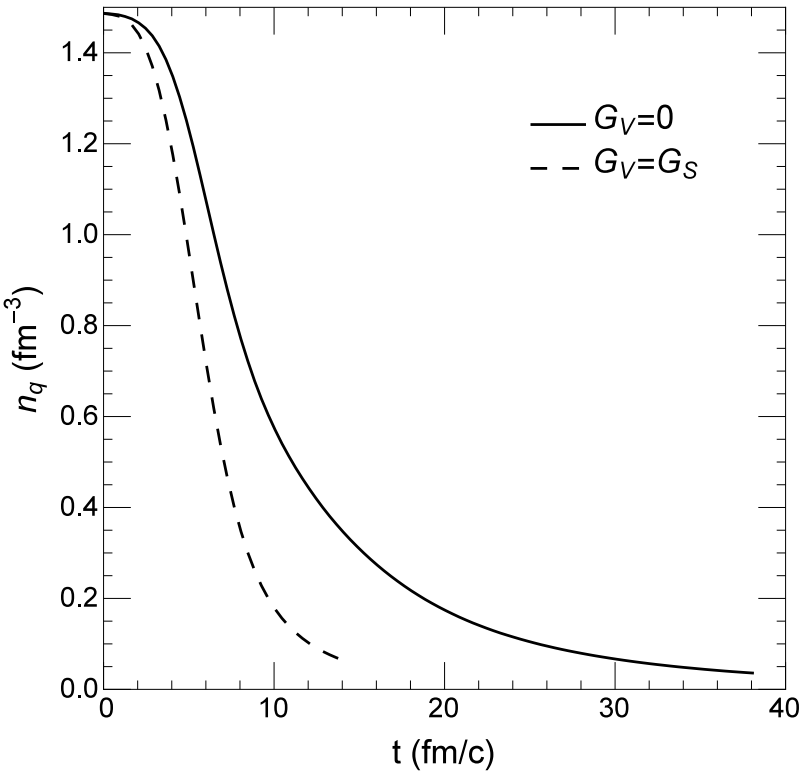

Figure 5.2: Time evolution of the density of the central part of an expanding quark matter with (solid line) and without (dashed line) a first-order phase transition.

at $t = 20$ fm/c for the case with a first-order phase transition, while the right window shows that at $t = 10$ fm/c for the case without a first-order phase transition, when the density of the central cell is about 0.2 fm^{-3} in both cases. Although density clumps appear in both cases, those in the one with a first-order phase transition are significantly larger. As in the case of a quark matter in a box, we can quantify the density fluctuations by studying the scaled density moments [55]. They are shown in Fig. 5.4 by the black and red lines for the cases with and without a first-order phase transition, respectively. The dotted, dashed, and solid lines are for $N = 2$, 4, and 6 respectively. In both cases, the scaled density moments first increase and then decrease with time. In the case without a first-order phase transition, this is

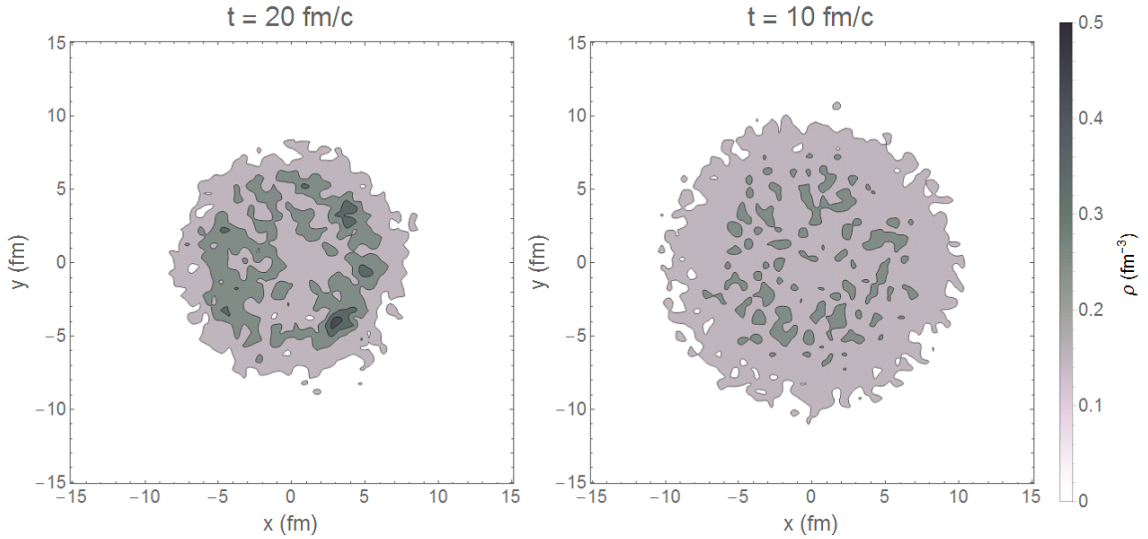

Figure 5.3: Density distributions of an expanding quark matter on the $z = 0$ plane at $t = 20$ fm/c for the case with a first-order phase transition (left window) and at $t = 10$ fm/c for the case without a first-order phase transition (right window).

caused by an increased surface and deviation from the smooth Wood-Saxon density distribution that disappear quickly in time from their initial values. To the contrary, the scaled density moments in the case with a first-order phase transition becomes much larger with time and only decreases very little afterwards, reflecting the effect due to density clumps that distribute randomly inside the expanding quark matter. Therefore, the saturated scaled density moments, which are larger for larger N, can be regarded as signals for a first-order phase transition in a baryon-rich quark matter.

Since density fluctuations can lead to spatial anisotropy even in central heavy ion collisions, it has been suggested that they may affects the anisotropic flows in the transverse plane [38, 39]. The latter are defined by expanding the transverse

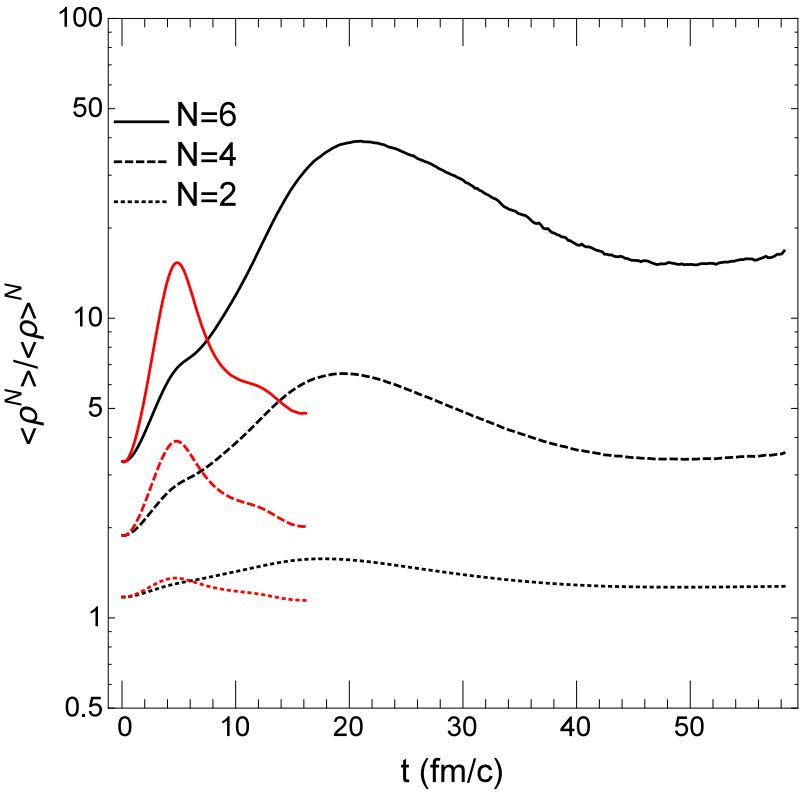

Figure 5.4: Scaled density moments as functions of time for the cases with (black lines) and without (red lines) a first-order phase transition.

momentum distribution $f(p_T, \phi)$ as a Fourier series in the azimuthal angle ϕ,

$$f(p_T, \phi) = \frac{N(p_T)}{2\pi}\{1 + 2\sum_{n=1}^{\infty} v_n(p_T)\cos[n(\phi - \psi_n)]\} \tag{5.2}$$

in terms of the event plane angle ψ_n [64] and the anisotropic flow coefficient v_n. To calculate the anisotropic flow coefficients, we use the two particle cumulant method [65, 66], namely, $v_n\{2\} = \sqrt{\langle\cos(n\Delta\phi)\rangle}$ by averaging over all particle pairs in an event. We have calculated $v_2\{2\}$ and $v_4\{2\}$ for 100 events, and their final event distributions are shown, respectively, in the left and right windows of Fig. 5.5 with the solid and dashed lines for the cases with and without first order phase transition,

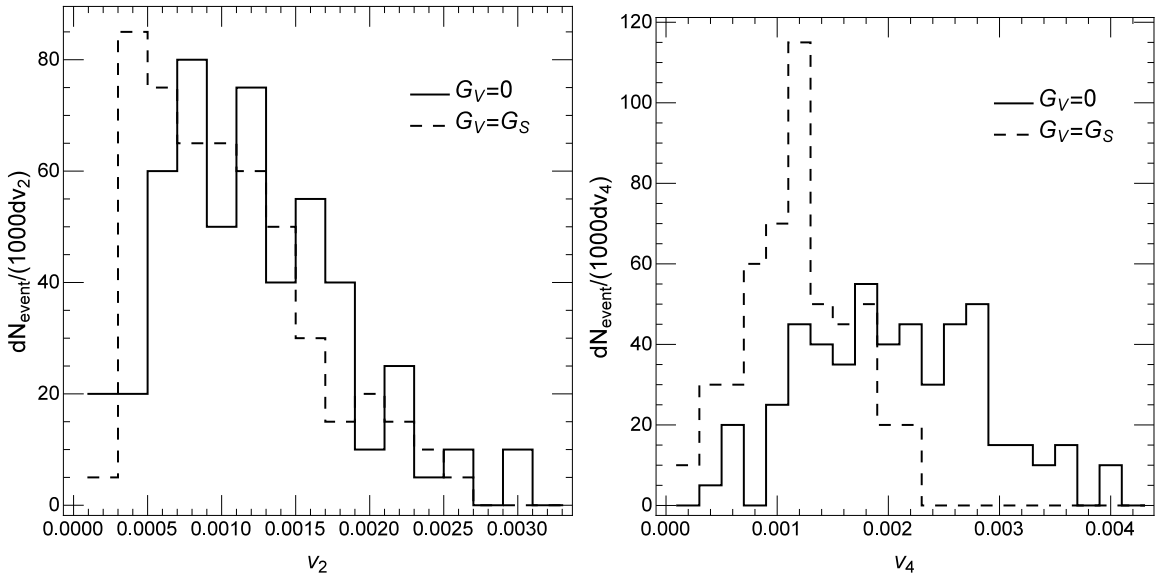

Figure 5.5: Final anisotropic flow coefficients v_2 (left window) and v_4 (right window) distributions for 100 events.

respectively. Both distributions peak at a larger value for the case with a first-order phase transition, particularly for v_4, thus providing a plausible signal for the first-oder phase transition. Unfortunately, the values of the fluctuation induced v_2 and v_4 are much smaller than those in non-central heavy ion collisions.

We have also studied the effect of density fluctuations on dilepton production. Since the dilepton production rate is proportional to the square of parton density, more dileptons are produced when the density fluctuation is large. Also, a longer partonic phase as a result of a first-order phase transition would increase the depletion yield as well. As usually done in studying depletion production in heavy ion collisions, we use the perturbative approach to calculate the dilepton yield from the quark-antiquark scattering in the expanding quark matter by neglecting its effect on the

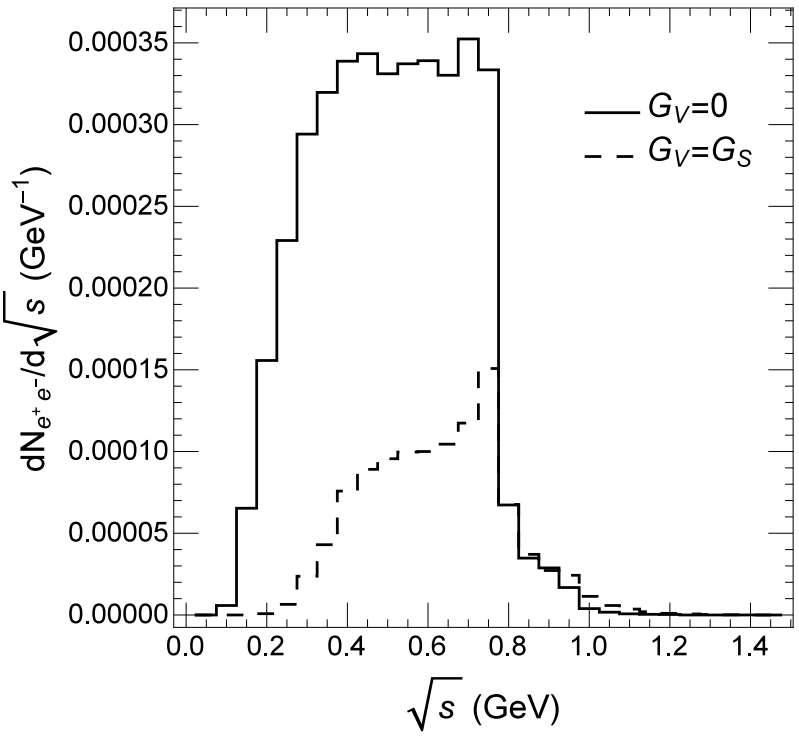

Figure 5.6: Dilepton yield as a function of the invariant mass $\sqrt{s}$ for the cases with (solid line) and without (dashed line) a first-order phase transition.

collisional dynamics. Their cross sections are given by

$$\sigma_{q\bar{q}\to e^+e^-} = \frac{4\pi\alpha^2}{3s}\sqrt{\frac{1-4m_e^2/s}{1-4m_q^2/s}}\Big(1+2\frac{m_e^2+m_q^2}{s}+4\frac{m_e^2m_q^2}{s^2}\Big), \tag{5.3}$$

where $s = (p_{e^-} + p_{e^+})^2$ is the square of the invariant mass of the dilepton and $\alpha = \frac{1}{137}$ is the fine-structure constant. The dilepton invariant mass spectrum from the expanding quark matter are shown in Fig. 5.6 by the solid and dashed lines for the cases with and without first-order phase transition, respectively. As expected, more dileptions are produced from the quark matter with a first-order phase transition. We note the dilepton invariant mass spectrum peaks at $\sqrt{s} \approx 0.5$ GeV with the peak

value being about 3.5×10^{-4} GeV^{-1}, which is comparable with the result obtained from a hadronic transport model [67]. This enhancement in dilepton production may thus be detectable in experimetns. We also note that most dileptons are produced from quark-antiquark annihilation as very few pions are present in the system due to the low phase transition temperature T_c predicted by the SU(3) NJL model.

In summary, we have studied in this subsection the spinodal instability of an expanding quark matter that are initially smoothly distributed in a sphere with a diffused surface. We have found that its expansion is slowed by the presence of a first-order phase transition and it develops at same time density clumps and momentum anisotropy. These features are studied via the scaled density moments and anisotropic flows $v_2\{2\}$ and $v_4\{2\}$ as possible signals of the phase transition. Also, an enhanced production of dileptons is predicted as a result of the density fluctuations.

5.2 Realistic initial conditions from the AMPT

In this subsection, we use a more realistic initial parton distributions for heavy ion collisions. Specifically, the initial partons are obtained from a multiphase transport (AMPT) model with string melting [30] that uses a heavy ion jet interaction generator (HIJING) [68, 69, 70] as the input. In this model, not only the mini-jet partons from initial hard collisions are included but also hadrons produced from excited strings, which are neither projectile nor target nucleons without any interactions, are converted to partons according to the flavor and spin structures of their valence quarks. In particular, a meson is converted to a quark and an anti-quark, while a baryon is first converted to a quark and a diquark, and the diquark is then decomposed into two quarks. The quark masses are taken to be $m_u = 5.6$, $m_d = 9.9$, and $m_s = 199$ MeV$/c^2$ as in the PYTHIA program [71]. The above two-body decom-

position is isotropic in the rest frame of the parent hadron or diquark. These partons are produced after a formation time of $t_f = E_H/m_{T,H}^2$, with E_H and $m_{T,H}$ denoting, respectively, the energy and transverse mass of the parent hadron. We obtain these partons as the initial conditions of out study of an expanding quark matter by running the AMPT program with vanishing parton scattering cross sections in Zhang's parton cascade (ZPC)[72] and with the hadronic afterburner based on a relativistic transport (ART) [73, 74] turned off. Using the partons from Au+Au collisions at zero impact parameter and a center-of-mass collisional energy $\sqrt{s_{NN}} = 2.5$ GeV as the initial distribution, we have found that some parts of the system go through the spinodal region when the SU(3) NJL model with $G_V = 0$ is used in the Boltzmann equation and in constructing the phase diagram. As shown by the solid line in Fig. 5.7, the trajectory of the central part of the system moves into the spinodal instability region at about 4.4 fm/c after expansion, and goes out of this region at about 5 fm/c. Although 0.6 fm/c is too short for the spinodal instability to develop in the central part of the quark matter, its other parts may stay longer in the spinodal instability region due to both the geometry of initial parton distributions and the correlations between the parton rapidities and longitudinal (z) coordinates.

Figure 5.8 shows the rapidity and longitudinal coordinate correlation of initial partons from a typical AMPT event for central Au+Au collisions at $\sqrt{s_{NN}} =$ 2.5 GeV. This correlation can be quantified as follows:

$$r_{yz} \equiv \frac{\sum_i (y_i - \bar{y})(z_i - \bar{z})}{\sqrt{\sum_i (y_i - \bar{y})^2 \sum_i (z_i - \bar{z})^2}} = 0.355. \tag{5.4}$$

This positive correlation means that partons initially in the front are more likely to have momenta pointing forward, while partons initially in the back are more likely to have momenta pointing backward. This correlation helps the initially disc-shaped

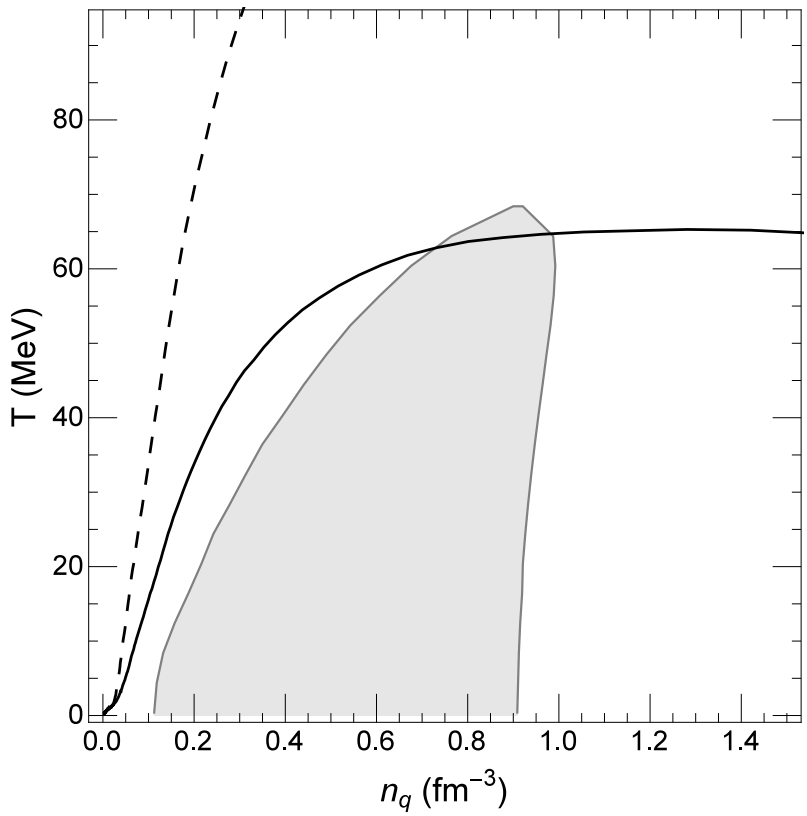

Figure 5.7: Phase trajectories of the central part of an expanding quark matter with (solid trajectory) and without (dashed trajectory) a first-order phase transition using initial parton distribution from the AMPT model. The spinodal region is shown by gray color.

quark matter to expand, leading to a fast decrease of the density in the center of the quark matter, as shown in the upper row of Fig. 5.9. Here, the quark matter is initially largely confined in a thin disk of thickness less than 0.5 fm. When it is allowed to free streaming without any interactions, there appear two high density clumps that fly apart in the opposite directions. This feature becomes less prominent after the inclusion of quark mean-field potentials but without a phase transition in the quark matter, i.e., taking $G_V = G_S$, as shown in the middle row of Fig. 5.9. With a first-order phase transition in the quark matter by setting $G_V = 0$, the

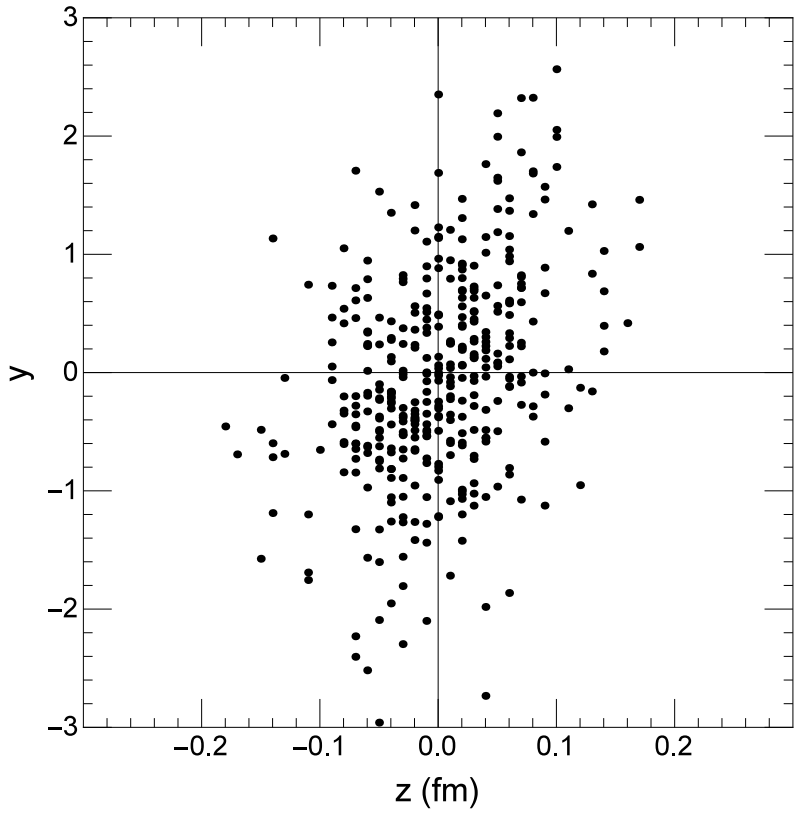

Figure 5.8: Rapidity and longitudinal coordinate correlations of initial partons from AMPT for central Au+Au collisions at $\sqrt{s_{NN}} = 2.5$ GeV.

lower row of Fig. 5.9 shows that the initial central disk evolves into three disks of dense matter with one in the middle due to the strong attractions that keep some partons to coalesce, besides the two forward and backward moving disks. As the quark matter expands, these disks become rings and finally turn into disjointed clumps. Furthermore, the density distribution of the quark matter in the reaction plane ($y = 0$) shown in Fig. 5.10 indicates that the quark matter with a first-order phase transition expands twice as slow as that without a first-order phase transition. Because of the non-trivial spatial distribution even in the case of free-streaming quark matter, the scaled density moments are no longer useful quantities to characterize

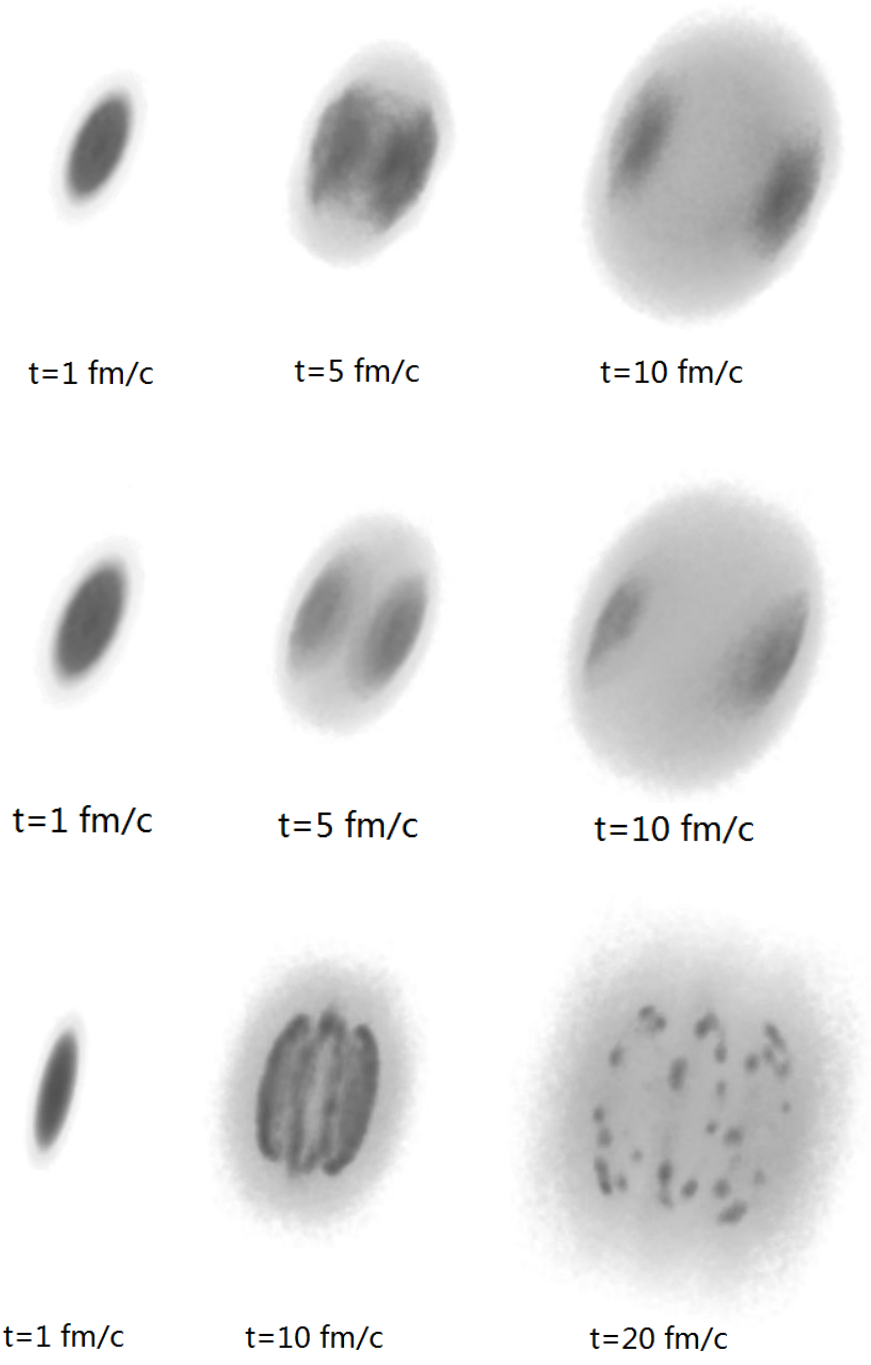

Figure 5.9: Time evolution of density distributions in central Au+Au collisions at $\sqrt{s_{NN}} = 2.5$ GeV using initial conditions from the AMPT for the cases of free streaming (upper row) and including mean fields from the SU(3) NJL model with $G_V = G_V$ (middle row) and $G_V = 0$ (lower row).

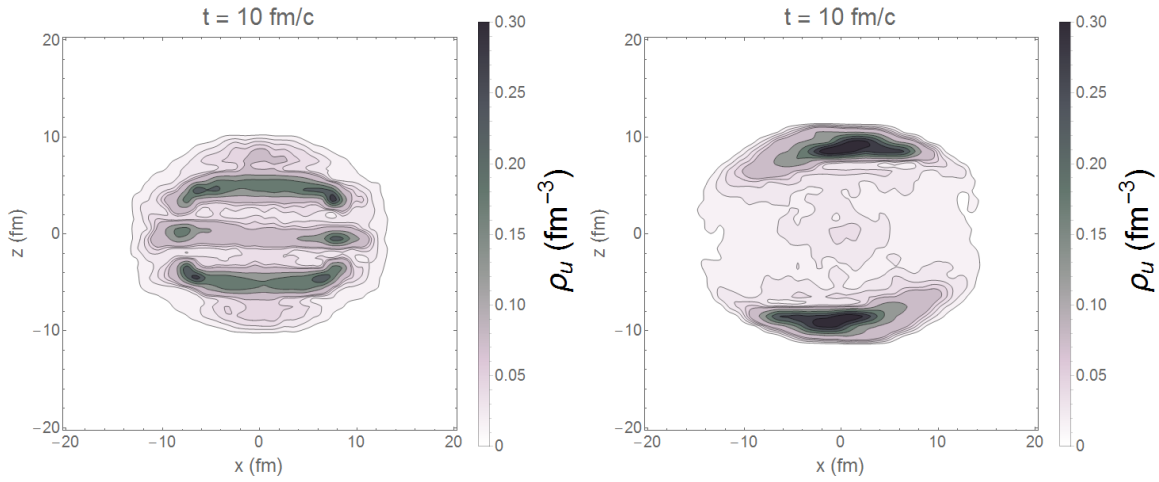

Figure 5.10: Density distribution of an expanding quark matter on the $y = 0$ plane at $t = 10$ fm/c with (left window) and without (right window) a first-order phase transition using the AMPT initial conditions.

the density fluctuations of an expanding quark matter due to its spinodal instability or a first-order phase transition. On the other hand, the different density variations along the beam (z) axis shown in Fig. 5.10 are expected to affect the parton rapidity distribution. This is because partons in the middle disc, which is present only in the case with a first-order phase transition, have a small rapidity and due to the attractive quark interactions, they attract partons from the other two discs and slow down their expansion in the longitudinal direction, thus restricting their rapidities to a narrow region around the midrapidity. As shown by the solid line in Fig. 5.11, the parton rapidity distribution in the case with a first-order phase transition is indeed much narrower than that in the case without a first-order phase transition, shown by the dashed line. This effect can be regarded as a possible signal of a first-order phase transition and is worth studying in experiments.

We have also studied the dilepton invariant mass spectrum from an expanding quark matter with initial conditions from the AMPT model. This is shown in

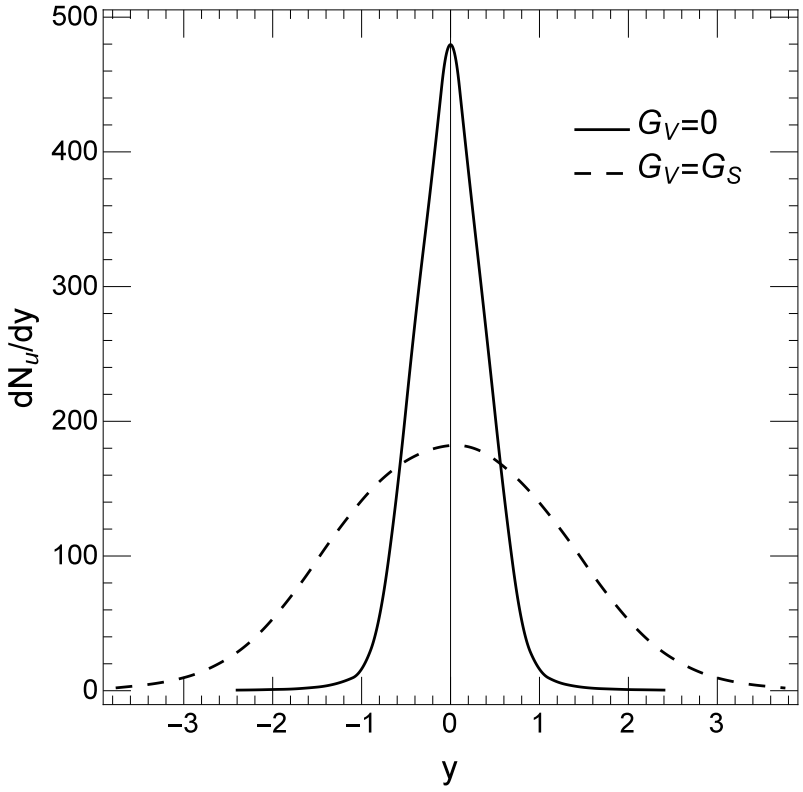

Figure 5.11: Final rapidity distribution of quarks for the cases with (solid curve) and without (dashed curve) a first-order phase transition from an expanding quark matter using the AMPT initial conditions.

Fig. 5.12 by solid and dashed lines for the cases with and without a first-order phase transition, respectively. As in the Section 5.1 using the blast-wave initial conditions, the presence of a first-order phase transition enhances the dilepton yield as a result of density fluctuations and longer partonic phase. However, the dilepton yield is lower than that obtained from the calculation with the blast wave initial condition by two orders of magnitude because there are very few antiquarks in the partonic matter produced in heavy ion collisions at such a low energy and also because we have not included the bremsstrahlung contribution to dilepton production from the quark-quark scattering.

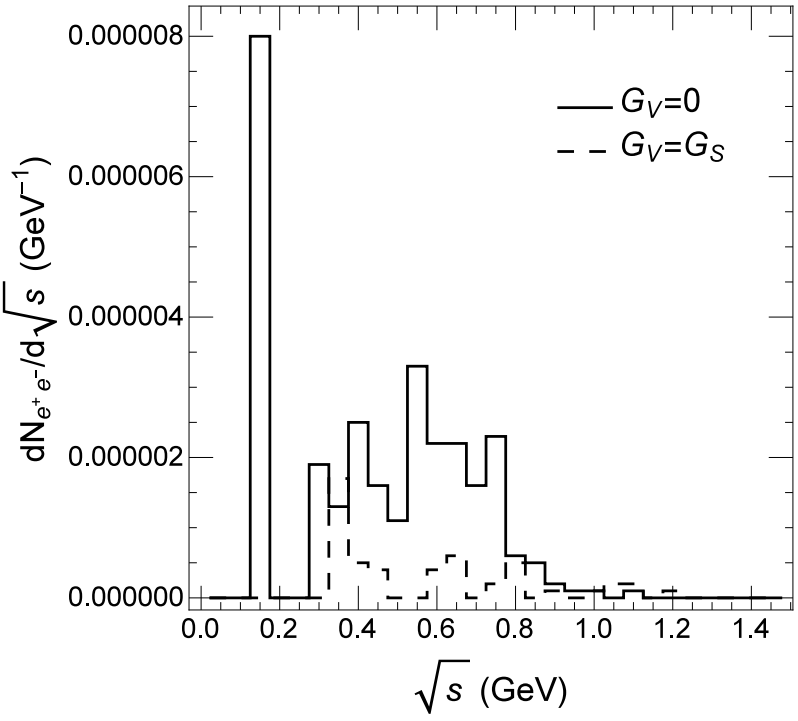

Figure 5.12: Dilepton yield as a function of invariant mass M for the cases with (solid curve) and without (dashed curve) a first-order phase transition from an expanding quark matter using the AMPT initial conditions.

In summary, we have introduced the AMPT initial conditions to the transport model with mean fields. In this case, the quark matter does not expand isotropically. Instead, the initial disc-like distribution splits into two discs, moving along the beam axis in opposite directions for both cases of free streaming and with mean fields but without a first-order phase transition. If the expanding quark matter undergoes a first order-phase transition, a third disc appears in the middle and pull the other two back towards it, resulting in a narrower rapidity distribution. Also, a first-order phase transition leads to an enhancement in the dilepton yield in a heavy ion collision.

6. SUMMARY

The spinodal instability is a thermodynamic feature of a first-order phase transition in a many-body system. It occurs when its pressure in some parts decreases with increasing density. This can amplify the density fluctuations and leads to a phase separation in the system. We have studied this phenomenon using both analytical and numerical approaches based on the NJL and PNJL models, which have been shown to give good descriptions of the properties of baryon free quark-gluon plasma and also predicts the existence of a first-order phase transition in baryon rich quark matter. Analytically, we have obtained the boundaries of the spinodal region and calculated the growth rate of unstable modes during the early stage. We find that at the mean-field level, the boundaries of spinodal instabilities shrink with the wave number of unstable modes. Both the vector interaction and quantum effects suppress the spinodal instability. For the former, the suppression is seen for all unstable modes, while for the latter, it acts only those of short wavelength. Also, we find the critical temperature T_c in the PNJL model is almost twice as large as in the NJL model, which can be understood as a result of the reduction of degrees of freedom below T_c due to confinement. Numerically, we have solved the Boltzmann equations by the test-particle method and obtained some intuitive pictures on the phase separation for a quark matter both in a static box and undergoing expansion. For the case of a static box, we find the growth rates extracted from the early growth of a sinusoidal density fluctuation to agree with the analytical results. We have also calculated the higher-order density moments of the quark matter and found them to increase and saturate at large values after phase separation, making them possible signals for the first-order phase transition. The skewness of the quark

number event-by-event distribution in a small sub-volume of the quark matter is also found to increase, but this feature disappears if the sub-volume is large. As for the expanding quark matter, two cases have been studied. One is based on the blast-wave initial conditions, while the other using the AMPT initial conditions, which are disc-like. In both cases, we find that the expansions are slowed down by the presence of a first-order phase transition. Density clumps are found to appear and lead to an anisotropy in the momentum space, which can be characterized by the scaled density moments and the anisotropic flows v_2 and v_4. An enhancement in the dilepton yield is also observed. The expansion of the quark matter with the AMPT initial conditions is more complex. Normally, the initial disc-like quark matter splits into two discs, moving along the beam axis in opposite directions. If the expanding quark matter undergoes a first order-phase transition, a third disc appears in the middle and pulls the other two discs back towards it, resulting in a narrower rapidity distribution.

In the future, we plan to develop a more consistent transport model, in which all cross sections are calculated self-consistently from the NJL model, so that the temperature and density dependence of the collisional effect can be taken into account. The dilepton production through the $qq \to qqe^+e^-$ process will also be included, since it could be the main contribution to the dilepton yield from a quark matter of high baryon chemical potential. We also plan to extend the transport model using the PNJL model, which is more realistic and agrees better with the lattice results for quark matter low baryon chemical potential. We hope that our study will help to understand the phase transition in the baryon-rich matter by comparing theoretical predictions with available and future experimental data.

REFERENCES

[1] F. Li, C. M. Ko, *Phys. Rev. C* **93**, 035205 (2016).

[2] A. Polyakov, *Phys. Lett. B* **72**, 477 (1978).

[3] D. J. Gross, R. D. Pisarski, L. G. Yaffe, *Rev. Mod. Phys.* **53**, 43 (1981).

[4] Y. Aoki, G. Endrodi, Z. Fodor, S. Katz, K. Szabo, *Nature* **443**, 675 (2006).

[5] E. Y. Loh, *et al.*, *Phys. Rev. B* **41**, 9301 (1990).

[6] M. Asakawa, Y. Koichi, *Nucl. Phys. A* **504**, 668 (1989).

[7] A. Barducci, R. Casalbuoni, S. D. Curtis, R. Gatto, G. Pettini, *Phys. Lett. B* **231**, 463 (1989).

[8] A. Barducci, R. Casalbuoni, S. De Curtis, R. Gatto, G. Pettini, *Phys. Rev. D* **41**, 1610 (1990).

[9] A. Barducci, R. Casalbuoni, G. Pettini, R. Gatto, *Phys. Rev. D* **49**, 426 (1994).

[10] M. A. Halasz, A. D. Jackson, R. E. Shrock, M. A. Stephanov, J. J. M. Verbaarschot, *Phys. Rev. D* **58**, 096007 (1998).

[11] J. Berges, K. Rajagopal, *Nucl. Phys. B* **538**, 215 (1999).

[12] R. Rapp, T. Schfer, E. V. Shuryak, M. Velkovsky, *Ann. Phys.* **280**, 35 (2000).

[13] O. Scavenius, A. Mócsy, I. N. Mishustin, D. H. Rischke, *Phys. Rev. C* **64**, 045202 (2001).

[14] N. Antoniou, A. Kapoyannis, *Phys. Lett. B* **563**, 165 (2003).

[15] Y. Hatta, T. Ikeda, *Phys. Rev. D* **67**, 014028 (2003).

[16] A. Barducci, R. Casalbuoni, G. Pettini, L. Ravagli, *Phys. Rev. D* **72**, 056002 (2005).

[17] M. He, J.-F. Li, W.-M. Sun, H.-S. Zong, *Phys. Rev. D* **79**, 036001 (2009).

[18] K. Fukushima, *Phys. Rev. D* **77**, 114028 (2008). [Erratum: Phys. Rev.D78,039902(2008)].

[19] S. Carignano, D. Nickel, M. Buballa, *Phys. Rev. D* **82**, 054009 (2010).

[20] S.-x. Qin, L. Chang, H. Chen, Y.-x. Liu, C. D. Roberts, *Phys. Rev. Lett.* **106**, 172301 (2011).

[21] N. M. Bratovic, T. Hatsuda, W. Weise, *Phys. Lett. B* **719**, 131 (2013).

[22] M. A. Stephanov, *Prog. Theor. Phys. Suppl.* **153**, 139 (2004).

[23] M. A. Stephanov, *Phys. Rev. Lett.* **102**, 032301 (2009).

[24] K. Morita, B. Friman, K. Redlich, V. Skokov, *Phys. Rev. C* **88**, 034903 (2013).

[25] B. Friman, *et al.*, *Lect. Notes Phys.* **814**, 1 (2011).

[26] T. K. Nayak, *Nucl. Phys. A* **830**, 555C (2009).

[27] M. M. Aggarwal, *et al.*, *Phys. Rev. Lett.* **105**, 022302 (2010).

[28] D. McDonald, *EPJ Web Conf.* **95**, 01009 (2015).

[29] L. Adamczyk, *et al.*, *Phys. Rev. Lett.* **110**, 142301 (2013).

[30] Z.-W. Lin, C. M. Ko, B.-A. Li, B. Zhang, S. Pal, *Phys. Rev. C* **72**, 064901 (2005).

[31] Y. Nambu, G. Jona-Lasinio, *Phys. Rev.* **122**, 345 (1961).

[32] Y. Nambu, G. Jona-Lasinio, *Phys. Rev.* **124**, 246 (1961).

[33] C. M. Ko, T. Song, F. Li, V. Greco, S. Plumari, *Nucl. Phys. A* **928**, 234 (2014).

[34] J. Xu, L.-W. Chen, C. M. Ko, Z.-W. Lin, *Phys. Rev. C* **85**, 041901 (2012).

[35] J. Xu, T. Song, C. M. Ko, F. Li, *Phys. Rev. Lett.* **112**, 012301 (2014).

[36] J. Steinheimer, J. Randrup, *Phys. Rev. Lett.* **109**, 212301 (2012).

[37] C. Herold, M. Nahrgang, I. Mishustin, M. Bleicher, *Nucl. Phys. A* **925**, 14 (2014).

[38] C. Herold, M. Nahrgang, I. Mishustin, M. Bleicher, *J. Phys. Conf. Ser.* **509**, 012065 (2014).

[39] J. Steinheimer, J. Randrup, V. Koch, *Phys. Rev. C* **89**, 034901 (2014).

[40] G. 't Hooft, *Phys. Rev. D* **14**, 3432 (1976).

[41] M. Buballa, *Phys. Rept.* **407**, 205 (2005).

[42] B. R. Holstein, *Phys. Lett. B* **244**, 83 (1990).

[43] T. Hatsuda, T. Kunihiro, *Phys. Lett. B* **185**, 304 (1987).

[44] N. Weiss, *Phys. Rev. D* **24**, 475 (1981).

[45] N. Weiss, *Phys. Rev.D* **25**, 2667 (1982).

[46] K. Fukushima, *Phys. Lett. B* **591**, 277 (2004).

[47] S. Roessner, C. Ratti, W. Weise, *Phys. Rev. D* **75**, 034007 (2007).

[48] C. A. de Sousa, P. Costa, M. C. Ruivo, H. Hansen, *AIP Conf. Proc.* **1343**, 592 (2011).

[49] P. Costa, M. C. Ruivo, C. A. de Sousa, H. Hansen, *Symmetry* **2**, 1338 (2010).

[50] S. Borsányi, *et al.*, *J. High Energy Phys.* **2010**, 1 (2010).

[51] T. Bhattacharya, *et al.*, *Phys. Rev. Lett.* **113**, 082001 (2014).

[52] A. Bazavov, *et al.*, *Phys. Rev. D* **90**, 094503 (2014).

[53] T. Hatsuda, T. Kunihiro, *Phys. Rept.* **247**, 221 (1994).

[54] M. Dutra, O. Lourenço, A. Delfino, T. Frederico, M. Malheiro, *Phys. Rev. D* **88**, 114013 (2013).

[55] J. Randrup, *Phys. Rev. C* **82**, 034902 (2010).

[56] J. Steinheimer, J. Randrup, *Phys. Rev. C* **87**, 054903 (2013).

[57] O. Yilmaz, S. Ayik, F. Acar, S. Saatci, A. Gokalp, *Eur. Phys. J. A* **49**, 33 (2013).

[58] S. Ayik, O. Yilmaz, N. Er, A. Gokalp, P. Ring, *Phys. Rev. C* **80**, 034613 (2009).

[59] J. Rammer, *Quantum field theory of non-equilibrium states* (Cambridge, UK: Univ. Pr. (2007) 536 p, 2007).

[60] P. C. Martin, J. S. Schwinger, *Phys. Rev.* **115**, 1342 (1959).

[61] J. Randrup, *Phys. Rev. C* **79**, 054911 (2009).

[62] M. B. Pinto, V. Koch, J. Randrup, *Phys. Rev. C* **86**, 025203 (2012).

[63] P. Chakraborty, J. I. Kapusta, *Phys. Rev. C* **83**, 014906 (2011).

[64] B. H. Alver, C. Gombeaud, M. Luzum, J.-Y. Ollitrault, *Phys. Rev. C* **82**, 034913 (2010).

[65] S. Wang, *et al.*, *Phys. Rev. C* **44**, 1091 (1991).

[66] N. Borghini, P. M. Dinh, J.-Y. Ollitrault, *Phys. Rev. C* **64**, 054901 (2001).

[67] T. Galatyuk, P. M. Hohler, R. Rapp, F. Seck, J. Stroth (2015).

[68] X.-N. Wang, *Phys. Rev. D* **43**, 104 (1991).

[69] X.-N. Wang, M. Gyulassy, *Phys. Rev. D* **44**, 3501 (1991).

[70] M. Gyulassy, X.-N. Wang, *Comput. Phys. Commun.* **83**, 307 (1994).

[71] T. Sjstrand, *Comput. Phys. Commun.* **82**, 74 (1994).

[72] B. Zhang, *Comput. Phys. Commun.* **109**, 193 (1998).

[73] B.-A. Li, C. M. Ko, *Phys. Rev. C* **52**, 2037 (1995).

[74] B.-A. LI, A. T. Sustich, B. Zhang, C. M. Ko, *Int. J. Mod. Phys. E* **10**, 267 (2001).

[75] S. P. Klevansky, A. Ogura, J. Hufner, *Ann. Phys.* **261**, 37 (1997).

[76] J. S. Schwinger, *J. Math. Phys.* **2**, 407 (1961).

[77] L. Keldysh, *Zh. Eksp. Teor. Fiz.* **47**, 1515 (1964).

[78] C.-Y. Wong, *Phys. Rev. C* **25**, 1460 (1982).

APPENDIX A

STATISTICS OF CONFINED QUARKS

In this appendix, we discuss in detail the statistics of confined quarks, especially the effect of reduced color degrees of freedom below the confinement-deconfinement temperature due to the Polyakov loop. This effect can be seen explicitly in the expression shown below.

Since the background gauge field A_4 in Eq. (1.1) is traceless, it can be diagonalized in the color space and rewritten as $A_4 = U\mathrm{diag}\{\phi^1, \phi^2, \cdots, \phi^{N_c}\}U^{-1}$ with $\sum_{a=1}^{N_c} \phi^a = 0$. The Polyakov loop then becomes

$$\Phi(\mathbf{x}) = \frac{1}{N_c}\mathrm{Tr}\left[U\exp\left(i\beta\mathrm{diag}\{\bar{\phi}^1, \bar{\phi}^2, \cdots, \bar{\phi}^{N_c}\}\right)U^{-1}\right] = \frac{1}{N_c}\sum_{a=1}^{N_c}\exp(i\beta\bar{\phi}^a), \quad \text{(A.1)}$$

where

$$\bar{\phi}^a = \frac{1}{\beta}P\int_0^\beta \phi^a(\mathbf{x},\tau)d\tau \quad \text{(A.2)}$$

is the τ averaged background field. In the confined phase, $\Phi = 0$, which means $\sum_{a=1}^{N_c}\exp(i\beta\bar{\phi}^a) = 0$, a symmetric solution is $\exp(i\beta\bar{\phi}^a) = (-1)^{2a/N_c}$. Acting the $\bar{\phi}^a$ on free quarks, the quark sector of the QCD action in the $S^1 \times E^3$ space is then

$$\mathcal{S}_q = -\int_0^\beta \mathrm{d}\tau\mathrm{d}\mathbf{x}^3\bar{q}^a(-\gamma^0\partial_\tau + i\boldsymbol{\gamma}\cdot\nabla - m + \gamma^0(\mu + i\bar{\phi}^a))q^a. \quad \text{(A.3)}$$

$\bar{\phi}^a$ can thus be absorbed in the chemical potential μ by redefining $\widetilde{\mu}^a = \mu + i\bar{\phi}^a$. The quark equilibrium distribution is thus

$$f_0^a(E) = \frac{1}{e^{\frac{E\mp\widetilde{\mu}^a}{T}}+1} = \frac{1}{(-1)^{2a/N_c}e^{\frac{E\mp\mu}{T}}+1}. \quad \text{(A.4)}$$

Defining $\xi \equiv e^{\frac{E\mp\mu}{T}}$ and $z_a \equiv \exp(i\beta\bar{\phi}^a) = (-1)^{2a/N_c}$, and using $\sum_{a=1}^{N_c} z_a^n = N_c\delta_{n,(kN_c)}$, where $k \in \mathbb{Z}$, the color average of Eq. (A.4) is then

$$\begin{aligned} \bar{f}_0 &= \frac{1}{N_c}\sum_{a=1}^{N_c}\frac{1}{z_a\xi+1} = \frac{1}{N_c}\sum_{a=1}^{N_c}\sum_{k=0}^{\infty} z_a^k(-\xi)^k = \sum_{k=0}^{\infty}(-\xi)^{kN_c} \\ &= \frac{1}{-(-\xi)^{N_c}+1} = \frac{1}{(-)^{N_c+1}e^{\frac{E-\mu}{T/N_c}}+1}. \end{aligned} \tag{A.5}$$

The above equation shows that the color-averaged distribution of confined quarks is same as the distribution of a free quark gas, but with the temperature being $1/N_c$ of the original one. Physically, the quark degrees of freedom are reduced by $1/N_c$ due to confinement. As a result, confined quarks take only $1/N_c$ energy from the heat bath as free quarks would take, which makes them appear "cold".

Eq. (A.5) also shows that the distribution looks bosonic if N_c is even. In fact, the statistics of confined quarks is neither fermionic nor bosonic, but N_c-anyonic. This can be seen by applying the gauge transformation $q^a(\tau,\mathbf{x}) \to q^{a\prime}(\tau,\mathbf{x}) = \exp(-i\tau\bar{\phi}^a)q^a(\tau,\mathbf{x})$, so that the coupling term $i\bar{q}^a\gamma^0\bar{\phi}^a q^a$ in Eq. (A.3) vanishes. Quarks are then free under the new gauge. The price paid is that the anti-periodic boundary condition on τ axis is broken: $q^a(\beta,\mathbf{x}) = (-1)^{1-2a/N_c}q(0,\mathbf{x})$. The equilibrium distributions are thus different.

In a more general case, quarks are neither perfectly confined nor completely free, which means the Polyakov loop $|\Phi|$ is between 0 and 1. In the case of $N_c = 3$, the color-averaged quark distribution is

$$\begin{aligned} \bar{f}_0 &= \frac{1}{3}\left(\frac{1}{z_1\xi+1}+\frac{1}{z_2\xi+1}+\frac{1}{z_3\xi+1}\right) \\ &= \frac{1}{3}\frac{(z_1^{-1}+z_2^{-1}+z_3^{-1})\xi^2+2(z_1+z_2+z_3)\xi+3}{\xi^3+(z_1^{-1}+z_2^{-1}+z_3^{-1})\xi^2+(z_1+z_2+z_3)\xi+1} \end{aligned}$$

$$= \frac{\bar{\Phi} e^{\frac{E \mp \mu}{T/2}} + 2\Phi e^{\frac{E \mp \mu}{T}} + 1}{e^{\frac{E \mp \mu}{T/3}} + 3\bar{\Phi} e^{\frac{E \mp \mu}{T/2}} + 3\Phi e^{\frac{E \mp \mu}{T}} + 1}, \tag{A.6}$$

where the second equality follows from $z_1 z_2 z_3 = 1$, as $\bar{\phi}$ is traceless. Compared to the Fermi-Dirac distribution at same temperature and baryon chemical potential, f_Φ is larger for low-energy states and smaller for high energy states.

APPENDIX B

EXPRESSIONS FOR QUARK CORRELATORS AND THE SEMICLASSICAL APPROXIMATION

B.1 Explicit form for the quark correlator

In this Appendix, we give the explicit expressions for the correlators $i\widetilde{\chi}$s used in our calculations:

$$
\begin{aligned}
i\widetilde{\chi}_{\sigma\sigma}(i\gamma,k) &= -\frac{N_F}{\pi^2}\int_0^{\Lambda-k} dp \frac{p^2}{4E_p}\mathcal{A}(p;T,\mu)\left[4-\frac{1}{pk}\left(\frac{\gamma^2+k^2}{2}+2M^2\right)\mathcal{F}_1(p,\gamma,k)\right] \\
&\quad -\frac{N_F}{\pi^2}\int_{\Lambda-k}^{\Lambda} dp \frac{p^2}{4E_p}\mathcal{A}(p;T,\mu)\left[\frac{\Lambda^2-(p-k)^2}{kp}\right. \\
&\quad \left.+\frac{1}{pk}\left(\frac{\gamma^2+k^2}{2}+2M^2\right)\mathcal{G}_1(p,\gamma,k,\Lambda)\right], \qquad \text{(B.1)} \\
i\widetilde{\chi}^0_{\sigma j}(i\gamma,k) &= -\frac{N_F M}{\pi^2}\int_{\Lambda-k}^{\Lambda} dp \frac{p}{2k}\mathcal{B}(p;T,\mu)\left[-\mathcal{G}_1(p,\gamma,k,\Lambda)+\frac{\gamma}{E_p}\mathcal{G}_2(p,\gamma,k,\Lambda)\right] \\
&\quad -\frac{N_F M}{\pi^2}\int_0^{\Lambda-k} dp \frac{p}{2k}\mathcal{B}(p;T,\mu)\left[\mathcal{F}_1(p,\gamma,k)+\frac{\gamma}{E_p}\mathcal{F}_2(p,\gamma,k)\right], \qquad \text{(B.2)} \\
i\widetilde{\chi}^3_{\sigma j}(i\gamma,k) &= -\frac{N_F M i}{\pi^2}\int_0^{\Lambda-k} dp \frac{p}{2E_p}\mathcal{B}(p;T,\mu)\left[-\frac{\gamma E_p}{k^2}\mathcal{F}_1(p,\gamma,k)+\frac{\gamma^2}{k^2}\mathcal{F}_2(p,\gamma,k)\right] \\
&\quad -\frac{iN_F M\gamma^2}{\pi^2 k^2}\int_{\Lambda-k}^{\Lambda} dp \frac{p}{2E_p}\mathcal{B}(p;T,\mu)\left[\frac{E_p}{\gamma}\mathcal{G}_1(p,\gamma,k,\Lambda)+\mathcal{G}_2(p,\gamma,k,\Lambda)\right], \qquad \text{(B.3)} \\
i\widetilde{\chi}^{00}_{jj}(i\gamma,k) &= \frac{N_F}{\pi^2}\int_0^{\Lambda-k} dp \frac{p^2}{4E_p}\mathcal{A}(p;T,\mu) \\
&\quad \times\left[\frac{4E_p^2-\gamma^2-k^2}{2kp}\mathcal{F}_1(p,\gamma,k)+4-\frac{4E_p\gamma}{kp}\mathcal{F}_2(p,\gamma,k)\right] \\
&\quad +\frac{N_F}{\pi^2}\int_{\Lambda-k}^{\Lambda} dp \frac{p^2}{4E_p}\mathcal{A}(p;T,\mu)\left[-\frac{4E_p^2-\gamma^2-k^2}{2kp}\mathcal{G}_1(p,\gamma,k,\Lambda)\right. \\
&\quad \left.+\frac{\Lambda^2-(p-k)^2}{kp}-\frac{4E_p\gamma}{kp}\mathcal{G}_2(p,\gamma,k,\Lambda)\right], \qquad \text{(B.4)}
\end{aligned}
$$

$$
\begin{aligned}
i\widetilde{\chi}^{03}_{jj}(i\gamma,k) &= \frac{N_F i}{\pi^2}\int_0^{\Lambda-k} dp \frac{p^2}{2k}\mathcal{A}(p;T,\mu) \\
&\times\left[\frac{\gamma(4E_p^2-\gamma^2-k^2)}{4E_pkp}\mathcal{F}_1(p,\gamma,k)+\frac{2\gamma}{E_p}-\frac{2\gamma^2}{kp}\mathcal{F}_2(p,\gamma,k)\right] \\
&+\frac{N_F i}{\pi^2}\int_{\Lambda-k}^{\Lambda} dp \frac{p^2}{2k}\mathcal{A}(p;T,\mu)\Bigg[-\frac{\gamma(4E_p^2-\gamma^2-k^2)}{4E_pkp}\mathcal{G}_1(p,\gamma,k,\Lambda) \\
&+\frac{\gamma}{E_p}\frac{\Lambda^2-(p-k)^2}{2kp}-\frac{2\gamma^2}{kp}\mathcal{G}_2(p,\gamma,k,\Lambda)\Bigg], \qquad \text{(B.5)} \\
i\widetilde{\chi}^{33}_{jj}(i\gamma,k) &= -\frac{N_F}{\pi^2}\int_0^{\Lambda-k} dp \frac{p^2}{2E_p}\mathcal{A}(p;T,\mu) \\
&\times\left[\frac{\gamma^2(4E_p^2-\gamma^2-k^2)}{4pk^3}\mathcal{F}_1(p,\gamma,k)+\frac{2\gamma^2}{k^2}-\frac{2\gamma^3E_p}{k^3p}\mathcal{F}_2(p,\gamma,k)\right] \\
&-\frac{N_F}{\pi^2}\int_{\Lambda-k}^{\Lambda} dp \frac{p^2}{2E_p}\mathcal{A}(p;T,\mu)\Bigg[-\frac{\gamma^2(4E_p^2-\gamma^2-k^2)}{4pk^3}\mathcal{G}_1(p,\gamma,k,\Lambda) \\
&+\frac{\gamma^2}{k^2}\frac{\Lambda^2-(p-k)^2}{2kp}-\frac{2\gamma^3E_p}{k^3p}\mathcal{G}_2(p,\gamma,k,\Lambda)\Bigg], \qquad \text{(B.6)}
\end{aligned}
$$

where

$$
\begin{aligned}
\mathcal{A}(p;T,\mu) &= 3-\sum_{i=1}^{3} f_0(p;T,\tilde{\mu}_i)-\sum_{i=1}^{3} f_0(p;T,-\tilde{\mu}_i), \qquad \text{(B.7)} \\
\mathcal{B}(p;T,\mu) &= \sum_{i=1}^{3} f_0(p;T,\tilde{\mu}_i)-\sum_{i=1}^{3} f_0(p;T,-\tilde{\mu}_i), \qquad \text{(B.8)} \\
\mathcal{F}_1(p,\gamma,k) &= \ln\left|\frac{(\gamma^2+k^2+2kp)^2+4\gamma^2E_p^2}{(\gamma^2+k^2-2kp)^2+4\gamma^2E_p^2}\right|, \qquad \text{(B.9)} \\
\mathcal{F}_2(p,\gamma,k) &= \arctan\left(\frac{2\gamma E_p}{\gamma^2+k^2-2kp}\right)-\arctan\left(\frac{2\gamma E_p}{\gamma^2+k^2+2kp}\right), \qquad \text{(B.10)} \\
\mathcal{G}_1(p,\gamma,k,\Lambda) &= \ln\left|\frac{(\gamma^2+k^2-2kp)^2+4\gamma^2E_p^2}{(\Lambda^2+\gamma^2-p^2)^2+4\gamma^2E_p^2}\right|, \qquad \text{(B.11)} \\
\mathcal{G}_2(p,\gamma,k,\Lambda) &= \arctan\left(\frac{2\gamma E_p}{\gamma^2+k^2-2kp}\right)-\arctan\left(\frac{2\gamma E_p}{\Lambda^2+\gamma^2-p^2}\right) \qquad \text{(B.12)}
\end{aligned}
$$

with $\tilde{\mu}_{1,2}=\mu-2G_Vj^0\pm i\phi_3$ and $\tilde{\mu}_3=\mu-2G_Vj^0$ are the effective chemical potentials.

B.2 Semiclassical approximation to the quark correlator

In the classical limit, namely $\hbar \to 0$, the correlators $\widetilde{\chi}$s can be simplified. Expanding each term to the order of $\hbar$ by using $E_{\mathbf{p}+\hbar\mathbf{k}} = E_{\mathbf{p}} + \hbar\mathbf{k}\cdot\mathbf{p}/E_{\mathbf{p}} + \mathcal{O}(\hbar^2)$ and $f(E_{\mathbf{p}+\hbar\mathbf{k}} \pm \widetilde{\mu}^a) = f(E_{\mathbf{p}} \pm \widetilde{\mu}^a) + \hbar\mathbf{k}\cdot\nabla_{\mathbf{p}} f(E_{\mathbf{p}} \pm \widetilde{\mu}^a) + \mathcal{O}(\hbar^2)$, we then have

$$\begin{aligned}
\frac{f_0(E_{\mathbf{p}} - \widetilde{\mu}_a) - f_0(E_{\mathbf{p}+\hbar\mathbf{k}} - \widetilde{\mu}_a)}{E_{\mathbf{p}+\hbar\mathbf{k}} - E_{\mathbf{p}} - \hbar\omega - i0^+} &= \frac{\mathbf{k}\cdot\nabla_{\mathbf{p}} f_0(E_{\mathbf{p}} - \widetilde{\mu}_a)}{\omega - \mathbf{p}\cdot\mathbf{k}/E_{\mathbf{p}}} + \mathcal{O}(\hbar), \\
\frac{f_0(E_{\mathbf{p}+\hbar\mathbf{k}} + \widetilde{\mu}_a) - f_0(E_{\mathbf{p}} + \widetilde{\mu}_a)}{E_{\mathbf{p}} - E_{\mathbf{p}+\hbar\mathbf{k}} - \hbar\omega - i0^+} &= \frac{-\mathbf{k}\cdot\nabla_{\mathbf{p}} f_0(E_{\mathbf{p}} + \widetilde{\mu}_a)}{\omega + \mathbf{p}\cdot\mathbf{k}/E_{\mathbf{p}}} + \mathcal{O}(\hbar), \\
\frac{f_0(E_{\mathbf{p}+\hbar\mathbf{k}} + \widetilde{\mu}_a) + f_0(E_{\mathbf{p}} - \widetilde{\mu}_a) - 1}{-E_{\mathbf{p}} - E_{\mathbf{p}+\hbar\mathbf{k}} - \hbar\omega - i0^+} &= \frac{1 - f_0(E_{\mathbf{p}} + \widetilde{\mu}_a) - f_0(E_{\mathbf{p}} - \widetilde{\mu}_a)}{2E_{\mathbf{p}}} + \mathcal{O}(\hbar), \\
\frac{1 - f_0(E_{\mathbf{p}+\hbar\mathbf{k}} - \widetilde{\mu}_a) - f_0(E_{\mathbf{p}} + \widetilde{\mu}_a)}{E_{\mathbf{p}} + E_{\mathbf{p}+\hbar\mathbf{k}} - \hbar\omega - i0^+} &= \frac{1 - f_0(E_{\mathbf{p}} + \widetilde{\mu}_a) - f_0(E_{\mathbf{p}} - \widetilde{\mu}_a)}{2E_{\mathbf{p}}} + \mathcal{O}(\hbar),
\end{aligned} \tag{B.13}$$

and

$$\begin{aligned}
\mathrm{Tr}[\Delta_+(\mathbf{p})\Delta_+(\hbar\mathbf{k}+\mathbf{p})] &= \mathrm{Tr}[\Delta_-(\mathbf{p})\Delta_-(\hbar\mathbf{k}+\mathbf{p})] = 8\frac{M^2}{E_{\mathbf{p}}^2} + \mathcal{O}(\hbar^2), \\
\mathrm{Tr}[\Delta_-(\mathbf{p})\Delta_+(\hbar\mathbf{k}+\mathbf{p})] &= \mathrm{Tr}[\Delta_+(\mathbf{p})\Delta_-(\hbar\mathbf{k}+\mathbf{p})] = 8\frac{\mathbf{p}^2}{E_{\mathbf{p}}^2} + \mathcal{O}(\hbar), \\
\mathrm{Tr}[\Delta_+(\mathbf{p})\gamma^0\Delta_+(\hbar\mathbf{k}+\mathbf{p})] &= -\mathrm{Tr}[\Delta_-(\mathbf{p})\gamma^0\Delta_-(\hbar\mathbf{k}+\mathbf{p})] = 8\frac{M}{E_{\mathbf{p}}} + \mathcal{O}(\hbar), \\
\mathrm{Tr}[\Delta_-(\mathbf{p})\gamma^0\Delta_+(\hbar\mathbf{k}+\mathbf{p})] &= -\mathrm{Tr}[\Delta_+(\mathbf{p})\gamma^0\Delta_-(\hbar\mathbf{k}+\mathbf{p})] = \mathcal{O}(\hbar), \\
\mathrm{Tr}[\Delta_+(\mathbf{p})\gamma^3\Delta_+(\hbar\mathbf{k}+\mathbf{p})] &= \mathrm{Tr}[\Delta_-(\mathbf{p})\gamma^3\Delta_-(\hbar\mathbf{k}+\mathbf{p})] = 8\frac{M\mathbf{p}\cdot\hat{\mathbf{k}}}{E_{\mathbf{p}}^2} + \mathcal{O}(\hbar), \\
\mathrm{Tr}[\Delta_-(\mathbf{p})\gamma^3\Delta_+(\hbar\mathbf{k}+\mathbf{p})] &= \mathrm{Tr}[\Delta_+(\mathbf{p})\gamma^3\Delta_-(\hbar\mathbf{k}+\mathbf{p})] = 8\frac{M\mathbf{p}\cdot\hat{\mathbf{k}}}{E_{\mathbf{p}}^2} + \mathcal{O}(\hbar), \\
\mathrm{Tr}[\gamma^0\Delta_+(\mathbf{p})\gamma^0\Delta_+(\hbar\mathbf{k}+\mathbf{p})] &= \mathrm{Tr}[\gamma^0\Delta_-(\mathbf{p})\gamma^0\Delta_-(\hbar\mathbf{k}+\mathbf{p})] = 8 + \mathcal{O}(\hbar^2), \\
\mathrm{Tr}[\gamma^0\Delta_-(\mathbf{p})\gamma^0\Delta_+(\hbar\mathbf{k}+\mathbf{p})] &= \mathrm{Tr}[\gamma^0\Delta_+(\mathbf{p})\gamma^0\Delta_-(\hbar\mathbf{k}+\mathbf{p})] = \mathcal{O}(\hbar), \\
\mathrm{Tr}[\gamma^3\Delta_+(\mathbf{p})\gamma^3\Delta_+(\hbar\mathbf{k}+\mathbf{p})] &= \mathrm{Tr}[\gamma^3\Delta_-(\mathbf{p})\gamma^3\Delta_-(\hbar\mathbf{k}+\mathbf{p})] = 8\frac{(\mathbf{p}\cdot\hat{\mathbf{k}})^2}{E_{\mathbf{p}}^2} + \mathcal{O}(\hbar^2),
\end{aligned}$$

$$
\begin{aligned}
\mathrm{Tr}[\gamma^3\Delta_-(\mathbf{p})\gamma^3\Delta_+(\hbar\mathbf{k}+\mathbf{p})] &= \mathrm{Tr}[\gamma^3\Delta_+(\mathbf{p})\gamma^3\Delta_-(\hbar\mathbf{k}+\mathbf{p})] \\
&= 8\left(\frac{(\mathbf{p}\cdot\hat{\mathbf{k}})^2}{E_{\mathbf{p}}^2}-1\right)+\mathcal{O}(\hbar), \\
\mathrm{Tr}[\gamma^0\Delta_+(\mathbf{p})\gamma^3\Delta_+(\hbar\mathbf{k}+\mathbf{p})] &= -\mathrm{Tr}[\gamma^3\Delta_-(\mathbf{p})\gamma^3\Delta_-(\hbar\mathbf{k}+\mathbf{p})] = 8\frac{\mathbf{p}\cdot\hat{\mathbf{k}}}{E_{\mathbf{p}}}+\mathcal{O}(\hbar^2), \\
\mathrm{Tr}[\gamma^0\Delta_-(\mathbf{p})\gamma^3\Delta_+(\hbar\mathbf{k}+\mathbf{p})] &= -\mathrm{Tr}[\gamma^3\Delta_+(\mathbf{p})\gamma^3\Delta_-(\hbar\mathbf{k}+\mathbf{p})] \\
&= -8\frac{\mathbf{p}\cdot\hat{\mathbf{k}}}{E_{\mathbf{p}}}+\mathcal{O}(\hbar). \qquad \text{(B.14)}
\end{aligned}
$$

Using the above results, the correlators in the classical limit are

$$
\begin{aligned}
i\widetilde{\chi}_{\sigma\sigma}(\omega,\mathbf{k}) &\approx 2\sum_{a=1}^{3}\int_{|\mathbf{p}|<\Lambda}\frac{d^3\mathbf{p}}{(2\pi)^3}\Big\{\frac{\mathbf{p}^2}{E_{\mathbf{p}}^3}(1-f_0(E_{\mathbf{p}}+\widetilde{\mu}_a)-f_0(E_{\mathbf{p}}-\widetilde{\mu}_a)) \\
&\quad +\frac{M^2}{E_{\mathbf{p}}^2}\frac{\mathbf{k}\cdot\nabla_{\mathbf{p}}(f_0(E_{\mathbf{p}}-\widetilde{\mu}_a)+f_0(E_{\mathbf{p}}+\widetilde{\mu}_a))}{\omega-\mathbf{p}\cdot\mathbf{k}/E_{\mathbf{p}}}\Big\}, \\
i\widetilde{\chi}^0_{\sigma j}(\omega,\mathbf{k}) &\approx 2\sum_{a=1}^{3}\int_{|\mathbf{p}|<\Lambda}\frac{d^3\mathbf{p}}{(2\pi)^3}\frac{M}{E_{\mathbf{p}}}\frac{\mathbf{k}\cdot\nabla_{\mathbf{p}}(f_0(E_{\mathbf{p}}-\widetilde{\mu}_a)-f_0(E_{\mathbf{p}}+\widetilde{\mu}_a))}{\omega-\mathbf{p}\cdot\mathbf{k}/E_{\mathbf{p}}}, \\
i\widetilde{\chi}^z_{\sigma j}(\omega,\mathbf{k}) &\approx 2\sum_{a=1}^{3}\int_{|\mathbf{p}|<\Lambda}\frac{d^3\mathbf{p}}{(2\pi)^3}\left(\frac{M\mathbf{p}\cdot\hat{\mathbf{k}}}{E_{\mathbf{p}}^2}\right)\frac{\mathbf{k}\cdot\nabla_{\mathbf{p}}(f_0(E_{\mathbf{p}}-\widetilde{\mu}_a)+f_0(E_{\mathbf{p}}+\widetilde{\mu}_a))}{\omega-\mathbf{p}\cdot\mathbf{k}/E_{\mathbf{p}}}, \\
i\widetilde{\chi}^{00}_{jj}(\omega,\mathbf{k}) &\approx 2\sum_{a=1}^{3}\int_{|\mathbf{p}|<\Lambda}\frac{d^3\mathbf{p}}{(2\pi)^3}\frac{\mathbf{k}\cdot\nabla_{\mathbf{p}}(f_0(E_{\mathbf{p}}-\widetilde{\mu}_a)+f_0(E_{\mathbf{p}}+\widetilde{\mu}_a))}{\omega-\mathbf{p}\cdot\mathbf{k}/E_{\mathbf{p}}}, \\
i\widetilde{\chi}^{0z}_{jj}(\omega,\mathbf{k}) &\approx 2\sum_{a=1}^{3}\int_{|\mathbf{p}|<\Lambda}\frac{d^3\mathbf{p}}{(2\pi)^3}\left(\frac{\mathbf{p}\cdot\hat{\mathbf{k}}}{E_{\mathbf{p}}}\right)\frac{\mathbf{k}\cdot\nabla_{\mathbf{p}}(f_0(E_{\mathbf{p}}-\widetilde{\mu}_a)+f_0(E_{\mathbf{p}}+\widetilde{\mu}_a))}{\omega-\mathbf{p}\cdot\mathbf{k}/E_{\mathbf{p}}}, \\
i\widetilde{\chi}^{zz}_{jj}(\omega,\mathbf{k}) &\approx 2\sum_{a=1}^{3}\int_{|\mathbf{p}|<\Lambda}\frac{d^3\mathbf{p}}{(2\pi)^3}\Big\{\left(\frac{(\mathbf{p}\cdot\hat{\mathbf{k}})^2}{E_{\mathbf{p}}^2}-1\right)(1-f_0(E_{\mathbf{p}}+\widetilde{\mu}_a)-f_0(E_{\mathbf{p}}-\widetilde{\mu}_a)) \\
&\quad +\left(\frac{(\mathbf{p}\cdot\hat{\mathbf{k}})^2}{E_{\mathbf{p}}^2}\right)\frac{\mathbf{k}\cdot\nabla_{\mathbf{p}}(f_0(E_{\mathbf{p}}-\widetilde{\mu}_a)+f_0(E_{\mathbf{p}}+\widetilde{\mu}_a))}{\omega-\mathbf{p}\cdot\mathbf{k}/E_{\mathbf{p}}}\Big\}. \qquad \text{(B.15)}
\end{aligned}
$$

Comparing above $\widetilde{\chi}$s with Eqs. (3.49) and (3.50), we find that they are the same as those obtained by solving the linearized Boltzmann equations without the collisional term. Since Eq. (B.15) shows that all correlators in the classical limit are functions of ω/k, the solution to Eq. (3.18) in the classical limit should be $\omega_{\mathbf{k}} = C\mathbf{k}$, where C

is some constant. Furthermore, since $\hbar$ always comes with $\mathbf{k}$ and ω, the growth rates calculated in both quantum and classical case should agree in the long wavelength (small k) limit, although the quantum correction is significant in the short wavelength (large k) limit.

APPENDIX C

TRANSPORT EQUATIONS

C.1 Derivation of transport equations

The transport equations based on the SU(2) NJL model without the vector interaction were previously derived in Ref. [75] from the non-equilibrium Green's functions. In this appendix, the same method is used to derive the transport equations for the SU(3) case with the vector interaction for quarks and antiquarks. Since the collisional terms in this case are of the same form as in the SU(2) case, only the mean-field or Vlasov part of the transport equations is derived to take into account the effect due to the additional quark vector interaction that leads to a Lorentz-like force.

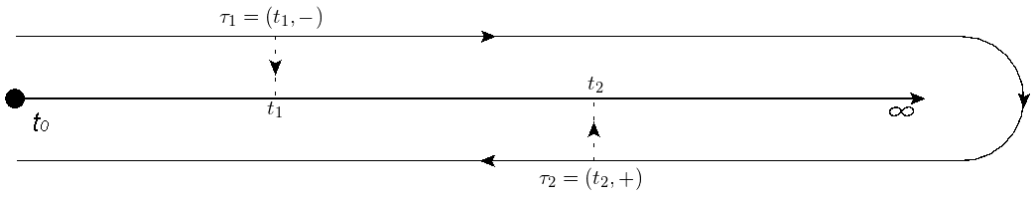

Figure C.1: The τ path, on which the non-equilibrium Green's function is defined, is composed of a forward path directing to the future and a backward path directing to the past, leading to the path-dependent times $(t, -)$ and $(t, +)$ on these two paths, respectively.

The dynamics of a quark in a quark matter can be described by its non-equilibrium Green's function $G(1, 1')$, where $1 = (\tau_1, \mathbf{x}_1, s_1, c_1, \cdots)$ denotes the time, position, spin, color, and other quantum numbers of the quark, defined on a path-dependent

time as shown in Fig. C.1 with the forward path directing to the future and the backward path directing to the past. The Green's function then satisfies the Dyson equations [59]:

$$G(1,1') = G_0(1,1') + G_0(1,2) \otimes \Sigma(2,3) \otimes G(3,1'), \tag{C.1}$$

$$G(1,1') = G_0(1,1') + G(1,2) \otimes \Sigma(2,3) \otimes G_0(3,1'). \tag{C.2}$$

Although the above two equations are the same in the equilibrium case, they become different in the non-equilibrium case and their difference describes how the system deviates from equilibrium. Labeling the path-dependent times by $(t,-)$ and $(t,+)$ for the time on the forward and backward paths, respectively, the Green's functions can then be decomposed into 2×2 matrices defined in the $(-,+)$ space, which is called the Schwinger-Keldysh space [76, 77]:

$$G = \begin{pmatrix} G_F & G_> \\ G_< & G_{AF} \end{pmatrix}, \tag{C.3}$$

where

$$\begin{aligned} G_>(1,1') &\equiv \langle q(1)\bar{q}(1')\rangle, \\ G_<(1,1') &\equiv -\langle \bar{q}(1')q(1)\rangle, \\ G_F(1,1') &\equiv \theta(t'-t)G_>(1,1') + \theta(t-t')G_<(1,1'), \\ G_{AF}(1,1') &\equiv \theta(t'-t)G_<(1,1') + \theta(t-t')G_>(1,1'), \end{aligned} \tag{C.4}$$

with $1 = (t_1, \mathbf{x}_1, s_1, c_1, \cdots)$, since the additional path information is expressed through the indices in the Schwinger-Keldysh space.

The free Green's function G_0 in Eqs.(C.1) and (C.2) satisfies the relations

$$\hat{G}_0^{-1}(1)G_0(1,1') = G_0(1,1')\hat{G'}_0^{-1}(1') = i\delta(1-1')\tau_3, \tag{C.5}$$

with

$$\hat{G}_0^{-1}(1) \equiv i\partial\!\!\!/_1 - m_0 \quad \text{and} \quad \hat{G'}_0^{-1}(1') \equiv -i\overleftarrow{\partial\!\!\!/}_{1'} - m_0, \tag{C.6}$$

where $\overleftarrow{\partial}$ means that the derivative acts on the left. The third Pauli matrix τ_3 in Eq. (C.5) is defined in the Schwinger-Keldysh space. It appears because t and t' in the θ step functions in G_{AF} have the opposite order compared to those in G_F, resulting in an opposite sign in front of $\delta(t-t')$ after ∂_t or $\partial_{t'}$ acts on the θ functions in G_{AF} compared with that in G_F.

Multiply $\hat{G}_0^{-1}$ and $\hat{G'}_0^{-1}$ on Eq. (C.1) and (C.2) respectively, we have

$$\hat{G}_0^{-1}(1)G(1,1') = i\delta(1-1')\tau_3 + i\tau_3\Sigma(1,2)\otimes G(2,1'), \tag{C.7}$$

$$G(1,1')\hat{G'}_0^{-1}(1') = i\delta(1-1')\tau_3 + iG(1,2)\otimes\Sigma(2,1')\tau_3. \tag{C.8}$$

For the self energy $\Sigma(1,2)$ in above equations, we show explicitly in the following the contribution from the Hartree term for the u quark for illustrations as it is straightforward to extend to the Fock term and other quarks. Including the diagrams shown in Fig. C.2, the Hartree self energy can be expressed as

$$\Sigma^u(1,2) = i\delta(1-2)\begin{pmatrix} V_F^u(1) & 0 \\ 0 & -V_{AF}^u(1) \end{pmatrix}, \tag{C.9}$$

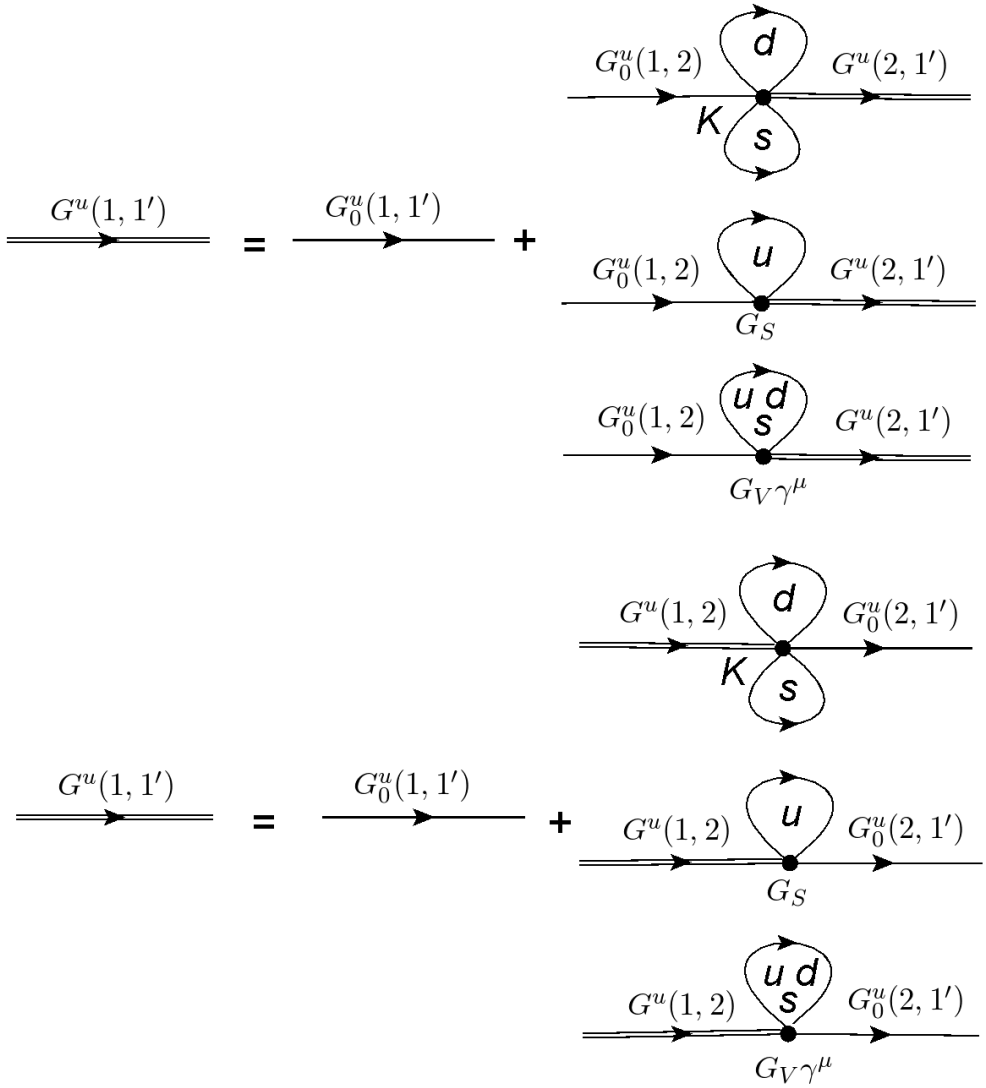

Figure C.2: Dyson equations for the u quark. Only Hartree diagrams are included in the self energy.

where

$$\begin{aligned} V_F^u(1) &= -2G_S \mathrm{Tr} G_F^u(1,1) - 2K \mathrm{Tr} G_F^d(1,1) \mathrm{Tr} G_F^s(1,1) \\ &\quad +2G_V \gamma^\mu \sum_{q=u,d,s} \mathrm{Tr}[G_F^q(1,1)\gamma_\mu], \\ V_{AF}^u(1) &= -2G_S \mathrm{Tr} G_{AF}^u(1,1) - 2K \mathrm{Tr} G_{AF}^d(1,1) \mathrm{Tr} G_{AF}^s(1,1) \\ &\quad +2G_V \gamma^\mu \sum_{q=u,d,s} \mathrm{Tr}[G_{AF}^q(1,1)\gamma_\mu]. \end{aligned} \tag{C.10}$$

We note that the fermion loop contributes an additional minus sign in above equations. The self energy is diagonalized in the Schwinger-Keldysh space, since the off-diagonal terms must connect the two points with different path indices, which is excluded by $\delta(1-2)$. The negative sign in front of V_{AF}^u comes from the backward integration path:

$$\int_C d\tau V(\tau) G = \int_0^\infty dt \left(V_F(t) G_{-\pm} - V_{AF}(t) G_{+\pm} \right), \tag{C.11}$$

where the subscripts + and − labels the components in the Schwinger-Keldysh space.

Introducing the Keldysh Green's Function $G_K = (G_> + G_<)/2 = (G_F + G_{AF})/2$, Eq.(C.7) and Eq.(C.8) then become

$$\begin{aligned} \left(i\not{\partial}_1 - m_0 + V_K^u(1)\right) G_K^u(1,1') &= 0, \\ G_K^u(1,1') \left(-i\overleftarrow{\not{\partial}}_{1'} - m_0 + V_K^u(1')\right) &= 0, \end{aligned} \tag{C.12}$$

where V_K^u can be decomposed into a scalar and a vector part:

$$V_K^u(x) \equiv (V_F^u(x) + V_{AF}^u(x))/2 = V^S(x) + V_\mu^V(x)\gamma^\mu, \tag{C.13}$$

leading thus to an effective or constituent mass for both the u and anti-u quark:

$$M = m_0 - V^S. \tag{C.14}$$

Taking the difference between Eq.(C.12) and Eq.(C.12) results in

$$i\not{\partial}_1 G^u_K(1,1') + iG^u_K(1,1')\overleftarrow{\not{\partial}}_{1'} + V^u_K(1)G^u_K(1,1') - G^u_K(1,1')V^u_K(1') = 0. \tag{C.15}$$

Introducing the mixed or Wigner coordinates $X \equiv (x_1 + x_{1'})/2$ and $x \equiv (x_1 - x_{1'})$, and Fourier transforming all the functions with respect to the relative coordinates x according to

$$\widetilde{G}^u_K(X,p) \equiv \int d^4x e^{ipx} G^u_K(X + \frac{x}{2}, X - \frac{x}{2}), \qquad \widetilde{V}^u_K(p) \equiv \int d^4x e^{ipx} V^u_K(x), \tag{C.16}$$

we can rewrite Eq.(C.15) in the (X,p) representation as

$$\begin{aligned} &\frac{i}{2}\partial_{X^\mu}\{\gamma^\mu, \widetilde{G}^u_K(X,p)\} + [\not{p}, \widetilde{G}^u_K(X,p)] \\ &+ \int \frac{d^4l}{(2\pi)^4}\left(\widetilde{V}^u_K(l)\widetilde{G}^u_K(X, p - \frac{l}{2}) - \widetilde{G}^u_K(X, p + \frac{l}{2})\widetilde{V}^u_K(l)\right) e^{-ilX} = 0. \end{aligned} \tag{C.17}$$

Taylor expanding $\widetilde{G}^u_K(X, p \pm l/2)$ at $l = 0$ and truncating to terms of order $O(l^2)$ as follows:

$$\widetilde{G}^u_K(X, p \pm l/2) \approx \widetilde{G}^u_K(X,p) \pm \frac{l_\mu}{2}\partial_{p_\mu}\widetilde{G}^u_K(X,p) + O(l^2), \tag{C.18}$$

we obtain from Eq. (C.17)

$$\frac{i}{2}\partial_{X^\mu}\{\gamma^\mu, \widetilde{G}^u_K(X,p)\} + [\not{p} + V^u(X), \widetilde{G}^u_K(X,p)] - \frac{i}{2}\{\partial_{X^\mu}V^u(X), \partial_{p_\mu}\widetilde{G}^u_K(X,p)\} = 0. \tag{C.19}$$

To proceed further, we make the quasi-particle approximation by Fourier expanding the quark and antiquark fields as follows:

$$\begin{aligned} q(x) &= \sum_s \int \frac{d^3\mathbf{k}}{2E_{\mathbf{k}}(2\pi)^3} \left(b_s(\mathbf{k}) u_s(\mathbf{k}) e^{-iE^-_{\mathbf{k}_-}t + i\mathbf{k}_-\cdot\mathbf{x}} + (d^\dagger_s(\mathbf{k}) v_s(\mathbf{k}) e^{iE^+_{\mathbf{k}_+}t - i\mathbf{k}_+\cdot\mathbf{x}} \right), \\ \bar{q}(x) &= \sum_s \int \frac{d^3\mathbf{k}}{2E_{\mathbf{k}}(2\pi)^3} \left(b^\dagger_s(\mathbf{k}) \bar{u}_s(\mathbf{k}) e^{iE^-_{\mathbf{k}_-}t - i\mathbf{k}_-\cdot\mathbf{x}} + (d_s(\mathbf{k}) \bar{v}_s(\mathbf{k}) e^{-iE^+_{\mathbf{k}_+}t + i\mathbf{k}_+\cdot\mathbf{x}} \right), \end{aligned} \tag{C.20}$$

where $\mathbf{k}_\pm \equiv \mathbf{k} \pm \mathbf{V}^V$ and $E^\pm_{\mathbf{k}} \equiv E_{\mathbf{k}} \pm V^V_0$, b and d are the annihilation operators of the dressed (or constituent) quark and anti-quark, respectively, and u and v are the corresponding Dirac spinors. The quark Green's function is then

$$\begin{aligned} &\widetilde{G}_>(X,p) = \int d^4x e^{ipx} \langle q(X+\frac{x}{2}) \bar{q}(X-\frac{x}{2}) \rangle \\ &= \sum_{s,s'} \int \frac{d^3\mathbf{k}}{2E_{\mathbf{k}}(2\pi)^3} \frac{d^3\mathbf{k}'}{2E_{\mathbf{k}'}(2\pi)^3} \langle b_s(\mathbf{k}) b^\dagger_{s'}(\mathbf{k}') \rangle u_s(\mathbf{k}) \bar{u}_{s\prime}(\mathbf{k}') e^{-i(E_{\mathbf{k}_-} - E_{\mathbf{k}'_-})T} e^{i(\mathbf{k}-\mathbf{k}')\cdot\mathbf{X}} \\ &\quad \times \int d^4x e^{i(2p^0 + 2V^V_0 - E_{\mathbf{k}_-} - E_{\mathbf{k}'_-})x^0/2} e^{i(-2\mathbf{p} + \mathbf{k}_- + \mathbf{k}'_-)\cdot\mathbf{x}/2} \\ &\quad + \sum_{s,s'} \int \frac{d^3\mathbf{k}}{2E_{\mathbf{k}}(2\pi)^3} \frac{d^3\mathbf{k}'}{2E_{\mathbf{k}'}(2\pi)^3} \langle d^\dagger_s(\mathbf{k}) d_{s'}(\mathbf{k}') \rangle v_s(\mathbf{k}) \bar{v}_{s'}(\mathbf{k}') e^{-i(E_{\mathbf{k}_+} - E_{\mathbf{k}'_+})T} e^{i(\mathbf{k}-\mathbf{k}')\cdot\mathbf{X}} \\ &\quad \times \int d^4x e^{i(2p^0 + 2V^V_0 + E_{\mathbf{k}_+} + E_{\mathbf{k}'_+})x^0/2} e^{i(-2\mathbf{p} - \mathbf{k}_+ - \mathbf{k}'_+)\cdot\mathbf{x}/2} \\ &= \sum_{s,s'} \int \frac{d^3\mathbf{k}}{2E_{\mathbf{k}}(2\pi)^2} \frac{1}{2E_{\mathbf{2p}^+ - \mathbf{k}}} \langle b_s(\mathbf{k}) b^\dagger_{s'}(\mathbf{2p}^+ - \mathbf{k}) \rangle u_s(\mathbf{k}) \bar{u}_{s'}(\mathbf{2p}^+ - \mathbf{k}) \\ &\quad \times e^{-i(E_{\mathbf{k}_-} - E_{\mathbf{2p}-\mathbf{k}_-})T} e^{2i(\mathbf{k}-\mathbf{p}^+)\cdot\mathbf{X}} \delta(p^0 + V^V_0 - E_{\mathbf{k}_-}/2 - E_{\mathbf{2p}-\mathbf{k}_-}/2) \\ &\quad + \sum_{s,s'} \int \frac{d^3\mathbf{k}}{2E_{\mathbf{k}}(2\pi)^2} \frac{1}{2E_{-\mathbf{2p}^+ - \mathbf{k}}} \langle d^\dagger_s(\mathbf{k}) d_{s'}(-\mathbf{2p}^+ - \mathbf{k}) \rangle v_s(\mathbf{k}) \bar{v}_{s'}(-\mathbf{2p}^+ - \mathbf{k}) \\ &\quad \times e^{-i(E_{\mathbf{k}_+} - E_{-\mathbf{2p}-\mathbf{k}_+})T} e^{2i(\mathbf{k}+\mathbf{p}^+)\cdot\mathbf{X}} \delta(p^0 + V^V_0 + E_{\mathbf{k}_+}/2 + E_{-\mathbf{2p}-\mathbf{k}_+}/2), \end{aligned} \tag{C.21}$$

where $\mathbf{p}^{\pm} \equiv \mathbf{p} \pm \mathbf{V}^V$. In terms of the quark and antiquark distributions,

$$\begin{aligned}
\langle b_s(\mathbf{k}) b^\dagger_{s'}(\mathbf{2p}^+ - \mathbf{k})\rangle &= (2\pi)^3 2E_{\mathbf{p}^+}\delta^3(2\mathbf{p}^+ - 2\mathbf{k})\delta_{ss'}(1 - f_q(X,\mathbf{p})), \\
\langle d^\dagger_s(\mathbf{k}) d_{s'}(-\mathbf{2p}^+ - \mathbf{k})\rangle &= (2\pi)^3 2E_{-\mathbf{p}^+}\delta^3(2\mathbf{p}^+ + 2\mathbf{k})\delta_{ss'} f_{\bar{q}}(X,-\mathbf{p}),
\end{aligned} \tag{C.22}$$

the Green's function $\widetilde{G}_>(X,p)$ in Eq.(C.21) can be written in a simple form as

$$\begin{aligned}
\widetilde{G}_>(X,p) &= \frac{\pi}{E_{\mathbf{p}^+}}(1 - f_q(X,\mathbf{p}))\sum_s u_s(\mathbf{p}^+)\bar{u}_s(\mathbf{p}^+)\delta(p^0 + V_0^V - E_{\mathbf{p}^+}) \\
&\quad + \frac{\pi}{E_{-\mathbf{p}^+}} f_{\bar{q}}(X,-\mathbf{p})\sum_s v_s(-\mathbf{p}^+)\bar{v}_s(-\mathbf{p}^+)\delta(p^0 + V_0^V + E_{-\mathbf{p}^+}) \\
&= \pi\Big(\gamma^0 + \frac{p_i^+\gamma^i}{E_{\mathbf{p}^+}} + \frac{M}{E_{\mathbf{p}^+}}\Big)\delta(p^0 + V_0^V - E_{\mathbf{p}^+})(1 - f_q(X,\mathbf{p})) \\
&\quad + \pi\Big(\gamma^0 - \frac{p_i^+\gamma^i}{E_{\mathbf{p}^+}} - \frac{M}{E_{\mathbf{p}^+}}\Big)\delta(p^0 + V_0^V + E_{-\mathbf{p}^+}) f_{\bar{q}}(X,-\mathbf{p}).
\end{aligned} \tag{C.23}$$

Similarly, we have for other Green's fucntions

$$\begin{aligned}
\widetilde{G}_<(X,p) &= -\pi\Big(\gamma^0 + \frac{p_i^+\gamma^i}{E_{\mathbf{p}^+}} + \frac{M}{E_{\mathbf{p}^+}}\Big)\delta(p^0 + V_0^V - E_{\mathbf{p}^+}) f_q(X,\mathbf{p}) \\
&\quad -\pi\Big(\gamma^0 - \frac{p_i^+\gamma^i}{E_{\mathbf{p}^+}} - \frac{M}{E_{\mathbf{p}^+}}\Big)\delta(p^0 + V_0^V + E_{-\mathbf{p}^+})(1 - f_{\bar{q}}(X,-\mathbf{p})),
\end{aligned} \tag{C.24}$$

and

$$\begin{aligned}
\widetilde{G}_K(X,p) &= \pi\Big(\gamma^0 + \frac{p_i^+\gamma^i}{E_{\mathbf{p}^+}} + \frac{M}{E_{\mathbf{p}^+}}\Big)\delta(p^0 + V_0^V - E_{\mathbf{p}^+})(\frac{1}{2} - f_q(X,\mathbf{p})) \\
&\quad -\pi\Big(\gamma^0 - \frac{p_i^+\gamma^i}{E_{\mathbf{p}^+}} - \frac{M}{E_{\mathbf{p}^+}}\Big)\delta(p^0 + V_0^V + E_{-\mathbf{p}^+})(\frac{1}{2} - f_{\bar{q}}(X,-\mathbf{p})).
\end{aligned} \tag{C.25}$$

Substituting $\widetilde{G}^u_K$ in Eq. (C.19), taking the trace, and integrating over p^0 from 0

to infinity, we obtain the following Vlasov equation for the u quark:

$$\partial_{X^0} f_u(X,\mathbf{p}) + \frac{p^{i+}}{E_{\mathbf{p}^+}} \partial_{X^i} f_u(X,\mathbf{p}) - \partial_{X^i} V^S(X) \frac{M}{E_{\mathbf{p}^+}} \partial_{p_i} f_u(X,\mathbf{p})$$
$$-\partial_{X^i} V_0^V(X) \partial_{p_i} f_u(X,\mathbf{p}) - \partial_{X^i} V_j^V(X) \frac{p^{j+}}{E_{\mathbf{p}^+}} \partial_{p_i} f_u(X,\mathbf{p}) = 0. \qquad \text{(C.26)}$$

If the integration is over p^0 from $-\infty$ to 0, we then obtain the following Vlasov equation for the anti-u quark:

$$\partial_{X^0} f_{\bar{u}}(X,\mathbf{p}) + \frac{p^{i-}}{E_{\mathbf{p}^-}} \partial_{X^i} f_{\bar{u}}(X,\mathbf{p}) - \partial_{X^i} V^S(X) \frac{M}{E_{\mathbf{p}^-}} \partial_{p_i} f_{\bar{u}}(X,\mathbf{p})$$
$$+\partial_{X^i} V_0^V(X) \partial_{p_i} f_{\bar{u}}(X,\mathbf{p}) + \partial_{X^i} V_j^V(X) \frac{p^{j-}}{E_{\mathbf{p}^-}} \partial_{p_i} f_{\bar{u}}(X,\mathbf{p}) = 0. \qquad \text{(C.27)}$$

The scalar mean field V^S and the vector mean field V^V in the above equation are given by

$$\begin{aligned} V^S(x) &= -2G_S \mathrm{Tr} G_K^u(x,x) - K(\mathrm{Tr} G_>^d(x,x)\mathrm{Tr} G_>^s(x,x) + \mathrm{Tr} G_<^d(x,x)\mathrm{Tr} G_<^s(x,x)), \\ V_\mu^V(x) &= 2G_V \sum_{q=u,d,s} \mathrm{Tr}[G_K^q(x,x)\gamma_\mu], \end{aligned} \qquad \text{(C.28)}$$

where

$$\begin{aligned} \mathrm{tr} G_K^q(x,x) &= \int \frac{d^4p}{(2\pi)^4} \mathrm{tr} \widetilde{G}_K^q(x,p) = 2\int \frac{d^3\mathbf{p}}{(2\pi)^3} \frac{M}{E_\mathbf{p}} \left(1 - f_q(x,\mathbf{p}) - f_{\bar{q}}(x,\mathbf{p})\right) \\ &= \mathrm{tr} G_>^q(x,x) = \mathrm{tr} G_<^q(x,x), \\ \mathrm{tr}[G_K^q(x,x)\gamma_0] &= \int \frac{d^4p}{(2\pi)^4} \mathrm{tr}[\widetilde{G}_K^q(x,p)\gamma_0] = -2\int \frac{d^3\mathbf{p}}{(2\pi)^3} \left(f_q(x,\mathbf{p}) - f_{\bar{q}}(x,\mathbf{p})\right), \\ \mathrm{tr}[G_K^q(x,x)\gamma_i] &= \int \frac{d^4p}{(2\pi)^4} \mathrm{tr}[\widetilde{G}_K^q(x,p)\gamma_i] = -2\int \frac{d^3\mathbf{p}}{(2\pi)^3} \frac{p_i}{E_\mathbf{p}} \left(f_q(x,\mathbf{p}) - f_{\bar{q}}(x,\mathbf{p})\right), \end{aligned} \qquad \text{(C.29)}$$

can be interpreted as the negative quark condensate $-\langle\bar{q}q\rangle$, density ρ_0, and current density $\mathbf{j}$, respectively, and the factor 2 in above equations is due to the spin degeneracy of quark and antiquark. The scalar and vector mean fields can thus be written as

$$\begin{aligned} V^S(x) &= 2G_S\langle\bar{u}u\rangle + 2K\langle\bar{d}d\rangle\langle\bar{s}s\rangle, \\ V^V_\mu(x) &= -2G_V j_\mu. \end{aligned} \tag{C.30}$$

Similar derivations can be used for d and s quarks and their antiquarks, and their transport equations are similar to those for the u and $\bar{u}$ quarks.

C.2 Test particle method on solving the Boltzmann equations

For large amplitude density fluctuations or their long time behavior, one needs to solve the time evolution of the density matrix via either the time-dependent Hatree-Fock (TDHF) or the Dyson-Schwinger equation. In this work, we solve instead the classical Boltzmann equation by using the test particle method. In this approach, the one particle phase-space distribution function $f(\mathbf{x},\mathbf{p})$ is replaced by N classical particles, i.e., $f(\mathbf{x},\mathbf{p},t) = \sum_i \delta(\mathbf{x}-\mathbf{x}_i(t))\delta(\mathbf{p}-\mathbf{p}_i(t))/N$ [78]. Since

$$\partial_t f(\mathbf{x},\mathbf{p},t) = -\sum_{i=1}^{N}(\dot{\mathbf{x}}_i\cdot\nabla_{\mathbf{x}} + \dot{\mathbf{p}}_i\cdot\nabla_{\mathbf{p}})f(\mathbf{x},\mathbf{p},t), \tag{C.31}$$

we obtain from Eqs. (C.26) and (C.27)

$$\begin{aligned} 0 &= \sum_{i=1}^{N}\Big(\Big(-\dot{\mathbf{x}}_i + \frac{\mathbf{p}_i^+}{E_{\mathbf{p}_i^+}}\Big)\cdot\nabla_{\mathbf{x}} + \Big(-\dot{\mathbf{p}}_i + \nabla_{\mathbf{x}}V^S(\mathbf{x}_i)\frac{M}{E_{\mathbf{p}_i^+}} \\ &\quad +\nabla_{\mathbf{x}}V_0^V(\mathbf{x}_i) + \nabla_{\mathbf{x}}V_j^V(\mathbf{x}_i)\frac{p_i^{j+}}{E_{\mathbf{p}_i^+}}\Big)\cdot\nabla_{\mathbf{p}}\Big) \\ &\quad \frac{1}{N}\delta(\mathbf{x}-\mathbf{x}_i(t))\delta(\mathbf{p}-\mathbf{p}_i(t)) \end{aligned} \tag{C.32}$$

for quarks, and

$$
\begin{aligned}
0 \;=\; & \sum_{i=1}^{N} \Big(\Big(-\dot{\mathbf{x}}_i + \frac{\mathbf{p}_i^-}{E_{\mathbf{p}_i^-}} \Big) \cdot \nabla_{\mathbf{x}} + \Big(-\dot{\mathbf{p}}_i + \nabla_{\mathbf{x}} V^S(\mathbf{x}_i) \frac{M}{E_{\mathbf{p}_i^-}} \\
& - \nabla_{\mathbf{x}} V_0^V(\mathbf{x}_i) - \nabla_{\mathbf{x}} V_j^V(\mathbf{x}_i) \frac{p_i^{j-}}{E_{\mathbf{p}_i^-}} \Big) \cdot \nabla_{\mathbf{p}} \Big) \\
& \frac{1}{N} \delta(\mathbf{x} - \mathbf{x}_i(t)) \delta(\mathbf{p} - \mathbf{p}_i(t))
\end{aligned} \tag{C.33}
$$

for antiquarks, where the index i denotes different particles, while the index j refers to the spatial components of the vector mean field $\mathbf{V}$ and momentum $\mathbf{p}$. The equations of motion are thus

$$
\begin{aligned}
\dot{\mathbf{x}}_i &= \frac{\mathbf{p}_i^+}{E_{\mathbf{p}_i^+}}, \\
\dot{\mathbf{p}}_i &= \nabla V^S(\mathbf{x}_i) \frac{M}{E_{\mathbf{p}_i^+}} + \nabla V_0^V(\mathbf{x}_i) + \nabla V_j^V(\mathbf{x}_i) \frac{p_i^{j+}}{E_{\mathbf{p}_i^+}}
\end{aligned} \tag{C.34}
$$

for quarks and

$$
\begin{aligned}
\dot{\mathbf{x}}_i &= \frac{\mathbf{p}_i^-}{E_{\mathbf{p}_i^-}}, \\
\dot{\mathbf{p}}_i &= \nabla V^S(\mathbf{x}_i) \frac{M}{E_{\mathbf{p}_i^-}} - \nabla V_0^V(\mathbf{x}_i) - \nabla V_j^V(\mathbf{x}_i) \frac{p_i^{j-}}{E_{\mathbf{p}_i^-}}
\end{aligned} \tag{C.35}
$$

for anti-quarks. The momentum part of Eqs. (C.34) and (C.35) can be rewritten as

$$
\dot{\mathbf{p}}^{\pm} = \nabla V^S(\mathbf{x}) \frac{M}{E_{\mathbf{p}}} \mp \dot{\mathbf{x}} \times \mathbf{B} \pm \mathbf{E}, \tag{C.36}
$$

where $\mathbf{B} = \nabla \times \mathbf{V}^V$ is the strong magnetic field and $\mathbf{E} = \partial_t \mathbf{V}^V + \nabla V^S$ is the strong electric field, and in the$\mp$, the $-$ sign is for quark and the $+$ sign is for antiquark.

For the mean-field potentials in the above equations of motion, they are functions

of densities and are calculated from the latter by dividing the space into 3-dimensional grids and then counting the number of particles in a grid. For example, the scalar potential $V_i^S = 2G_S\langle\bar{q}q\rangle_i + 2K\langle\bar{q}q\rangle_l\langle\bar{q}q\rangle_k$ is calculated by summing up the ratio M_i/E_i of particles in each grid and the vector potential $V^{V\mu}(x) = -2G_V j^\mu$ is calculated from the sum of bp_i^μ/E_i of these particles with their baryon charge denoted by b. In the above, the subscripts i, l, and k with $i \neq l \neq k$ label the flavors. Since the quark mass is given by $M = m_0 - V^S$, it is determined self-consistently. To ensure the accuracy in the calculation of densities, many test particles are usually used. However, the finite grid size used in the calculation leads to a grid effect for zero-range interactions as in the NJL and PNJL model. In Appendix D, we discuss this effect and show that it suppresses the spinodal instability compared to that based on the analytic solution of the linearized Vlasov equation.

For the collisional terms in the transport model, they are usually treated by using the geometric method based on the two conditions of whether the impact parameter between two colliding particles is smaller than $\sqrt{\sigma/\pi}$, where σ is the total scattering cross section of the two particles, and if the two colliding particles pass through each other at the next time step in the evolution of the system. In Appendix D, we describe in detail the treatment of the collision term, including the methods used to ensure Lorentz invariant and to take into account the Pauli-blocking effect.

APPENDIX D

NUMERICAL IMPLEMENTATIONS OF THE TRANSPORT MODEL

D.1 Finite grid size effects

Counting partons in a grid of finite size in evaluating the mean fields effectively allows the partons in the grid interact with each other, thus modifying the contact interactions in the NJL model to finite-range ones. To study this effect, we need to calculate the probability for two partons in the same grid to have a separation $\Delta\mathbf{x}$. Given a parton located at $x \in [0, a]$ in a 1-dimensional grid $[0, a]$, the probability to find another parton located at $x + \Delta x$ in the same grid is

$$P(\Delta x) = \frac{1}{a}\int dx\theta(x)\theta(a-x)\theta(x+\Delta x)\theta(a-\Delta x-x) = \mathrm{tri}\left(\frac{\Delta x}{a}\right), \tag{D.1}$$

where

$$\mathrm{tri}(x) \stackrel{\Delta}{=} \max(0, 1-|x|). \tag{D.2}$$

The above expression can be straightforwardly generalized to the 3-dimensional case to give

$$P(\Delta\mathbf{x}) = \prod_i \mathrm{tri}\left(\frac{\Delta x^i}{a^i}\right), \tag{D.3}$$

where $\{a^1, a^2, a^3\}$ is the grid length. The interaction between the two partons at $\mathbf{x}$ and $\mathbf{y}$ is then replaced by

$$\begin{aligned} G_S\delta^3(\mathbf{x}-\mathbf{y}) &\rightarrow \frac{G_S}{\prod_i a^i}\prod_i \mathrm{tri}\left(\frac{x^i-y^i}{a_i}\right), \\ K\delta^3(\mathbf{x}-\mathbf{y}) &\rightarrow \frac{K}{\prod_i a^i}\prod_i \mathrm{tri}\left(\frac{x^i-y^i}{a_i}\right). \end{aligned} \tag{D.4}$$

Transforming Eq. (D.4) from **x**-space to **k**-space gives

$$\begin{aligned} G_S \to \tilde{G}_S &= G_S \prod_i \frac{2\cos(a^i k_i) - 2}{a^i k_i}, \\ K \to \tilde{K} &= K \prod_i \frac{2\cos(a^i k_i) - 2}{a^i k_i}. \end{aligned} \tag{D.5}$$

Note that in the limit that $a^i k_i \to 0$ for all the i, $\tilde{G}_S \to G_S$ and $\tilde{K} \to K$, which means the modification does not affect the long wavelength modes. Replacing G_S

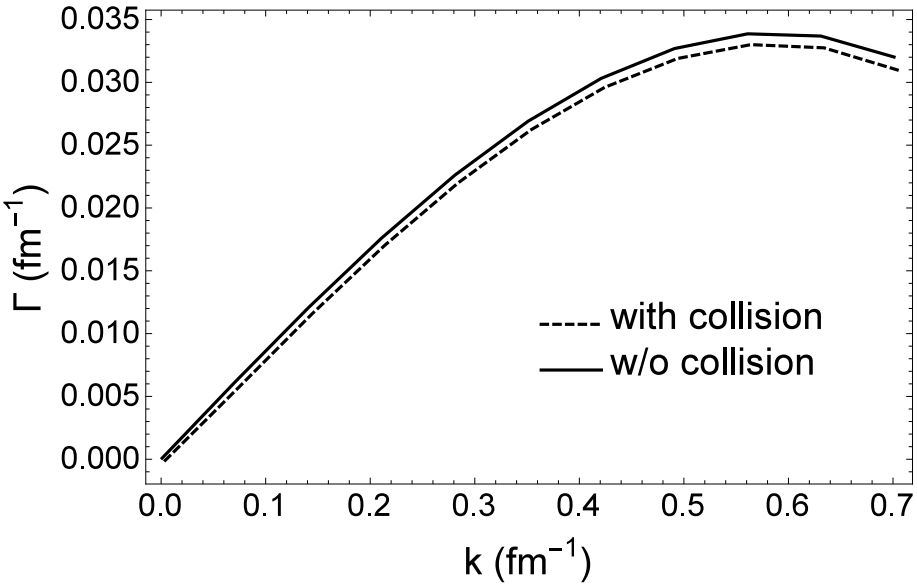

Figure D.1: Growth rate of unstable modes in the presence of finite grid effect with (dashed line) and without (solid line) the collisional term for isotropic parton scatting cross section of 3 mb in a quark matter of net quark density 0.7 fm^{-3} and temperature 45 MeV. The grid size is taken to be 2/3 fm.

and K in Eq.(3.51) with $\tilde{G}_S$ and $\tilde{K}$, respectively, and solving the resulting equation, we obtain the modified dispersion relation, and they are shown in Fig. D.1 for a grid size $a^i = 2/3$ fm. As expected, the growth rate Γ_k is not much affected in the small k

region but is significantly suppressed in the large k region. The finite grid size effect is thus opposite to that due to collisions but similar to the quantum effect shown in the Section 3. Using a finite grid size essentially allows partons to interact at finite separation, resulting in an effective finite-range interaction.

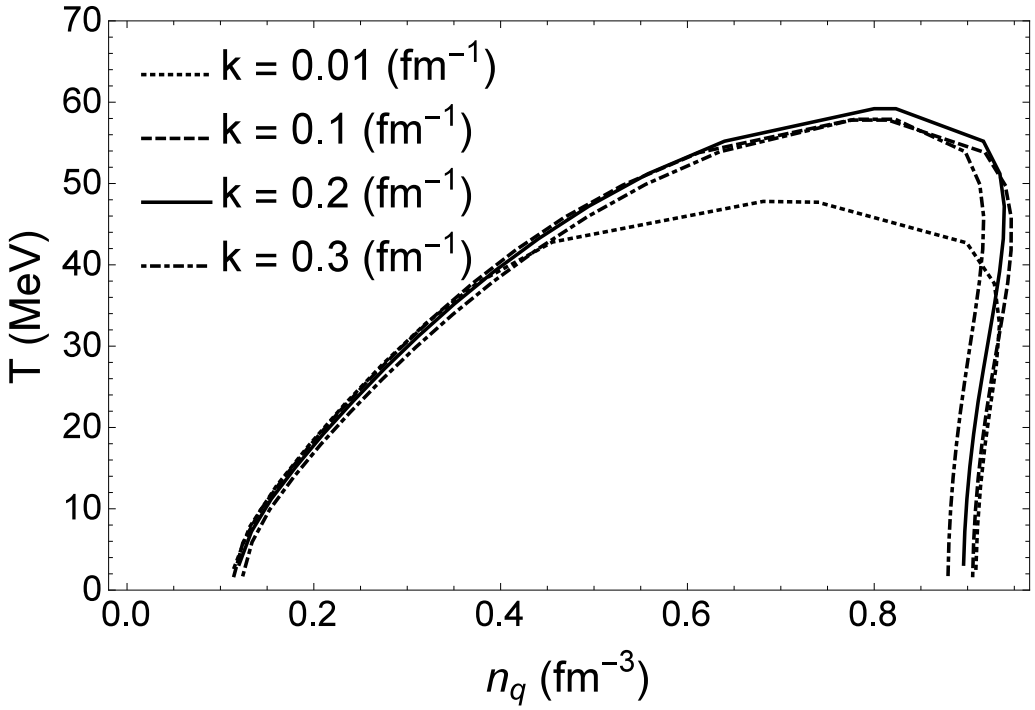

Figure D.2: Spinodal instability boundary for different values of unstable mode wave number after including both the collisional effect using an isotropic cross section of 3 mb and the effect due to a finite grid size of 2/3 fm.

Since unstable modes of long wavelength are affected by the collisional effect and those of shorter wavelength are affected by the finite grid size effect, including these effects makes the spinodal instability region of all unstable modes smaller than that obtained based on the consideration of thermodynamic instability. In Fig. D.2, we show the spinodal instability boundaries for unstable modes of wave numbers

$k = 0.01$ fm^{-1}, $k = 0.1$ fm^{-1}, $k = 0.2$ fm^{-1}, and $k = 0.3$ fm^{-1}, given by the dotted, dashed, solid and dot-dashed lines, respectively. The critical temperature T_c reaches a maximum value of about 60 MeV for $k = 0.2$ fm^{-1} and becomes smaller for unstable modes with either larger or smaller k, compared to the critical temperature of 70 MeV in the thermodynamic limit.

D.2 Two-body collisions and the Pauli effect

Two issues need to be considered in the treatment of the collision term in the Boltzmann equations. First, cross sections are not Lorentz invariant quantities. Since

$$d\sigma = \frac{1}{4E_A E_B |\mathbf{v}_A - \mathbf{v}_B|} \left(\prod_f \frac{d^3\mathbf{p}_f}{2E_f(2\pi)^3} \right) |\mathcal{M}(p_A, p_B \to \{p_f\})|^2 (2\pi)^4 \delta^4(p_A + p_B - \sum p_f), \tag{D.6}$$

with A and B denoting two colliding particles, and f denoting the final states, the cross section transforms as $(E_A E_B |\mathbf{v}_A - \mathbf{v}_B|)^{-1}$. For $\mathbf{p_A}$ and $\mathbf{p_B}$ parallel to each other, such as in their center of mass frame, boosting along the direction of $\mathbf{p_A}$ or $\mathbf{p_B}$ does not change the cross section. However, the momenta of two colliding particles in the lab frame are generally not parallel, we need to determine their scattering cross section from that in their center of mass frame according to

$$\sigma_{\text{lab}} = \sigma_{\text{CM}} \frac{\sqrt{(s - (m_A + m_B)^2)(s - (m_A - m_B)^2)}}{2E_A E_B |\mathbf{v}_A - \mathbf{v}_B|}, \tag{D.7}$$

where $s = (p_A + p_B)^2$ is the square of their invariant mass.

Another effect need to be taken into account in the transport model is the Pauli blocking effect, which prevents two fermions from occupying the same quantum state. Here, we estimate the importance of this effect, introduce an algorithm to include this effect, and check the reliability of the algorithm.

The collision rate of a gas of identical particles in a fixed volume is given by

$$R = \frac{1}{2}\int \frac{d^3\mathbf{p}_1}{2E_1}\frac{d^3\mathbf{p}_2}{2E_2}\frac{d^3\mathbf{p}_3}{2E_3}\frac{d^3\mathbf{p}_4}{2E_4}\frac{1}{(2\pi)^8}|\mathcal{M}|^2\delta^4(p_1+p_2-p_3-p_4)f_1f_2(1-f_3)(1-f_4), \quad \text{(D.8)}$$

where the factor 1/2 is for collisions of identical particles. In terms of the center of mass and relative momenta of initial particles $\mathbf{P}$ and $\mathbf{p}$ as well as those of final particles $\mathbf{P}'$ and $\mathbf{p}'$, defined by $\mathbf{p}_1 = \mathbf{P} + \mathbf{p}/2$, $\mathbf{p}_2 = \mathbf{P} - \mathbf{p}/2$, $\mathbf{p}_3 = \mathbf{P}' + \mathbf{p}'/2$, $\mathbf{p}_4 = \mathbf{P}' - \mathbf{p}'/2$ and using the transformation measures $d^3\mathbf{p}_1 d^3\mathbf{p}_2 = d^3\mathbf{P}d^3\mathbf{p}$ and $d^3\mathbf{p}_3 d^3\mathbf{p}_4 = d^3\mathbf{P}'d^3\mathbf{p}'$, the integral over $\mathbf{P}'$ can be eliminated by the δ function,

$$\delta^3(\mathbf{p}_1 + \mathbf{p}_2 - \mathbf{p}_3 - \mathbf{p}_4) = \delta^3(2\mathbf{P} - 2\mathbf{P}') = \delta^3(\mathbf{P} - \mathbf{P}')/8. \quad \text{(D.9)}$$

Expressing the energies in terms of $\mathbf{P}$, $\mathbf{p}$, and $\mathbf{p}'$ according to

$$\begin{aligned} E_1 &= \sqrt{P^2 + p^2/4 + xPp}, \\ E_2 &= \sqrt{P^2 + p^2/4 - xPp}, \\ E_3 &= \sqrt{P^2 + p'^2/4 + x'Pp}, \\ E_4 &= \sqrt{P^2 + p'^2/4 - x'Pp'}, \end{aligned} \quad \text{(D.10)}$$

where P, p, and p' denoting the magnitude of $\mathbf{P}$, $\mathbf{p}$, and $\mathbf{p}'$, respectively, and x and x' denoting $\cos(\mathbf{P}, \mathbf{p})$ and $\cos(\mathbf{P}, \mathbf{p}')$, respectively, the collision rate can be rewritten as

$$R = \frac{1}{2}\int dPP^2\frac{dpp^2dxd\phi}{4E_1E_2}\frac{dp'p'^2dx'd\phi'}{4E_3E_4}\frac{4\pi}{8(2\pi)^8}|\mathcal{M}|^2\delta(E_1+E_2-E_3-E_4)f_1f_2(1-f_3)(1-f_4). \quad \text{(D.11)}$$

For scatterings that are isotropic, the invariant amplitude $\mathcal{M}$ is independent of x, ϕ,

x', and ϕ', and the collision rate can be further simplified to

$$R = \frac{1}{2}\int dPP^2 \frac{dpp^2dx}{4E_1E_2}\frac{dp'p'^2dx'}{4E_3E_4}\frac{2}{8(2\pi)^5}|\mathcal{M}|^2\delta(E_1+E_2-E_3-E_4)f_1f_2(1-f_3)(1-f_4). \tag{D.12}$$

The remaining Dirac δ function can be written as

$$\delta(E_1+E_2-E_3-E_4) = \int dE\delta(E_1+E_2-E)\delta(E-E_3-E_4), \tag{D.13}$$

with

$$E = |\mathbf{p}_1| + |\mathbf{p}_2| > |\mathbf{p}_1+\mathbf{p}_2| = 2P. \tag{D.14}$$

Since

$$\begin{aligned}
\delta(E_1+E_2-E) &= \delta\left(p - E\sqrt{\frac{E^2-4P^2}{E^2-4x^2P^2}}\right)\frac{1}{|\partial(E_1+E_2-E)/\partial p|} \\
&= \delta\left(p - E\sqrt{\frac{E^2-4P^2}{E^2-4x^2P^2}}\right)\frac{4E_1E_2E}{p(E^2-4x^2P^2)}, \\
\delta(E_3+E_4-E) &= \delta\left(p - E\sqrt{\frac{E^2-4P^2}{E^2-4x'^2P^2}}\right)\frac{4E_3E_4E}{p(E^2-4x'^2P^2)},
\end{aligned} \tag{D.15}$$

we can eliminate the integrations over p and p' and obtain

$$R = \frac{1}{2}\int dEdPdxdx'\frac{2}{8(2\pi)^5}|\mathcal{M}|^2\frac{E^4P^2s}{(E^2-4x^2P^2)^{3/2}(E^2-4x'^2P^2)^{3/2}}f_1f_2(1-f_3)(1-f_4), \tag{D.16}$$

where $s \equiv (p_1+p_2)^2 = (E^2-4P^2)$. The invariant scattering amplitude $\mathcal{M}$ in the above equation can be expressed in terms of the cross section via the following well known relation:

$$|\mathcal{M}|^2 = 64\pi^2 s\frac{d\sigma}{d\Omega_{\rm CM}} = 16\pi s\sigma_{\rm CM}, \tag{D.17}$$

where $\sigma_{\rm CM}$ is the cross section evaluated in the center of mass frame and the second equality follows from the assumption that the scattering cross section is isotropic. The collision rate is therefore given by

$$R = \frac{1}{2}\int dEdPdxdx' \frac{2}{(2\pi)^4}\sigma_{CM}\frac{E^4P^2(E^2-4P^2)^2}{(E^2-4x^2P^2)^{3/2}(E^2-4x'^2P^2)^{3/2}} f_1 f_2(1-f_3)(1-f_4). \tag{D.18}$$

For systems in thermal equilibrium, all fs in Eq. (D.18) are Fermi-Dirac distribution functions, which have the property

$$(1-f_3)(1-f_4) = f_3 f_4 e^{E/T} z^{-2}, \tag{D.19}$$

with $z = e^{\mu/T}$. Defining the scaled energy $\xi = E/T$ and momentum $\eta = 2P/T$, Eq. (D.18) can be rewritten as

$$R = \frac{1}{2}\frac{T^6}{4(2\pi)^4}\int_0^\infty d\eta \int_\eta^\infty d\xi \sigma_{CM}\eta^2\xi^4(\xi^2-\eta^2)^2 F^2(\xi,\eta)e^\xi z^{-2}, \tag{D.20}$$

where

$$F(\xi,\eta) = \int_{-1}^{1} dx (\xi^2 - x^2\eta^2)^{-3/2} f(\xi,\eta,x) f(\xi,\eta,-x), \tag{D.21}$$

and

$$f(\xi,\eta,x) = \frac{1}{z^{-1}\exp(\frac{1}{2}(\xi + x\eta\sqrt{\frac{\xi^2-\eta^2}{\xi^2-x^2\eta^2}})) + 1}. \tag{D.22}$$

In terms of the particle density

$$n = -\frac{T^3}{\pi^2}\mathrm{Li}_3(-z), \tag{D.23}$$

where Li_3 is the polynomial logarithm function, the collision rate can be simply

expressed as

$$R = \frac{1}{2}\langle\sigma v\rangle_F n^2, \tag{D.24}$$

with

$$\langle\sigma v\rangle_F = \frac{1}{64\mathrm{Li}_3^2(-z)}\int_0^\infty d\eta\int_\eta^\infty d\xi\sigma_{\mathrm{CM}}\eta^2\xi^4(\xi^2-\eta^2)^2F^2(\xi,\eta)e^\xi z^{-2}. \tag{D.25}$$

We note that the cross section σ can be taken out of the integral if it has a constant value.

For comparison, we have also considered the collision rate of classical particles, which are not affected by the Pauli blocking effect. The rate can be obtained from Eq. (D.18) by dropping the factor $(1-f_3)(1-f_4)$ and using the Boltzmann distribution for f_1 and f_2, i.e., $f_1f_2 = z^2e^{-E/T}$. In this case, the collision rate becomes

$$R_B = \frac{1}{2}\int dEdPdxdx'\frac{2}{(2\pi)^4}\sigma_{\mathrm{CM}}\frac{E^4P^2(E^2-4P^2)^2}{(E^2-4x^2P^2)^{3/2}(E^2-4x'^2P^2)^{3/2}}e^{-E/T}z^2. \tag{D.26}$$

Carrying out the integration over x and x' using

$$\int_{-1}^1 dx\frac{1}{(E^2-4x^2P^2)^{3/2}} = \frac{2}{\sqrt{s}E^2}, \tag{D.27}$$

we find

$$R_B = \frac{1}{2}\int dEdP\frac{8}{(2\pi)^4}\sigma_{\mathrm{CM}}P^2(E^2-4P^2)e^{-E/T}z^2. \tag{D.28}$$

Changing variables according to $E = \sqrt{s}\cosh y$, $2P = \sqrt{s}\sinh y$, where y is the rapidity, and using the relation $dEdP = \sqrt{s}/2d\sqrt{s}dy$, the collision rate becomes

$$R_B = \frac{1}{2}\frac{z^2}{(2\pi)^4}\int d\sqrt{s}dy\sigma s^{5/2}\sinh^2 y e^{-\sqrt{s}\cosh y/T}$$

$$= \frac{1}{2}\frac{z^2T}{(2\pi)^4}\int d\sqrt{s}\sigma s^2 K_1(\sqrt{s}/T)$$
$$= \frac{1}{2}\frac{z^2T^6}{(2\pi)^4}\int dm\sigma m^4 K_1(m), \tag{D.29}$$

where $m = \sqrt{s}/T$ is the reduced energy. For isotropic and constant scattering cross section, i.e., $\sigma_{\rm CM}$ has no y dependence, and using the density of classical particles

$$n_B = \frac{zT^3}{\pi^2}, \tag{D.30}$$

the collision rate can be further simplified to

$$R_B = \sigma_{\rm CM} n_B^2 \frac{1}{32}\int dm m^4 K_1(m) = \frac{1}{2}\sigma_{\rm CM} n_B^2. \tag{D.31}$$

Apparently, we have $\langle\sigma v\rangle = \sigma_{\rm CM}$ in this case. In Fig. D.3, we shown $\langle\sigma v\rangle$ as a

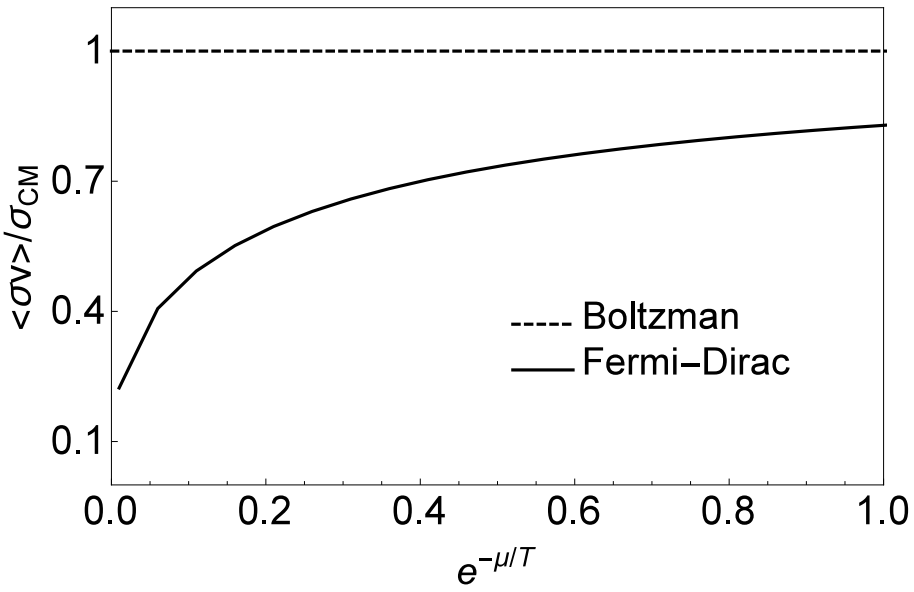

Figure D.3: Collision rates in systems of massless fermions (solid line) and classical particles (dashed line).

function of $e^{-\mu/T}$ for both systems consisting of fermions (solid line) and classical particles (dashed line). It is seen that at $\mu = T$ about 30% collisions are blocked, so the blocking effect is quite important.

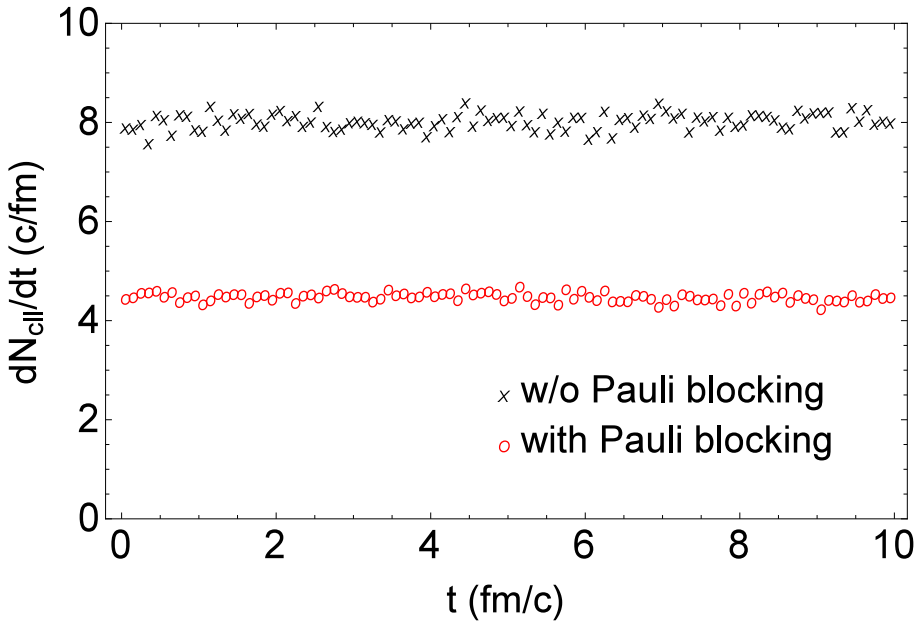

Figure D.4: Numbers of collisions per fm/c for 400 massless fermions (open circles) and classical particles (crosses) in a box of 1000 fm^3 at temperature of 200 MeV.

To implement the Pauli blocking effect in numerical calculations, we first estimate the size of the phase space occupied by partons of different flavors by considering the spatial volume $(-\max(\{|\mathbf{x}_i|\}), \max(\{|\mathbf{x}_i|\}))$ and the momentum volume $(-3\overline{\{|\mathbf{p}_i|\}}, 3\overline{\{|\mathbf{p}_i|\}})$, where the subscription i labels different particles. Although some high momentum particles may be outside above phase space, their density in the momentum space is very small as they are from the tail of the momentum distribution, the Pauli blocking effect on these particles is thus negligible. We then divide the above phase space volume into 10^6 cells and locate each particles in each cell, cal-

culate the phase space distribution by counting the number of particles in each cell, and block the collisions according to the probability f of the final state. We have checked this algorithm for the case of 400 massless particles in a box of 1000 fm^3 and at temperature $T = 200$ MeV. For a scattering cross section of 1 mb, there should be 4.59 collisions per fm/c if the particles are fermions and 8 collisions per fm/c if they are classical particles. Numerical results shown by open circles for fermions and by crosses for classical particles in Fig. D.4 agree perfectly with the expected values, indicating that our algorithm for treating the Pauli effect is almost perfect.